In presenting the dissertation as a partial fulfillment of the requirements for an advanced degree from the Georgia Institute of Technology, I agree that the Library of the Institute shall make it available for inspection and circulation in accordance with its regulations governing materials of this type. I agree that permission to copy from, or to publish from, this dissertation may be granted by the professor under whose direction it was written, or, in his absence, by the Dean of the Graduate Division when such copying or publication is solely for scholarly purposes and does not involve potential financial gain. It is understood that any copying from, or publication of, this dissertation which involves potential financial gain will not be allowed without written permission.

7/25/68

PRECISION SINGLE-CRYSTAL X-RAY DIFFRACTOMETRY

A THESIS

Presented to

The Faculty of the Graduate Division

by

Paul Elias Mackie, Jr.

In Partial Fulfillment

of the Requirements for the Degree

of Doctor of Philosophy in the School of Physics

Georgia Institute of Technology

March, 1972

PRECISION SINGLE-CRYSTAL

X-RAY DIFFRACTOMETRY

Approved:

Chairman

Date approved by Chairman: 10 January 1992

ACKNOWLEDGEMENTS

The author wishes to thank Professor R. A. Young for suggesting the thesis topic, for many helpful hours of discussion and for the constant encouragement to finish this work. This work was made possible because of the financial support received by the author from the National Institute of Dental Research. Further, the author thanks Professor A. J. C. Wilson for the helpful discussions held one summer. The author wishes to thank his wife Janet, for those qualities that one usually thanks wives for in acknowledgements: patience, understanding, and encouragement. But a great debt of gratitude is also owed her for the important contribution of typing the first two drafts of this thesis while taking care of two small children. And finally, the author thanks Mrs. Mary D. Haack for typing the final draft of this thesis.

TABLE OF CONTENTS

Page

ACKNOWLEDGEMENTS ii

LIST OF TABLES viii

LIST OF FIGURES x

SUMMARY xii

Chapter

I. INTRODUCTION 1

General Problem
Purpose of Research
Background

II. INSTRUMENTATION AND EQUIPMENT 7

Tape-Controlled Single-Crystal X-Ray Diffractometer System

Datex Controller
Data Output
Diffractometer
Counting Chain

Computer-Controlled Single-Crystal X-Ray Diffractometer System

PDP-8 Computer and Diffractometer Interface
Diffractometer
Counting Chain
Input-Output

III. LIMITING FACTORS OF PRECISION AND ACCURACY IN MEASURING SINGLE-CRYSTAL BRAGG INTENSITIES 14

Experimental Factors

Lorentz and Polarization Factors
Simultaneous Diffraction
Diffractometer Alignment and Specimen Centering

TABLE OF CONTENTS (Continued)

Chapter Page

Factors Affecting Counting Statistical Errors in Net Integrated Intensities

Effect of Varying the Ratio of Time-On-Peak to Time-On-Background
Effect of Tube Loading on Signal-To-Noise Ratio
Effect of Primary- and Diffracted-Beam Tunnels on the Signal-To-Noise Ratio
Effect of PHD and Scan Widths On the Signal-To-Noise Ratio
Statistical Error in Net Integrated Intensity Due to Statistical Variation of Primary Beam

Choice of Reflections to Minimize Variance In Selected Parameters
Scintillation Detector and Counting Chain
Wavelength Selection
Electronic and Mechanical Sources of Error

Systematic Factors

Absorption
Extinction
Thermal Diffuse Scattering

Structural-Model Limitations

Asphericity of the Atomic Form Factors
Breakdown of Harmonic Approximation
Anomalous Dispersion

IV. EXPERIMENTAL APPROACH. 66

Selection of Specimens
Specimen Preparation
Data Collection Strategy

Two-Pass Method
Controlled Precision
Selection of Scan Modes and Filters
Rotation About the Diffraction Vector
Programmatic Error Responses
Selection of Reflections

V. ANALYTICAL APPROACH. 73

TABLE OF CONTENTS (Continued)

Chapter — Page

Data Reduction

- Absorption Factor
- Lp Factor
- Normalization of the Intensities
- Observed Zeroes
- Flagged Data Which Were Not Used
- Visual Monitoring

Least-Squares Refinements

- Anomalous Dispersion and Extinction Corrections
- Weighting Scheme
- Multiple-Component Structure Models

VI. EVALUATION OF PRECISION TECHNIQUES 83

Introduction
Random Errors
Data Acquisition Rate and "Typical" *vs* "Controlled-Precision" Scanning Techniques
Simultaneous Diffraction

- Effectiveness and Reliability of "Flag-Test"
- Frequency of Occurrence *vs* Setting Asymmetry and Specimen Size
- Effect of Simultaneous Diffraction On the Extinction Constant *c*
- Effect of Simultaneous Diffraction On the Structure Parameters and Their Standard Deviations

Extinction and Anomalous Dispersion Corrections
Physical Reality of Specimen-To-Specimen Differences

VII. MATERIAL RESULTS 113

Introduction
Comparison of Mineral and Synthetic Fluorapatite
Synthetic Chlorapatite

- Pseudohexagonal Character and $P2_1/b$ to $P6_3/m$ Transition

TABLE OF CONTENTS (Continued)

Chapter — Page

Dielectric Behavior

Synthetic Fluor-Chlorapatite

Structure Refinements of the Fluor-Chlorapatites

F/(F+Cl) = 0.43 Fluor-Chlorapatite
F/(F+Cl) = 0.15 Fluor-Chlorapatite

Substitutional Models
Occurrence of Excess Halogen
Sterically Imposed Disorder

Neodymium-Doped Fluorapatites

Least-Squares Analyses
Charge-Balance Mechanism

VIII. CONCLUSIONS 168

Introduction
"Typical" vs "Controlled-Precision" Techniques
Simultaneous Diffraction and Extinction
Atomic Scale Bases for Some Apatite Properties

APPENDICES

A. INITIALIZATION OF THE DATA COLLECTION 172

Introduction
Initialization Program

B. OPTIMIZATION OF THE VARIANCE OF THE INTEGRATED NET INTENSITY OF A BRAGG REFLECTION 175

Single-Scan or Single-Filter Case
Double-Filter or Double-Scan Case

C. DETAILS OF DATA COLLECTION 179

Two-Pass Data Collection Strategy
Mounting Specimens
Centering Crystal and Determining Orientation Matrix

TABLE OF CONTENTS (Concluded)

Page

Wave-Length Selection
Aperture Selection
Computer-Controlled System

(h, k, ℓ) Selection
Scan Mode and Filter Selection
Algorithm for One Reflection
Initial Determination of Signal-To-Noise Ratio and I_n
Multiple Scans
Test for Blunders and Simultaneous Diffraction Effects
Tests for Filter Balance and Unexpected Character in Background

Instrument Performance Monitors of the Computer Controlled System

Collision Recovery
Recovery From Shaft-Encoder Failure
Monitoring of Incident Beam

REFERENCES 195

VITA 200

LIST OF TABLES

Table		Page
1.	Angular Ranges (2θ) Over Which Data Were Collected For Each Specimen.	43
2.	Specimen Characteristics.	69
3.	Linear Absorption Coefficients and Radii of Specimens Used.	75
4.	Final Least-Squares Parameters of Chlorapatite: Data Used Which Had Random Errors Added.	86
5.	Refined Structure Parameters of Fluorapatite (35-7) Data Collected By "Typical" and "Precision" Methods.	93
6.	Percentages of Reflections Flagged For Each Specimen.	98
7.	Number of Reflections Flagged For Various Settings of the Specimen Fluorapatite 35-7	100
8.	Values of the Extinction Constants, c, Obtained For Various Apatite Specimens.	100
9.	Comparison of Least-Squares Parameters For G-6-6-1 (Fluor-Chlorapatite) Using Data With and Without Flagged Reflections.	104
10.	Agreement Factors and Extinction Constants of the Various Apatites Observed	107
11.	Comparison of Refined Parameters of Two Fluor-Chlorapatite Specimens (G-6-6-1 and G-6-6-3).	110
12.	Least-Squares Structure Parameters of Mineral and Synthetic Fluorapatite	116

LIST OF TABLES (Concluded)

Table		Page
13.	Final Refined Parameters of Synthetic Monoclinic Chlorapatite in $P2_1/b$ and $P6_3/m$.	122
14.	Interatomic Distances and Angles for Monoclinic Chlorapatite.	127
15.	Sample Compositions for G-6-6-1 and G-10-1 (weight per cent)	136
16.	Refined Parameter Values of G-6-6-1 and G-10-1 (F/(F + Cl) = 0.15, 0.43).	138
17.	F + Cl and F/(F + Cl) for G-6-6-1 and G-10-1	153
18.	Refined Parameters of Two Nd-Doped and One Pure Fluorapatite; No Nd in the Structure Model.	160
19.	Refined Parameters of Two Nd-Doped and One Pure Fluorapatite.	163
20.	Sample Compositions for FAp:NdF_3 and FAp:Nd_2O_3 (weight per cent).	165
21.	Anomalous Dispersion Corrections for Various Atoms and Wavelengths.	183

LIST OF FIGURES

Figure		Page
1.	Five-Axis Goniostat.	11
2.	Effect of Simultaneous Diffraction on the Intensity of the 03.2 Reflection of Fluorapatite	19
3.	Sharpness of Simultaneous Diffraction Effect.	21
4.	Integrated Intensity of the 08.2 and 13, 0.2 Reflections of Fluorapatite vs Aperture Diameter.	26
5.	Integrated Intensity and Signal-To-Noise Ratio of the 08.6 Reflection of Fluorapatite vs Aperture Diameter	27
6.	Emitted Spectrum vs Operating Voltage, While Tube Loading Held Constant.	31
7.	Effect of Diffracted-Beam Tunnel on the Signal-to-Noise Ratio	33
8.	Integrated Intensity of Standard Reflection for Sample G-6-6-3 vs Time.	36
9.	Integrated Intensity of Standard Reflection for Sample G-10-1 vs Time.	37
10.	Photograph of Beam Diffracted From a Doubly-Bent LiF Monochromator	46
11.	Half-Normal Probability Plot of Parameter Differences Obtained With RE = 0% and RE = 25% Data	88
12.	Variation of Average Standard Deviation of Chlorapatite Oxygens vs Random Error	89

LIST OF FIGURES (Concluded)

Figure		Page
13.	Half-Normal Probability Plot of Parameter Differences Obtained With "Typical" and "Controlled-Precision" Techniques Applied to Specimen FAp 35-7.	92
14.	Percentage of Flagged Reflections vs μR	101
15.	Plan View of Chlorapatite Structure.	123
16.	Stereo-view of 6_3 Axis Environment of Monoclinic Chlorapatite	128
17.	Electron Density Difference Synthesis Along the Screw Axis of Chlorapatite.	134
18.	Difference Synthesis in 6_3 Axis Vicinity For G-10-1 (F/(F + Cl) = 0.43).	142
19.	Difference Synthesis in 6_3 Axis Vicinity For G-6-6-1 (F/(F + Cl) = 0.15)	143
20.	Difference Synthesis in 6_3 Axis Vicinity For G-6-6-1 (F/(F + Cl) = 0.15), F_{II} Included in the Model	147
21.	Difference Synthesis in 6_3 Axis Vicinity For G-6-6-1 (F/(F + Cl) = 0.15), F_I and F_{II} Included in the Model.	148
22.	Proposed Substitution Models: ClAp:F	151
23.	Scattering Factor Curves for Nd and Ca Scaled to Nd.	159

SUMMARY

This study was undertaken to improve the precision of atomic-scale details which can be obtained from single-crystal Bragg intensities. Ultimately, the goal of the work was to show that changes in large-scale observable properties can be explained with models based on the precision of the newly acquired atomic-scale detail.

The initial efforts of this work were devoted to the development and evaluation of techniques for collecting precise single-crystal Bragg intensities. The development of techniques involved equipment design as well as the writing of computer software to collect the data with appropriate strategy. Comparisons of least-squares refined parameters were used to assess the techniques. Comparisons were made for several crystals (a) of presumably identical composition and (b) with compositions differing by known amounts.

"Typical" vs "controlled-precision" techniques, random error, and simultaneous diffraction were the principal effects on precision which were studied.

The "controlled-precision" technique was found to yield significant improvements in precision over the "typical" technique for the same amount of time spent collecting the data. For the case cited, a 25 per cent reduction in time would result if the "controlled-precision" technique was used.

Simultaneous diffraction effects, generally ignored in single-crystal structure-refinements, were found to occur with a disquieting frequency (>14 per cent) for the apatite samples used. These effects were at least 3 per cent of the Bragg intensity. For asymmetrical settings of the crystal, the frequency of occurrence of simultaneous diffraction was still significant (>17 per cent). Least-squares refinements with and without the data affected by simultaneous diffraction gave the same structure parameters (within 3σ; where σ is the pooled standard deviation for the two refinements); however, the agreement factor, wR_2, increased 39 per cent (from 4.35 to 6.04 per cent). Furthermore, the extinction constant, $\underline{c}$, more than doubled when the data affected by simultaneous diffraction were included in the extinction correction procedure. Thus, if any physical interpretation is to be given the extinction constant, $\underline{c}$, one must correct for simultaneous diffraction or remove the affected data before the extinction correction procedure is applied.

The data collection techniques which were developed and evaluated were then used to collect data from seven different apatite specimens. Precision least-squares structure refinements of these data led to significant improvements in the knowledge of the atomic-scale differences in these apatites. Based on these physically significant differences, atomic-scale models were proposed to account for some observed macroscopic properties of various apatites.

Some of the observed physical properties for which atomic-scale models have been presented in this work are:

(1) The occurrence of a monoclinic form of chlorapatite.

(2) The preferential doubling of only one a axis of hexagonal chlorapatite to form the monoclinic structure.

(3) The prevalence of mimetic twinning in chlorapatite.

(4) The initial inhibition and eventual promotion of the monoclinic to hexagonal phase transition with increasing substitution of fluorine into the chlorapatite structure.

(5) The three-fold splitting of the 8600 cm^{-1} fluorescence line in MnO_4-doped chlorapatite.

CHAPTER I

INTRODUCTION

General Problem

The goals of this study were to develop and evaluate techniques for collecting precise intensity data with a single-crystal x-ray diffractometer and reducing these data to structure factor magnitudes, to verify that the precision obtained is physically significant, and to show with several examples how these precision techniques yield new and physically useful information regarding atomic-scale detail in real crystals.

Development of the techniques involved the design of both instrumental and operational aspects of the experiments, including development of computer programs to operate automated diffractometers with appropriate strategy and to assess the validity of the data obtained.

Before the physically significant factor $|F|$ can be deduced with the required precision, several other factors must first be extracted from the observed reflection intensities. The corrections for absorption and polarization are routine, those for extinction effects are somewhat more subtle, and those for simultaneous diffraction effects can not be accomplished by any existing general procedure. Comparisons of least-squares refinement results were thought to be a suitable assessment of the physical significance of observed differences in details (e.g., positions and thermal motion). These comparisons were made for

several crystals (a) of presumably identical chemical composition and (b) with compositions differing by known amounts.

A reasonable test of the physical utility of the new information was felt to be the determination of the structural locations and roles (e.g., effects of neighboring atoms) of various ions substituting in small degree (e.g., < 1 weight per cent) in several apatite crystals. It has been observed that fluorine-containing chlorapatite has a different symmetry (other bulk properties differ also e.g., the optical indicatrix changes from biaxial to uniaxial with the change in symmetry from $P2_1/b$ to $P6_3/m$). Thus, with the introduction of the fluorine ion on the screw axis of chlorapatite, an interaction must occur between the fluorine and the chlorine because the $P2_1/b$ symmetry is a consequence of the ordered displacements of chlorine atoms from $z = 1/2$. Several samples of chlorapatite with various fluorine compositions were studied to see if the precision techniques developed could detect the fluorine-chlorine interactions. Another test of the techniques was the study of two Nd-doped fluorapatite crystals. The determination of the structural location of the Nd presented a challenge because spectroscopic studies had indicated that Nd most probably occurred in apatite at the same site as Ca. Furthermore, the small amount of Nd (growth conditions were adjusted for approximately 0.4 weight per cent or 0.1 Nd per unit cell) could possibly be divided between two independent sites (Ca_I and Ca_{II}).

Purpose of Research

A general assessment of the precision which can be attained in single-crystal diffractometry is an important prerequisite to its use as

a research tool. Limits on precision must be established (under various conditions) if small differences in atomic-scale details are to be meaningful.

It is well recognized that the important mechanisms are in principle predictable from detailed knowledge of location and behavior of all individual atoms. From detailed knowledge of atomic locations and thermal motions in real (non-ideal) crystals, one may expect to determine atomic-scale mechanisms of physical properties, including response to impurities, defects, and environmental changes (e.g., in pressure, temperature, magnetic and electric fields, etc.). In total effect, such an achievement promises to contribute greatly to solid state physics, perhaps forming the basis for major fundamental advances in this broad field. However, at present our available information is much less detailed than is needed, being generally restricted either to (i) average properties of the atoms present in major proportion or (ii) detailed knowledge of only a very few atoms under special circumstances (e.g., information as given by field ion microscopy).

Background

Heretofore, with few exceptions, the assessment of precision has been dealt with in a piecemeal fashion, and often has been of secondary interest compared to the primary goal of the solution of the crystal structure. There are notable exceptions: (i) the American Crystallographic Association Single-Crystal Intensity Project (Abrahams, Alexander, Furnas, Hamilton, Ladell, Okaya, Young and Zalkin, 1967), (ii) the International Union of Crystallography Single-Crystal Intensity Project

(Commission on Crystallographic Apparatus, 1966), (iii) the evaluation of automatic diffractometer systems with NaCl spheres by Abrahams (Abrahams, 1964; Abrahams and Bernstein, 1967) and (iv) the work of Sudarsanan and Young (1969) on determining significant precision in crystal structural details of similar (hydroxyapatite) samples. These studies used various methods for the assessment of precision: 1) different laboratories studied different specimens of the same material, 2) different laboratories studied the same specimen, 3) a single laboratory studied several different specimens of the same material, and 4) a single laboratory studied the same specimen with several different techniques.

The IUCr and ACA single-crystal intensity projects used, respectively, the first and second techniques. These studies did not assess the precision which a single worker could expect to get, but only inter-experimental precision and accuracy. Sudarsanan and Young's work was with mineral samples with significant departures from the ideal hydroxyapatite composition. Several specimens from the same origin, and thus, presumably the same composition, were studied with both x-ray and neutron diffraction. They observed differences in the atomic-scale details between the several specimens. Both the work of Abrahams and that of Sudarsanan and Young ignored the effects of simultaneous diffraction on precision.

In the ACA Single-Crystal Intensity Project, seven laboratories, each one using its normal techniques, measured Bragg intensities from the same small (0.444 mm diameter) sphere of CaF_2. The conclusions of the members of the project (Abrahams et al., 1967) were that routine data-collection procedures could yield $|F|^2$ values within 5 per cent of

each other and that there was no evidence that any experiment was measuring $|F|^2$ values better than 2 per cent. Analyses were not carried out on the data obtained from the secondary spheres each member of the project was given because severe extinction was present and extinction corrections were not made. Thus, an assessment of precision between different specimens could not be made.

In the IUCr Single-Crystal Project, 17 sets of structure factors for D(+)-tartaric acid were measured. Sixteen laboratories participated and each laboratory was provided with approximately 12 well-developed small crystals. The agreement in this project was much poorer (the physical characteristics of the specimens each laboratory were given were different, e.g., different sizes and shapes leading to differing required absorption corrections which, unaccountably, were not always made) than in the ACA project. The agreement in this second project was reported (Commission on Crystallographic Apparatus, 1966) to be approximately 7 per cent for a concordant sub-set of the results. In neither of the Single-Crystal Projects were the data corrected for extinction, simultaneous diffraction or even, in some cases, absorption.

In the present work it was attempted to assess the lack of precision arising from various sources. The same physical specimen was studied with different techniques to assess differences due to technique; several specimens from the same source were studied with the same techniques to assess the physical reality of inter-specimen differences, and several different apatites with slightly different, but known, compositions were studied to demonstrate that the structural locations and roles of ions substituting in small degree could be determined.

In all, precision structure-refinements were made for seven different specimens of various compositions. A substantial effort was first invested in analysis, development and implementation of data-collection and validation techniques. These techniques were intended to improve upon past and current practice with respect to useful precision and, hence, the information available about atomic-scale details. The equipment selected and used, including the modifications made to it, is discussed in Chapter II. The various factors ordinarily limiting available precision in single-crystal diffractometry are analyzed in Chapter III. The experimental and analytical approaches then selected and implemented are discussed in Chapters IV and V, respectively. An evaluation of the precision actually obtained in definition of atomic-scale detail is discussed in Chapter VI. The crystallographic results obtained for the seven different materials are discussed in Chapter VII. Also discussed in that chapter is the new--and in some cases unforeseen--information about structural locations and roles of impurities in varying degrees. The physical significance of this newly available information, which would not have been available with currently conventional techniques, is pointed out. Finally, the principal conclusions resulting from the work are summarized in Chapter VIII.

CHAPTER II

INSTRUMENTATION AND EQUIPMENT

Tape-Controlled Single-Crystal X-Ray Diffractometer System

Datex Controller

The data were collected with two different automated single-crystal x-ray diffractometers. One diffractometer received its instructions from a punched paper tape unit (Datex X-Ray Diffractometer Control and Recording System) and the second diffractometer was controlled by a computer (PDP-8, Digital Equipment Corporation). Fundamental differences in the devices which controlled the two diffractometers necessitated that different control algorithms be used with the two diffractometers. The Datex unit (referred to later as simply the controller) had fixed hardware-wired logic. The programmed operating instructions to drive this fixed logic were obtained as needed from a punched eight-channel paper tape generated, as an independent operation, on a Burroughs B5500 computer. The lack of real-time interactive feed-back from the experiment, when the Datex Controller was used, required that the data set be collected with a two-pass mode of operation. This two-pass strategy is discussed further in Chapter IV.

The controller provided automated control (via instructions from the punched tape) of the following diffractometer functions:

1. The shutter to the x-ray source could be opened or shut and the continued operation of other controller functions was inhibited

until a completion signal for this operation was received by the controller.

2. Four axes of the diffractometer could be sequentially set to the angular values punched on the paper tape. The axes that could be positioned were 2θ, ω, χ, and ϕ. Control did not pass on to the next instruction on the tape unless the proper completion signal for the operation was received by the controller. The axes were physically positioned by a combination shaft encoder and stepping motor. The shaft encoders (analog-to-digital devices) sent back angular position information to the controller to be compared with the command position. If the command position and the actual position agreed, the completion signal was generated.

3. The selection of one of three filter materials could also be made by the controller. In practice, one of the three filter materials is usually an open hole, while the other two materials are selected to permit a balanced-filter configuration (Young, 1963) for the radiation being used.

4. By the proper use of the Datex Controller, one was able to collect data in any of three modes, fixed angle counting, constant speed scanning, and automatic step scanning. With the constant speed scanning mode, five different scan speeds ($\frac{1}{4}$, $\frac{1}{2}$, 1, 2, and 4 degrees per minute) were provided as well as a "slewing" speed for fast axis positioning. Various step sizes were allowed with the step scanning mode. Step sizes of 0.01°, 0.02°, 0.03°, 0.04°, 0.05°, 0.06°, 0.07°, 0.08°, and 0.09° were provided by the controller.

Data Output

The output data were registered on an eight-channel punched paper tape. The information on these paper tapes was later transcribed to punch cards in order to achieve compatibility with the computer center input facilities. The output data tapes were created with an odd-parity punch for each character generated in the eighth channel of the paper tape. The generation of this odd-parity punch was used to check for blunders in the punching mechanism.

The data were also monitored through the use of a strip-chart recorder and a paper tape printer.

Diffractometer

The goniostat was a five-circle design, which was designed and machined at the Georgia Institute of Technology (Young, Goodman, and Kay, 1964) and mounted on a commercially built diffractometer base. The five axes of the goniostat were the 2θ, ω, χ, ϕ, and σ. The σ axis, not usually found on diffractometers, provided a physical means (when $\omega = 0$) of performing rotations of the sample about the diffraction vector $(\vec{s}-\vec{s}_o)$, where $\vec{s}$ is a unit vector along the diffracted beam direction and $\vec{s}_o$ is a unit vector along the incident beam. Figure 1 illustrates the geometry of the five-circle diffractometer.

Counting Chain

The counting chain consisted of a scintillation detector (thallium-activated sodium iodide) and integral preamplifier, a pulse-height discriminator, and a solid-state timer and scaler.

Computer-Controlled Single-Crystal X-Ray Diffractometer System

The second automated diffractometer used was essentially the commercially built Picker FACS-1 system (Picker Corporation, Cleveland), after we had extensively modified its controlling algorithm to meet our data collection requirements.

PDP-8 Computer and Diffractometer Interface

The diffractometer operations were controlled and monitored by a small dedicated computer in a real-time mode of operation. The computer (Digital Equipment Corporation, PDP-8) had a small (4K) fast-access storage, and a large (32K) relatively-slow-access disk storage.

The diffractometer system functions which could be controlled by the computer were the reading, clearing, starting, and stopping of the scaler and timer. Eleven different values of preset count could be selected as well as thirteen different values of preset times. Each of the four shaft encoders could be individually read "on-the-fly" to obtain the current angular position of each shaft. There were four slew motors and two scan motors which could be controlled by the computer. Each motor could be started or stopped, and the shaft positioned in either the forward or reverse direction. Each of the four slew motors had two speeds, "slow" and "fast." A selection could be made of three filter positions and six different beam attenuators. The shutter position (opened or closed) was also controlled by the computer. An addition was made to the diffractometer interface which provided computer on-off control of the drive motor of the strip-chart recorder.

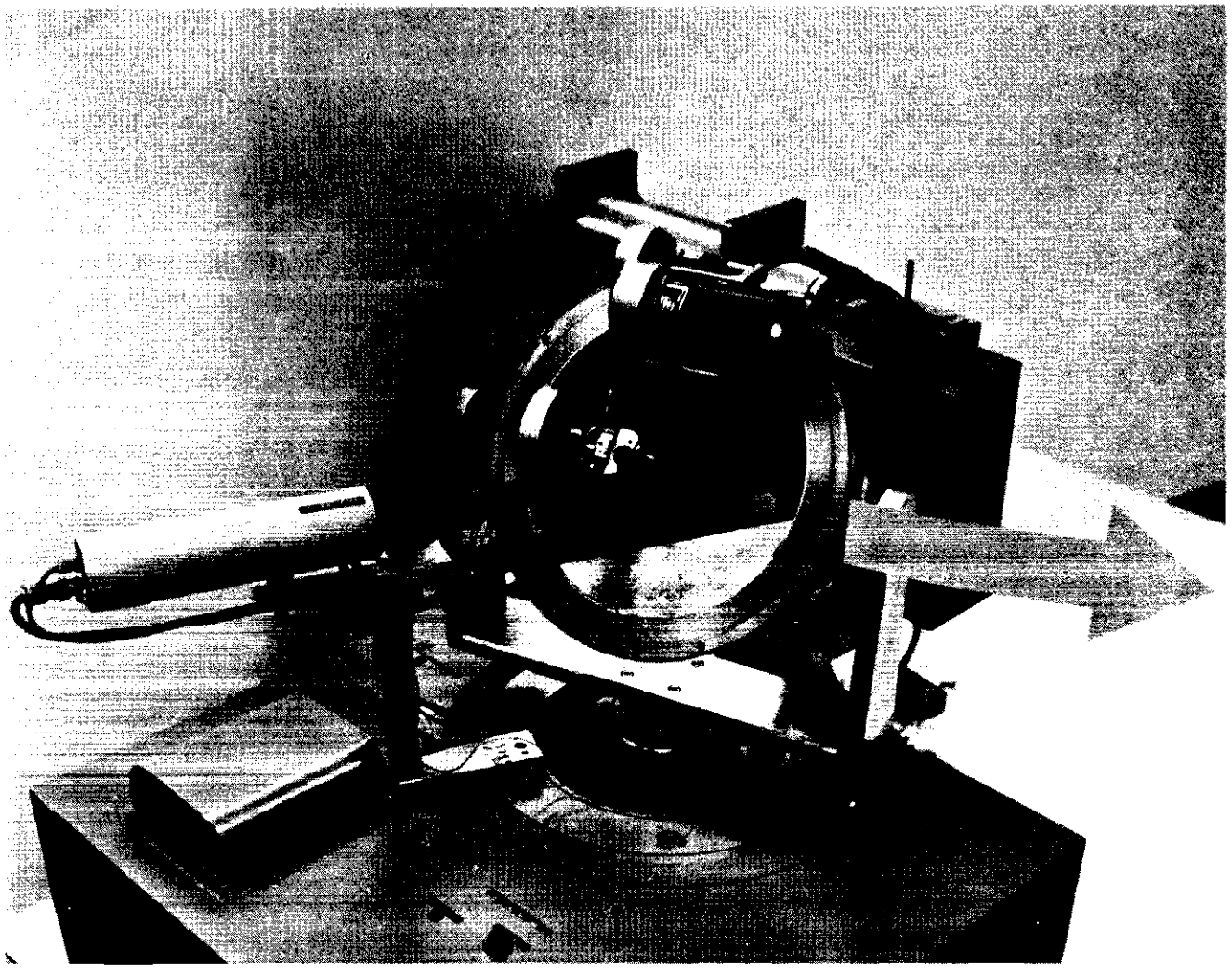

Figure 1. Five-Axis Goniostat.

Thus, on multiple scans over a Bragg peak, the strip-chart recorder could be turned off for all scans but the first one.

Much of the control of the diffractometer system was accomplished through the use of the interrupt concept. With this interrupt feature, at the completion of a diffractometer function the diffractometer interface would interrupt the computer in its performance of some ancillary function and the diffractometer needs would then be serviced by the computer.

Diffractometer

The goniostat was a full-circle design with four adjustable axes: 2θ, ω, χ, and ϕ. This particular goniostat lacked the σ axis, which was available on the goniostat controlled with Datex Controller. Rotations about the diffraction vector were achieved by a combination of rotations about the ω, χ, and ϕ axes.

Counting Chain

The x-ray photon detection circuit consisted of a scintillation detector and integral photomultiplier tube (NaI(Tl)), pulse-height discriminator, and computer-interfaced scalar and timer.

Input-Output

Input information in digital form was received by the computer from the teletype keyboard, the teletype paper-tape reader, and the 300 character-per-second paper-tape reader (See Appendix A for a description of the input program, necessarily developed as a part of this work).

Four forms of data output were available with the system: Intensity vs angle information of an analog nature was displayed on the strip-chart recorder and storage oscilloscope display. The strip-chart

recorder provided a permanent record, while temporary displays of up to thirty minutes duration were provided with the cathode-ray "storage-scope" display. Output information of a digital nature was obtained in two forms: the teletype printer and the teletype eight-channel paper-tape punch. An odd parity bit was generated programmatically for paper-tape output to provide a check for punching errors.

CHAPTER III

LIMITING FACTORS OF PRECISION AND ACCURACY IN MEASURING SINGLE-CRYSTAL BRAGG INTENSITIES

One of the physically significant factors to be obtained in single-crystal x-ray diffractometry is $|F_{hk\ell}|$, the structure amplitude. The quantities observed during the experiment are the integrated Bragg intensities. For an imperfect crystal, the Bragg intensity $I_{hk\ell}$ of the $hk\ell$ reflection is related to the structure amplitude by

$$I_{hk\ell} = cLp|F_{hk\ell}^{OBS}|^2 \tag{1}$$

where the $I_{hk\ell}$ have been corrected for various physical factors (absorption, multiple Bragg scattering, and extinction) which affect the intensities diffracted by a macroscopic crystal. In equation (1), L is the Lorentz factor, p is the polarization factor, and c is an overall scale factor. The superscript OBS indicates that the structure amplitudes are "observed" rather than calculated from a structural model.

If one wants to obtain precision structure amplitudes, two general classes of factors must be considered. One class limits the precision with which one can collect the integrated intensity data (e.g., x-ray source instability), while the other class concerns the corrections to the integrated intensity data for various systematic errors (e.g., extinction and absorption). Precision and accuracy in least-squares refinements can also be affected by a third type of error,

errors which can occur in the calculated structure factor due to limitations of the mathematical model of the crystal structure (e.g., anharmonicity in the thermal motion of the atoms).

The experimental factors which control the precision of the collected integrated intensities will be considered first, then the systematic-error corrections which must be made to the integrated intensities, and finally, the sources of errors in the calculated structure factors.

Experimental Factors

Lorentz and Polarization Factors

The correction for the Lorentz-polarization factor for unpolarized incident radiation and no monochromator in the detected beam is routine. The Lorentz factor corrects the integrated intensities for the different rates with which the reciprocal lattice points (relps) are swept through the Ewald sphere; the factor is inversely proportional to the component of the relp's velocity along the radius of the Ewald sphere. For the geometry of the four-circle diffractometer (normal-beam equatorial) the form of the Lorentz factor is

$$L = (\sin 2\theta)^{-1} \quad . \tag{2}$$

Any deviations of the diffractometer from the ideal diffractometer geometry will result in an improper correction for the Lorentz factor. Thus, the crystal should be centered at the intersection of the four axes of the diffractometer (i.e., at the center of the "sphere of confusion"). The 2θ and ω axes must also be parallel, collinear, and both

perpendicular to the equatorial plane of the diffractometer. Young (1972) has considered in some detail the allowable tolerances in crystal placement and diffractometer alignment. For crystal-placement errors up to 0.04 mm, a precision of 0.01° in each setting axis leads to a cumulative error of ≤ 0.02 in the crystal θ-setting. This was sufficient for a one per cent precision in stationary-crystal stationary-counter intensity measures. The tolerances may be relaxed if the intensities are measured by one of the moving-crystal moving-counter methods.

The polarization factor in the kinematic approximation for once-scattered radiation in normal-beam equatorial geometry, is

$$p = \tfrac{1}{2}(1 + \cos^2 2\theta) \quad . \tag{3}$$

For experimental arrangements which utilize a crystal monochromator the polarization factor is somewhat more complex and subject to error, since the exact form of the polarization correction will depend on the geometry (Azaroff, 1955) and the mosaicity (Miyake, Togawa, and Hosoya, 1964) of the monochromator crystal. For the case in which the plane of incidence of the monochromator and the plane of incidence of the specimen are parallel and coplanar, the polarization correction p, for an ideally imperfect monochromator and specimen crystals, is

$$p = \frac{1 + \cos^2 2\theta_m \cos^2 2\theta}{1 + \cos^2 2\theta_m} \quad , \tag{4}$$

where θ_m is the Bragg angle for the planes being used in the monochromator. However, if the monochromator acts as a perfect crystal

$$p = \frac{1 + /\cos 2\theta_m / \cos^2 2\theta}{1 + /\cos 2\theta_m /} \quad . \tag{5}$$

In general, for a mosaic monochromator, the polarization factor will have a form

$$p = \frac{1 + K(\theta_m)\cos^2 2\theta}{1 + K(\theta_m)} \quad , \tag{6}$$

where the factor $K(\theta_m)$ depends on the degree of perfection of the monochromator crystal. Jennings (1968) and Olekhnovich (1969) have both found values for the polarization correction which exceed those of the perfect crystal case and lie outside the range of values usually assumed possible. Jennings attributes this anomalous polarization correction to a large secondary extinction effect, while Olekhnovich explains it by assuming sufficiently large primary and secondary extinction effects occurring simultaneously. Jennings finds experimentally that the polarization correction may differ by as much as 15 per cent from the value assumed for an imperfect crystal.

For this work a monochromator was not used; however, balanced filters and pulse height discrimination were used.

Simultaneous Diffraction

Simultaneous diffraction is well known to be a problem with neutron diffraction, and the problem has recently received renewed

attention with regard to x-ray diffraction (Cole, Chambers, and Dunn, 1962; Zachariasen, 1965; Young, 1969). The effect of simultaneous diffraction on the intensity of a reflection may range from the insignificant (undetectable within counting statistics) to several hundred per cent. Generally speaking, of those reflections affected by simultaneous diffraction, the relatively weak-intensity reflections are strengthened while the relatively strong-intensity reflections are weakened by the phenomenon. The reflection intensities which occur in the middle range of intensities may be either increased or decreased.

In deriving equation (1), one assumes that the integrated intensity $I_{hk\ell}$ was measured under conditions of single Bragg diffraction. With certain diffraction geometries and crystals of high symmetry, intrinsic simultaneous diffraction occurs. Burbank (1965) discusses the occurrence of intrinsic and systematic simultaneous diffraction with the single-crystal orienter. Intrinsic simultaneous diffraction can be removed if one adjusts the specimen so that no symmetry axis of the crystal is parallel to the ϕ-axis of the diffractometer. Accidental simultaneous diffraction can still occur. By rotating the specimen about the diffraction vector one can avoid, or at least reduce, the effects of multiple scattering (Santoro and Zocchi, 1963; Coppens, 1968). In Figure 2, the effect of simultaneous diffraction on the intensity of the 03.2 reflection of fluorapatite is illustrated as a function of specimen rotation, ψ about the diffraction vector. In this case, if the 03.2 reflection had been measured in the bisecting position (i.e., $\psi = 0^\circ$, $\omega = 0^\circ$), the integrated intensity would have been too large. A rotation of merely $1/2^\circ$ about the diffraction vector would have allowed

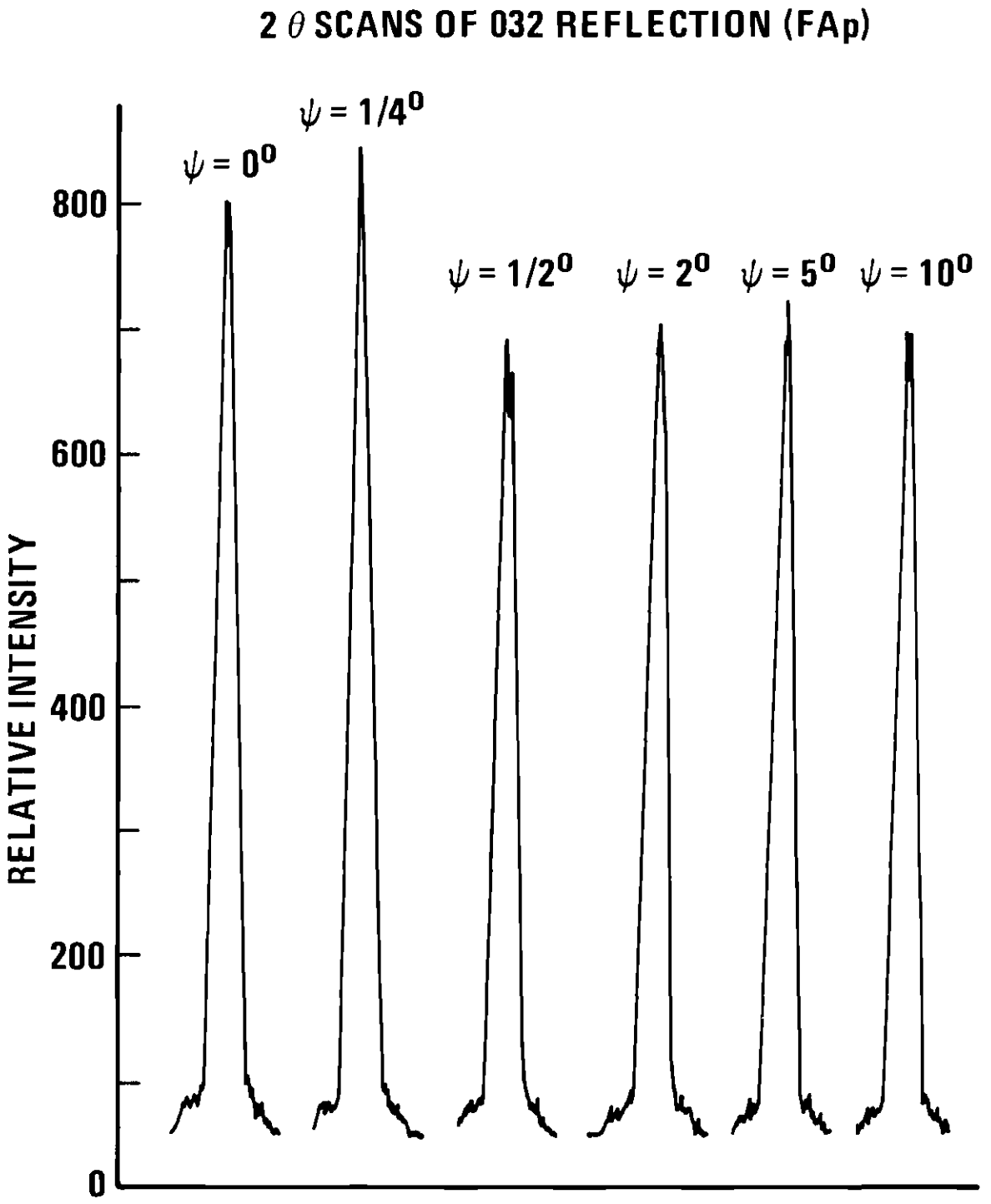

Figure 2. Effect of Simultaneous Diffraction on the Intensity of the 03.2 Reflection of Fluorapatite.

a determination of the integrated intensity free of simultaneous diffraction effects.

The sharpness, in ψ and in λ, of the simultaneous diffraction condition is indicated in a particularly striking way in Figure 3. In this figure we see that for $\psi = 0$, the α_1 component of the Kα doublet is affected very strongly by simultaneous diffraction, while the α_2 component is not perceptibly affected.

Various procedures have been proffered to avoid the inadvertent collection of data under conditions of simultaneous diffraction. Santoro and Zocchi (1964) have described a method for calculating the single-crystal orienter (goniostat) angle settings as a function of the azimuthal angle (rotation about the diffraction vector) and lattice parameters. Furthermore, they describe a method of finding the "optimum" value of the azimuthal angle. For a given set of orienter setting angles, a check is made to see if any other reciprocal lattice point (relp) is simultaneously within some specified small distance ϵ of the Ewald sphere. This procedure is repeated for a series of values for the azimuthal angle ψ. The optimum value of ψ would be in the center of the largest interval of ψ which is free of simultaneous diffraction. This procedure could be very time consuming even with an on-line computer. Furthermore, with large unit cells, the probability of there being a several-degree range of ψ free from simultaneous diffraction is small. Coppens (1968) describes a procedure in which one only has to check for the occurrence of a relp of a strong reflection on either the Ewald sphere of the incident beam or the Ewald sphere of the primary diffracted beam simultaneously with the occurrence of the relp of the

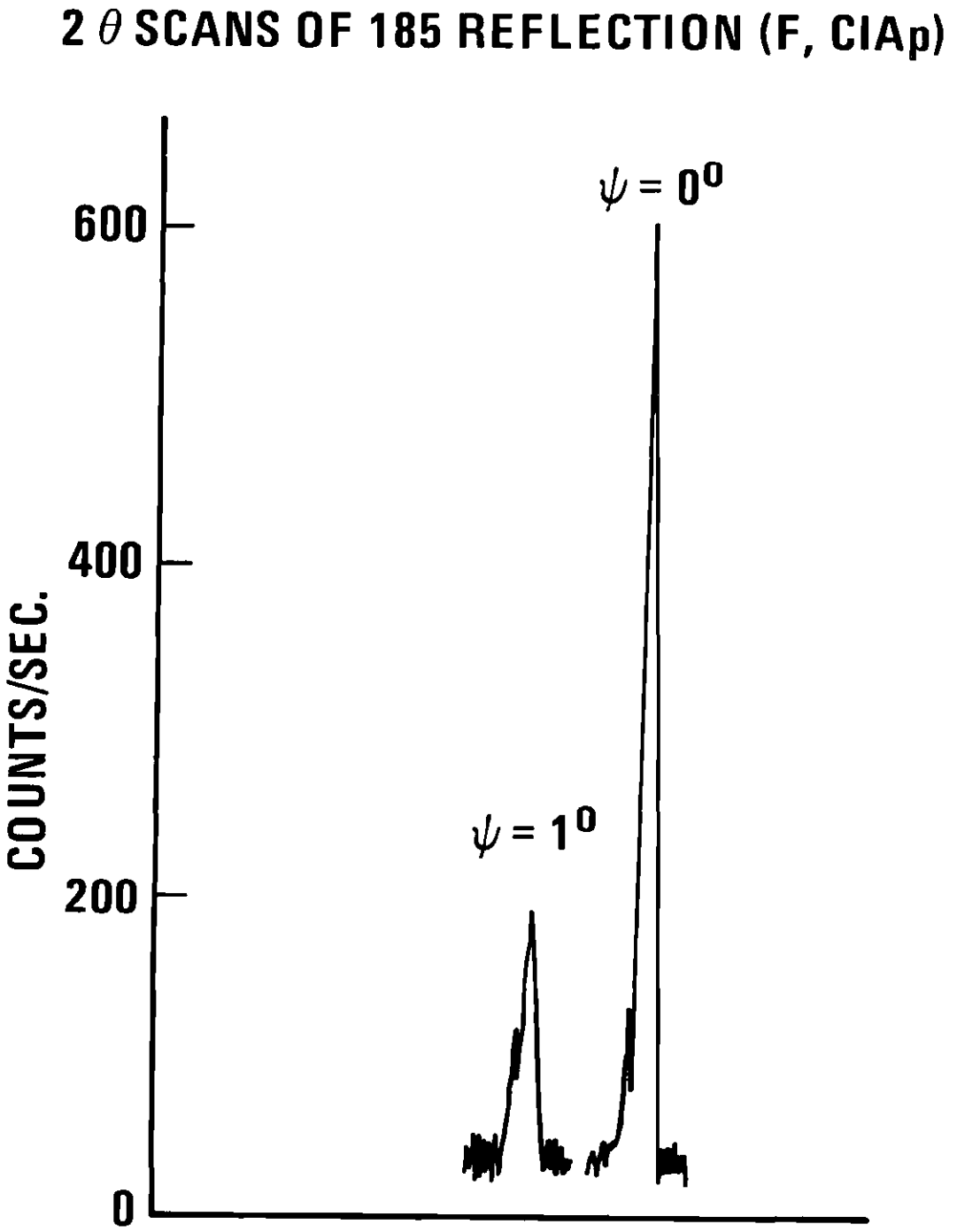

Figure 3. Sharpness of Simultaneous Diffraction Effect.

reflection to be observed on the incident-beam Ewald sphere. This procedure is fast in its operational use and allows one to find relatively simultaneous-diffraction-free intervals of the azimuthal angle.

An operational check for multiple scattering effects can easily be incorporated into the data-collection procedures of a computer-controlled four-circle diffractometer. The integrated intensity is collected at two different settings of the azimuthal angle, one-half of the time being spent at each setting of ψ that would have been spent in collecting the data if only one setting of ψ were used. Thus, it takes no longer to collect the data, except for the additional time to slew to the second set of angle settings. If the integrated intensity for the reflection differs at the two settings of ψ by more than the expected counting statistical error (e.g., at the 95 per cent level of confidence), then the reflection can be flagged on output as being unsuitable for inclusion into the least-squares refinement. Significant amounts of data may be flagged as unsuitable in this manner (up to 30 per cent have been observed to be flagged with apatite crystals). To collect these data under conditions of single diffraction, one could change the orientation of the crystal on the goniometer head (by several degrees) and recollect the previously flagged reflections. Another possible procedure would be to collect the data initially at three settings of ψ (spending one-third the total time at each setting) and to assume that the correct intensity is the average of the two or three values which differ by less than counting statistics. If all three estimates of the integrated intensity differ from each other by an amount greater than predicted by counting statistics, then one must not

use this reflection in the least-squares refinements or must re-collect data for it with a new orientation of the crystal.

Diffractometer Alignment and Specimen Centering

In order for accurate intensity measurements to be made, the diffractometer must be properly "aligned" independently of the x-ray alignment of the single-crystal specimen. The alignment criteria are:

1. 2θ, ω, ϕ must be made parallel and collinear when $\chi = 0^\circ$, 180°.

2. The χ plane must be parallel to 2θ, θ, ω, ϕ; and perpendicular to the equatorial plane of the diffractometer.

3. All four axes and the incident and diffracted x-ray beams must intersect at all times within a small ($\sim 1\,\mu$ radius) sphere, called the "sphere of confusion." Ideally this sphere would degenerate to a point.

4. Define $2\theta = 0^\circ$ as the detector position which intercepts a straight line drawn from the center of the x-ray focal spot through the center of the sphere of confusion and extented toward the detector. This line must be perpendicular to the vertical axis (2θ, ω) of the diffractometer.

5. The axes of the incident and diffracted beam tunnels must be collinear with the lines drawn from the center of the focal spot to the center of the sphere of confusion, and from the center of the sphere of confusion to the center of the detector aperture.

6. The focal spot must lie on the axis used in changing the take-off angle, in order to avoid realignment after changing the take-off angle.

7. The motion of the 2θ and θ axes must satisfy a 2:1 relationship.

8. Backlash in the angular settings should be small, or the position-sensing take-off (e.g., to the shaft encoders) should be independent of the positioning shaft and free ($< 0.01^{\circ}$) from backlash. About 0.005° of backlash is inherent in the encoders themselves due to the leading and trailing edges of the brushes and encoder disks.

Most of the critical points of the orienter alignment are, usually, adequately taken care of during final assembly when the diffractometer is built. Occasionally some aspects of the alignment must be checked because of instrument modifications, damage, wear or slippage. Even with a properly aligned diffractometer, a miscentered specimen will indicate an apparent need for 2θ and χ zero corrections. Furthermore, the miscentered crystal's position will move in the x-ray beam as any of the axes are rotated. If the beam is inhomogeneous, the effective integration of the intensities of the various peaks will vary from reflection to reflection, and, in an extreme case, the crystal may be translated entirely out of the incident beam. Polarization and Lorentz corrections are also affected by miscentering. A 0.04 mm error in centering the sample will result in an error in the Lp correction as large as 1/2 per cent in the range $5^{\circ} < 2\theta < 175^{\circ}$.

That various small departures from the ideal alignment will not seriously affect the integrated intensity is readily recognized if one considers the concept of an "acceptance region" (Young, 1959). This has been dealt with in some detail recently by Young (1972).

A particularly easy operational test exists for determining the proper size of detector aperture to use with one's current experimental conditions. The test consists of repeated measurements of the integrated intensity with various sizes of apertures being used. If the integrated intensity is plotted versus the aperture diameter, a result similar to Figure 4 and 5 is obtained. With an aperture too small, some of the diffracted radiation is not detected by the scintillation detector; but, as the aperture size is increased, the integrated intensity increases and then gradually levels off. If the aperture is increased still further, the integrated intensity may eventually decrease because of the background curvature due to tails of other peaks or angle-dependent diffuse scattering (e.g., air scattering of main beam). The "optimum" aperture size is one which just permits collection of all the Bragg-diffracted x-rays of the characteristic wavelength. An aperture size any larger only tends to decrease the signal-to-noise ratio, S, as is shown in Figure 5. The dependence of the minimum aperture on sample mosaicity and wave-length spread in the incident beam (i) differs for ω and 2θ scans and (ii) must be determined for each sample. The minimum aperture size generally increases with Bragg angle (for ω scans) and thus should be determined at a high Bragg angle, if automatic control over the aperture size is not available and manual intervention is inconvenient.

The operational test for determining proper aperture sizes was performed at high ($2\theta > 70^\circ$) Bragg angles and the "optimum" aperture size indicated was used at all times in the present work.

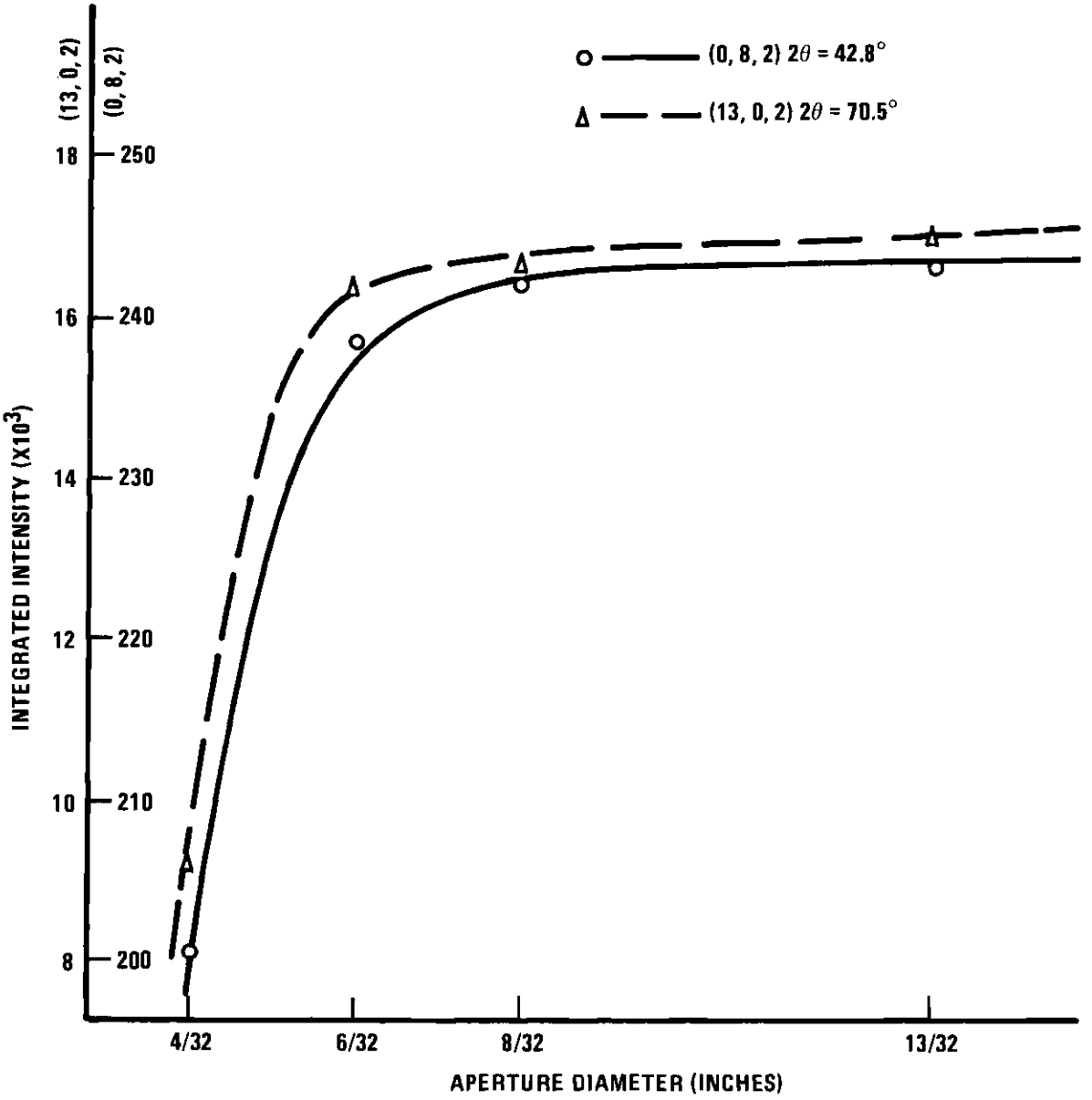

Figure 4. Integrated Intensity of the 08.2 and 13, 0.2 Reflections of Fluorapatite vs Aperture Diameter.

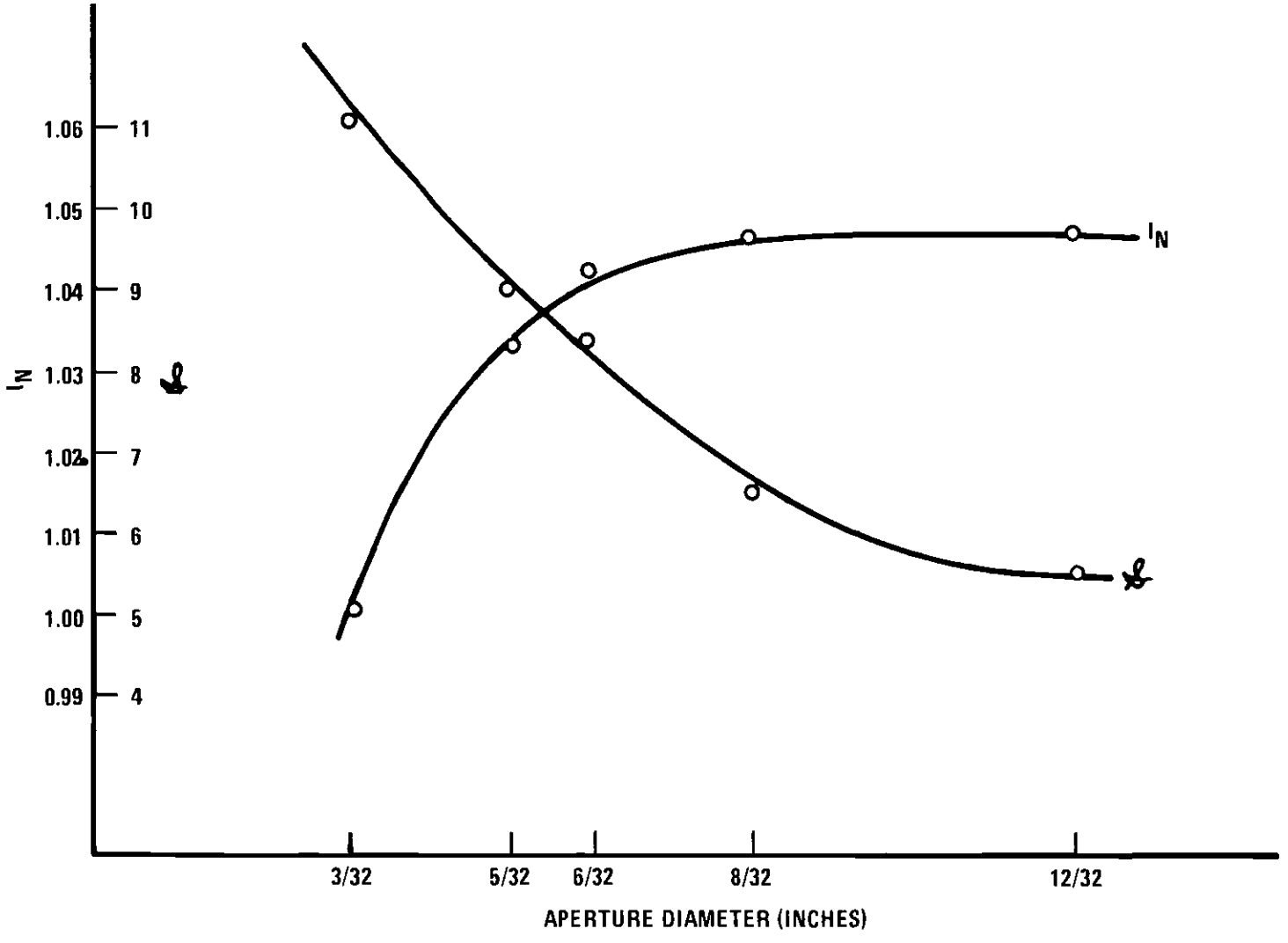

Figure 5. Integrated Intensity and Signal-to-Noise Ratio of the 08.6 Reflection of Fluorapatite vs Aperture Diameter.

Factors Affecting Counting Statistical Errors In Net Integrated Intensities

The contribution of counting statistical errors to the net integrated intensity can be decreased if one has properly designed equipment and collects the data with techniques designed to minimize the counting statistical error.

Effect of Varying The Ratio of Time-On-Peak to Time-On-Background. A derivation of the optimum ratio t_{opt}, of time spent on the peak to the total time spent on the background is in Appendix B and follows that of Young (1965). The expression for the optimum ratio of time t_{opt} in the single-filter case is:

$$t_{opt} = (1 + S)^{\frac{1}{2}} \quad , \tag{7}$$

where S is the signal-to-noise ratio. For a balanced-filter scan, the optimum ratio for t is:

$$t_{opt} = (1 + S_A/2 + S_B/2)^{\frac{1}{2}} \quad , \tag{8}$$

where S_A and S_B are the signal-to-noise ratios obtained with the alpha and beta filters, respectively. Since $S_A \approx 0$, then

$$t_{opt} \approx (1 + S_B/2)^{\frac{1}{2}} \quad . \tag{9}$$

The optimum fractional standard deviation, $\sigma(I_N)/I_N$, for the single scan case, can be expressed as:

$$\left[\frac{\sigma(I_N)}{I_N}\right]_{opt} = \frac{\left(1+\frac{1+(1+S)^{\frac{1}{2}}}{S}\right)^{\frac{1}{2}}}{I_N^{\frac{1}{2}}} \quad , \tag{10}$$

and for the balanced-filter case:

$$\left[\frac{\sigma(I_N)}{I_N}\right]_{opt} \approx \frac{\left(1+\frac{1+(1+S_B/2)^{\frac{1}{2}}}{S_B/2}\right)^{\frac{1}{2}}}{I_N^{\frac{1}{2}}} \quad . \tag{11}$$

Equations (9) and (11) illustrate that the effective signal-to-noise ratio, for the two scans of a balanced filter method of data collection, is half that of a single scan or single filter method. Thus, on a basis of signal-to-noise ratio only, one would prefer to collect the integrated intensities with a single scan or single-filter method whenever possible. Furthermore, an analysis of equation (10), similar to that carried out by Young (1965), reveals that an increase in S, when accompanied by a reduction in I_N, is not always beneficial; in fact, the fractional standard deviation can increase rather than decrease.

The optimum ratio of time t_{opt} was used to collect the data for each reflection with the computer-controlled diffractometer.

Effect of Tube Loading on Signal-To-Noise Ratio. As can be seen from equation (10), anything which will increase the signal-to-noise ratio without decreasing the net integrated intensity will improve (i.e., decrease) the fractional standard deviation. A higher operating voltage on the x-ray tube results not only in a higher I_N, but also in a higher S. The intensity of the characteristic radiation

is proportional to the tube current and proportional to the difference between the tube voltage and excitation potential raised to approximately the 1.5 power (the total radiation from the continuous spectrum increases in proportion to the square of the tube voltage, but the pulse height discriminator passes only a small portion of this). Thus, for a given tube loading, it is more favorable to increase the tube potential and reduce the tube current, to be consistent with the maximum rating of the tube, than to operate at the maximum current rating with reduced voltage. The effect, on the emitted spectrum, of changing the high voltage on the tube, while keeping the tube loading constant, is shown in Figure 6. If needed, higher operating loadings can be achieved with a rotating anode arrangement. Furthermore, a constant potential generator will provide a higher signal-to-noise ratio, without a reduction in the net integrated intensity, than the full-wave or half-wave rectified voltage sources.

Constant potential generators were used in this work and the x-ray tubes were operated at the highest permissible voltage (50 KeV) and the maximum current allowed for that voltage (16 ma). From Figure 6 we can see that the signal-to-noise ratio of the Kα wavelength increased significantly as the voltage was increased: $S \approx 4.7$ at 24 KeV, $S \approx 10.3$ at 30 KeV, and $S \approx 23.0$ at 50 KeV (corrected for count losses at 50 KeV).

Effect of Primary- and Diffracted-Beam Tunnels on The Signal-To-Noise Ratio. The use of primary-beam and diffracted-beam tunnels will reduce the amount of parasitic scattering which is detected. If properly designed, these beam tunnels permit the detector to view only the

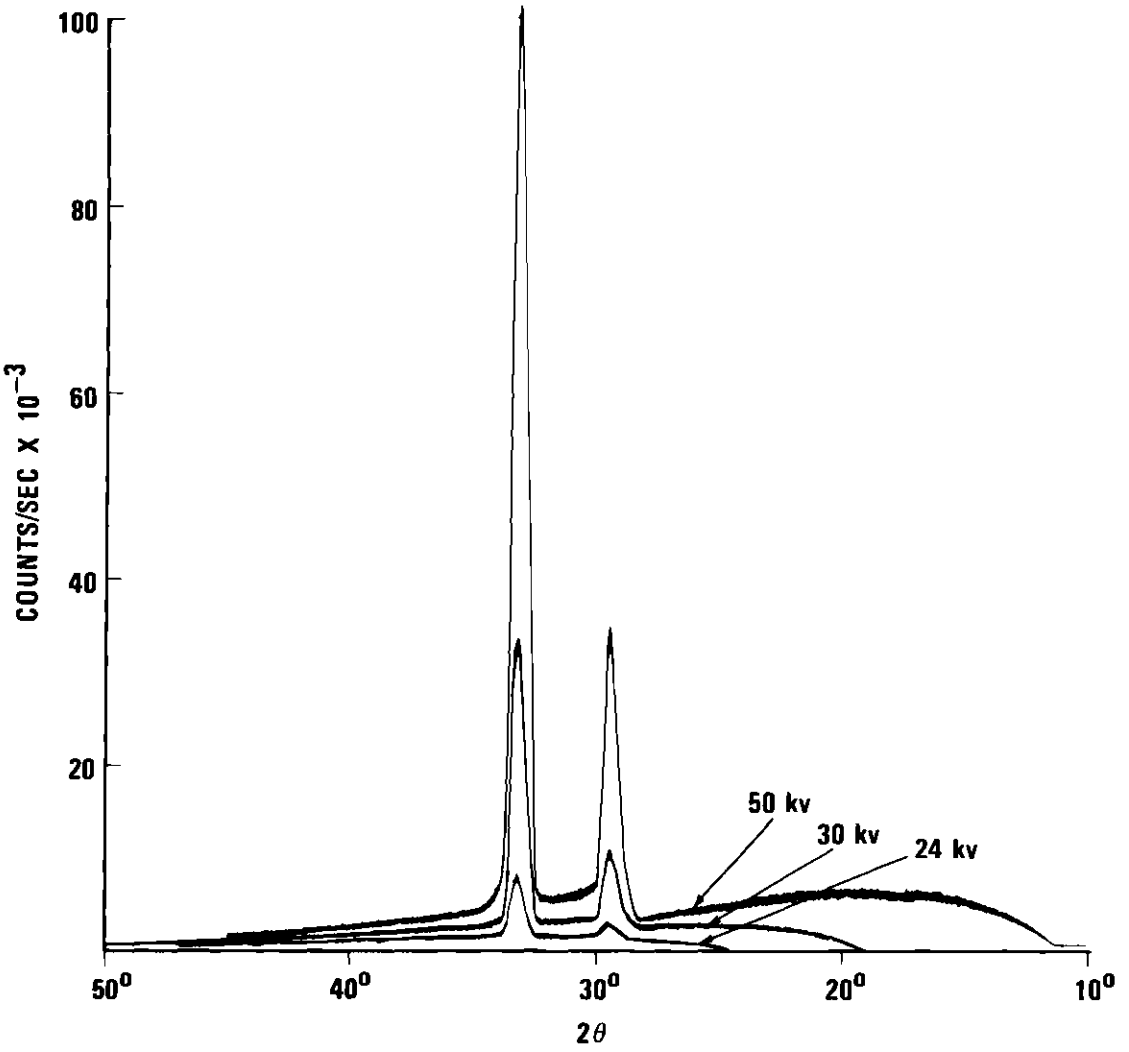

Figure 6. Emitted Spectrum vs Operating Voltage, While Tube Loading Held Constant.

specimen and the x-ray beam path in the immediate neighborhood of the specimen. The function of the detected-beam tunnel is not to function as a collimator, but to limit the view of the detector to a small volume containing the specimen. An immediate consequence of this will be an improvement in the signal-to-noise ratio. The effect of a diffracted beam tunnel on the signal-to-noise ratio is shown in Figure 7. Such beam tunnels were used in this work.

Effect of PHD and Scan Widths on the Signal-To-Noise Ratio. The signal-to-noise ratio may also be improved, without decreasing I_N, if one uses a pulse height discriminator (PHD) to reduce the contribution of the continuous spectrum and harmonics to the integrated intensity. The "window" in the PHD must be wide enough so that small instabilities in the electronic circuits will not result in a change in the integrated intensities.

The use of an excessive scan width, when one scans over a peak, reduces the signal-to-noise ratio. The choice of a narrower scan range over the peak must be made with the concomitant increase in the truncation error kept in mind. The truncation error is due to not including in the scan over the peak the Bragg diffracted intensity which occurs in tails of the Bragg peak. If an adequate truncation-correction procedure is not available, one should reduce the truncation error with a wider scan range, which will require longer counting times to obtain the same fractional standard deviation.

A pulse height discriminator was used during the collection of all of the data for this work and scan widths were kept small ($\sim$ 1.5 to 2 degrees) to increase the signal-to-noise ratios of the Bragg peaks.

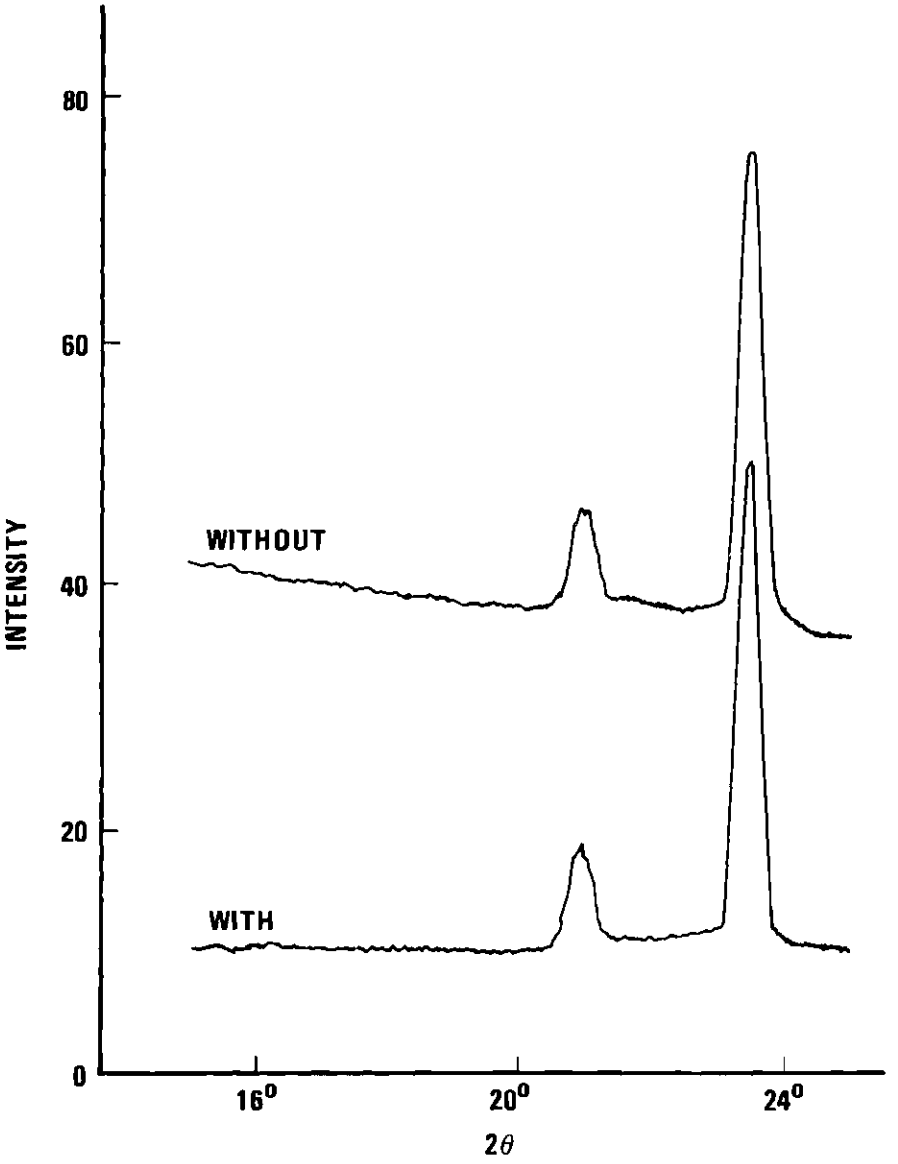

Figure 7. Effect of Diffracted-Beam Tunnel on the Signal-to-Noise Ratio

At the same time, these scan widths were wide enough (as judged by looking at strip-chart recordings) to eliminate truncation error as much as experimentally possible without resort to analytic truncation-error corrections.

Statistical Error In Net Integrated Intensity Due to Statistical Variation of Primary Beam. If the primary beam is being monitored, the statistical variation of the monitor count must be included in the standard deviations of the relative intensities. The variance of the normalized $I_{hk\ell}$ will be (the background can be neglected if the monitor intensity is much greater than the Bragg intensity)

$$\sigma^2(I_{norm}) = \left| \frac{\partial I_{norm}}{\partial I} \right|^2 \sigma^2(I) + \left| \frac{\partial I_{norm}}{\partial M} \right|^2 \sigma^2(M) \quad , \tag{13}$$

where

$$I_{norm} = \frac{I}{M} \quad , \tag{14}$$

and I is the number of counts detected for the $hk\ell$ reflections, and M is the number of monitor counts accumulated. Equation (13) reduces to

$$\sigma^2(I_{norm}) = I_{norm} \left(1 + \frac{I_{norm}}{M}\right) \quad . \tag{15}$$

Thus, the statistical variations of the monitor count may be ignored if $M \gg I_{norm}$. For $M = 1000\ I_{norm}$, a 0.1 per cent error is made in the variance if one neglects the statistical variation of the monitor count.

Monitoring the primary beam, however, does not give any indication of possible specimen deterioration, or change in mounting orientation. In this work, these effects were monitored with the periodic collection of the Bragg-intensity data of a standard reflection. The data can be placed on the same scale with the division of each Bragg intensity by the intensity of a periodically measured ($\sim$ every 1 to 3 hours) standard reflection. There are a number of ways in which the normalization can be accomplished. The simpliest way is merely to divide all of the intensities by the average of the two standard-reflection measures bracketing each block of measurements of reflection intensities. The statistical variation of the standard reflection will affect the variances of the normalized intensities as in equation (15). If one does not normalize the data, then to the variance of each reflection a term must be added which makes due allowance for statistical and systematic variation of the primary beam and counting-chain response.

Rather than normalizing the data in blocks to the average of the adjacent standards, one might choose to fit by least-squares a polynomial to the series of standard intensities and to normalize the data to this smooth curve. A contribution to the variance of the intensity of a reflection would then arise from the variance obtained from the least-squares procedure for the curve. Figures 8 and 9 show the intensities of the standards plotted as a function of time and the quadratic curves fitted by least-squares to the data. The data all fall within a range of $\pm$ 1 per cent from the curves obtained by least-squares fitting.

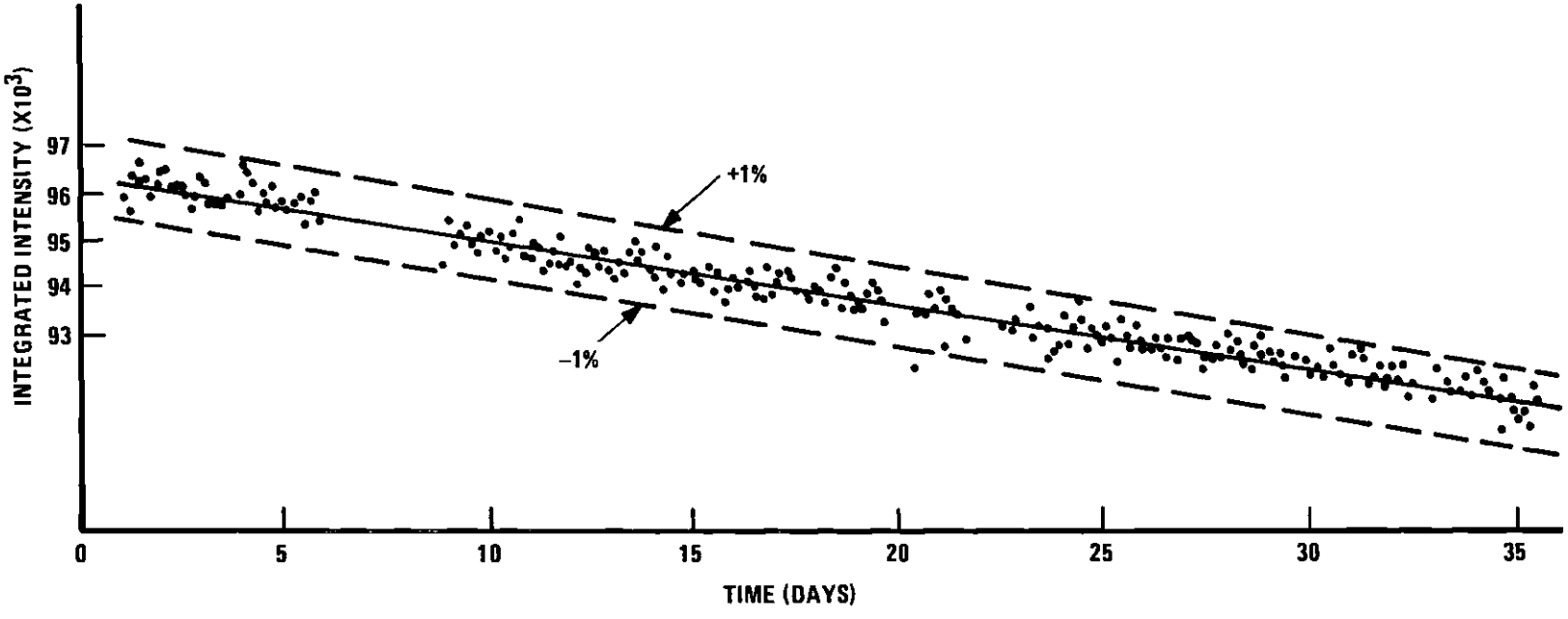

Figure 8. Integrated Intensity of Standard Reflection for Sample G-6-6-3 vs Time.

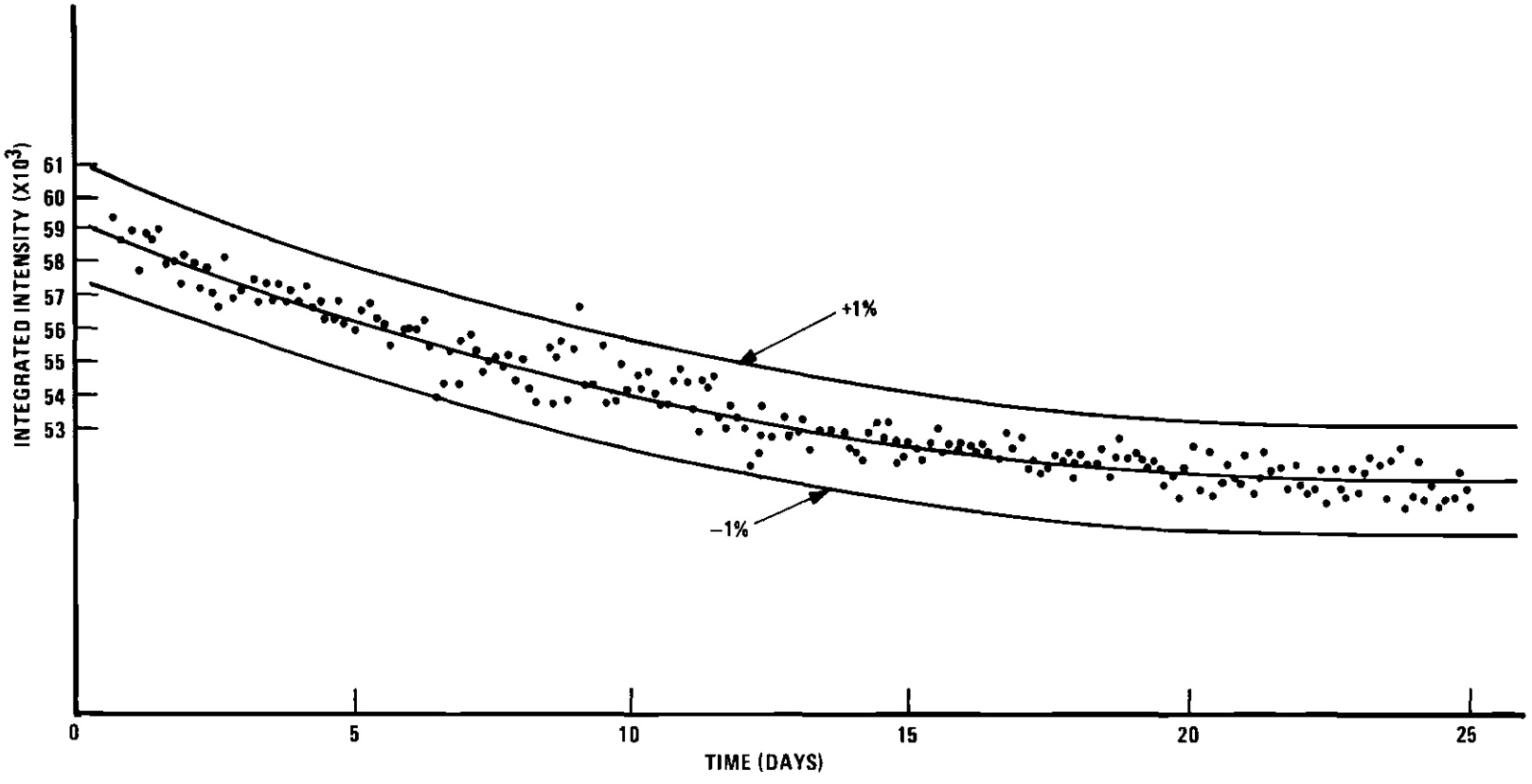

Figure 9. Integrated Intensity of Standard Reflection for Sample G-10-1 vs Time.

Choice of Reflections to Minimize Variance in Selected Parameters

From a practical point of view, one must set a limit to the duration of the data collection. Within the constraint of a fixed total time T for the experiment, one has a choice of collecting the complete set of data with a low statistical precision or a subset of the data with a concomitant increase in the statistical precision. Which technique is better, from the standpoint of variances of the parameters $\sigma^2(p_i)$, can be seen from the expression for the variance obtained from the least-squares procedure. If the correlations between the variable parameters are small the variance of the i^{th} parameter is:

$$\sigma^2(p_i) \approx \frac{1}{\sum_h W_h \left(\frac{\partial \Delta_h}{\partial p_i}\right)^2} \tag{16}$$

where

$$\Delta_h = -2|F_h| \frac{\partial |F_h|}{\partial p_i} \tag{17}$$

for least-squares minimization of the function R_2 (see equation 49). Let M reflections be collected at a time t_m per reflection for the first data set and N reflections at t_n per reflection for the second data set. Then

$$Mt_m = T \tag{18}$$

and

$$Nt_n = T \quad . \tag{19}$$

Substituting (17) into (16) we obtain:

$$\sigma^2(p_i) \approx \frac{1}{\sum_h W_h 4|F_h|^2 \left(\frac{\partial|F_h|}{\partial p_i}\right)^2} \quad , \tag{20}$$

where the upper limit on the summation is M for the first data set and N for the second. If the two sets of data are chosen in such a manner that they are both representative samples of the population from which they were drawn, then it can be assumed that:

$$\langle|F_h|^2\rangle_m = \langle|F_h|^2\rangle_n \tag{21}$$

and

$$\left\langle\left(\frac{\partial|F_h|}{\partial p_i}\right)^2\right\rangle_m = \left\langle\left(\frac{\partial|F_h|}{\partial p_i}\right)^2\right\rangle_n \quad . \tag{22}$$

Replacing the summation in equation (20) by averages we find:

$$\sigma_m^2(p_i) \approx 1/(C\,M\,\langle W_h\rangle_m) \tag{23}$$

and

$$\sigma_n^2(p_i) \approx 1/(C N \langle W_h \rangle_n) \quad , \tag{24}$$

where

$$C = 4\langle |F_h|^2 \rangle_j \left\langle \left(\frac{\partial |F_h|}{\partial p_i} \right)^2 \right\rangle_j \tag{25}$$

and j is either M or N. If the weights W_h are assigned as the reciprocal of the statistical variances, then

$$\langle W_h \rangle_m = \frac{N}{M} \langle W_h \rangle_n \quad . \tag{26}$$

Substituting equation (26) into equations (23) and (24) we find,

$$\sigma_m^2(p_i) = \frac{1}{C M \frac{N}{M} \langle W_h \rangle_n} = \sigma_n^2(p_i) \tag{27}$$

Thus, the least-squares variances of the parameters p_i will be the same for the two sets of data, if equations (21) and (22) are valid. Equations (21) and (22) require that the same number of counts above background be collected in both sets of data and that the reflections in the two sets have the same sensitivities to shifts in the parameters. It should be noted, however, that a smaller subset of data, collected in the same total time T, can yield improved $\sigma^2(p_i)$ if the data are collected in a selective manner such that relations (21) and (22) no longer remain true. In particular, if knowledge of one specific parameter

(e.g., p_k) were desired its variance could be optimized by choosing those reflections for observation for which γ_i is large for i = k and small for i ≠ k, where

$$\gamma_i = \left(\frac{\partial |F_h|}{\partial p_i} \quad \frac{\partial |F_h|}{\partial p_k} \right) \quad . \tag{28}$$

If this were done for each parameter, the resulting normal equations would be nearly diagonal (correlations between parameters having been minimized) and the convergence of the least-squares process would be accelerated. In practice the strong correlations between some parameters can not be reduced to the point where they can be ignored (e.g., between the overall scale factor and the overall temperature factor; between the individual site occupancy factors and the individual temperature factors). To separate out the effects of the scale factors and thermal parameters one must insure that the data have been collected over an extensive range of $\sin\theta/\lambda$. This method of selecting reflections was not used because the contribution of the calcium atoms of the apatite structure dominates the total scattering. In effect, γ_i for every reflection was much larger for a calcium parameter than any other parameter of the structure. As a consequence of this, as one can see in Chapter VII, the parameters of calcium were determined better (i.e., smaller standard deviations) than any other parameters.

The number of apatite reciprocal lattice points that could be reached with MoKα radiation and a maximum 2θ of 130° was approximately 37,000, of which more than 3,000 were crystallographically non-equivalent. For synthetic chlorapatite with a stoichiometric amount of

chlorine, the space group is not $P6_3/m$ but is $P2_1/b$ and, thus, the number of unique accessible reflections is more than 9,000. If each reflection were measured very rapidly the complete set of data could be collected in a reasonable time. However, to detect simultaneous diffraction at a high significance level would require too much time if a complete data set were collected. The detection of simultaneous diffraction effects by the comparison of two intensity measures can only be efficacious if the differences due to statistical fluctuations are smaller than the expected simultaneous diffraction effects. However, if one is willing to flag reflections (because of simultaneous diffraction effects) at a lower level of significance, then the complete set of data can be collected with the controlled-precision techniques without an increase in the collection time over that of the typical technique. A small (approximately 1000-1500 reflections) subset of data was chosen for collection with a higher precision than could have been obtained with the full set of data in the same length of time. The data in this subset were not chosen by zones, for these "special" reflections would have resulted in larger standard deviations for some refined parameters while yielding smaller standard deviations for others. The reflections selected occurred in bands concentric about the origin of reciprocal space. These bands were selected to span as large an interval of $\sin\theta/\lambda$ as possible, in order to facilitate the determination of the highly-correlated overall scale factor and thermal parameters. Nevertheless, for five specimens the data for all reflections within one broad angular range of 2θ were collected, the angular range for these data being nearly the same as the multi-band data (see Table 1).

Table 1. Angular Ranges (2θ) Over Which Data Were Collected For Each Specimen

SPECIMEN	ANGULAR RANGES (2θ)	NUMBER OF REFLECTIONS MEASURED
G-6-6-1	30° to 90°	1384
G-6-6-3	30° to 90° 100° to 120°	1380
NdF_3-FAp-2	30° to 90°	900
Nd_2O_3-FAp-1	30° to 90°	1010
G-10-1	30° to 90°	1129
Syn FAp-35-7	40° to 60° 75° to 85° 100° to 120°	1086
Syn ClAp-L1-24	25° to 100°	2232

Scintillation Detector and Counting Chain

Errors of several per cent in the observed Bragg intensities can arise from non-linear response and lack of uniform response over the surface of the scintillation crystal used in the detector. Minor errors in the settings of the specimen will result in various portions of the detector being used to detect the diffracted x-rays from different Bragg peaks. Uniform response may be checked if the face of the detector is moved across a small diameter x-ray beam ($\sim$0.2 mm diameter) and the response of the ratemeter observed. The intensity of the beam should be within the range of linear response of the counting chain and detector. The time constant of the ratemeter should be on the order of the time it takes to move the detector a distance equivalent to the x-ray beam diameter so that one may detect rapid spatial changes in the response. Over a period of time (6 months to 1 year), scintillation detectors may develop a relatively "dead" spot at that point where most of the reflections have been detected, resulting in progressive fatigue at that point. The response of the scintillation crystal was checked in this manner several times while this work was in progress. On one occasion crystal response was found to be non-uniform (one spot in particular on the crystal gave a much lower count rate than other points around this spot) and the scintillation crystal and photomultiplier tube were replaced.

Wavelength Selection

The volume of reciprocal space which can be sampled can be increased if one selects x-ray tube targets with short wavelengths such as MoKα. However, many of the reflections made accessible by a short-

wavelength target may have an effectively zero intensity because of the $\sin\theta/\lambda$ dependence of the temperature factor.

The wave length should be chosen not to produce significant fluorescence of the specimen. The fluorescence scattering is incoherent and contributes a background which, of course, has the undesirable effect of reducing the signal-to-noise ratio.

The corrections for anomalous dispersion will be greater if the wave length used is near an absorption edge of any of the constituent atoms of the specimen. Since it is better to eliminate the need for a correction than to make a large correction, one should choose λ to avoid the absorption edges of the constituent atoms.

There exist several prevailing methods of restricting the wavelength pass band of the spectrum emitted from the x-ray tube. Crystal monochromatization is used, but has the attendant problems of: (1) lack of intensity, (2) uncertainty in the polarization correction, and (3) non-uniform reflectivity over the surface of monochromator (see Figure 10). Balanced-filter (Ross filters) methods suffer in that the signal-to-noise ratio is reduced by a factor of two from the single filter methods. The background correction is difficult to apply at low Bragg angles with a single filter scheme, because the absorption edge of the filter material occurs near the Bragg peak, in the angular range where the background is sampled. This does not permit a good linear extrapolation (of the background) to be made. In practice, one either uses a monochromator or a combination of no-filter, single-filter, and balanced-filter scans. In this work each of the three types of scans were used. The most appropriate of the three types of scan was chosen on the basis

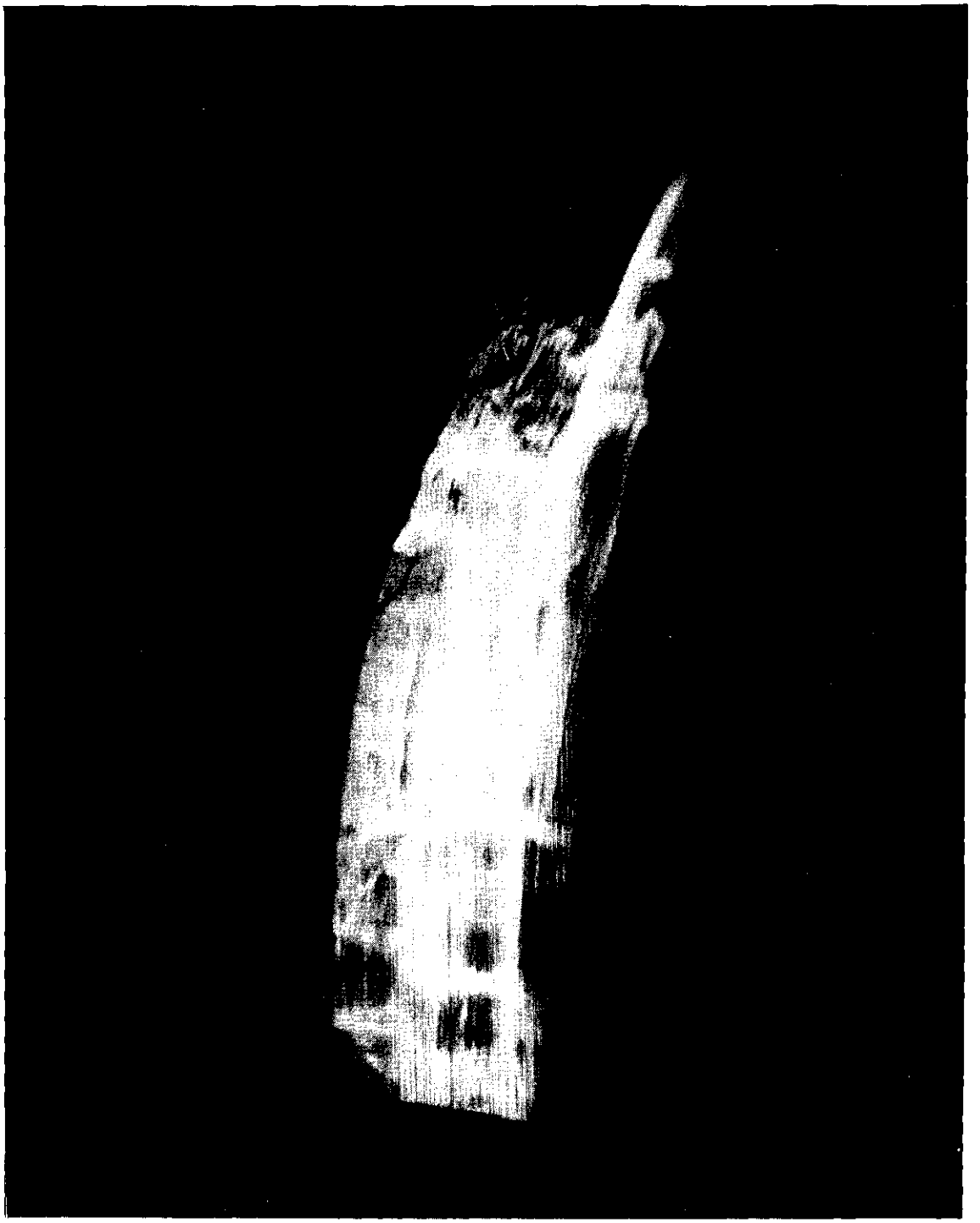

Figure 10. Photograph of Beam Diffracted From a Doubly-Bent LiF Monochromater.

of various experimental conditions (discussed in Appendix C under the topic "scan mode and filter selection").

Electronic and Mechanical Sources of Error

Possible electronic problems with the PDP-8 computer can be generally foreseen and corrected before they become a problem if a good preventive maintenance program is used. The computer has "margin" switches, which place marginal voltages (either too high or too low) on various sections of the computer logic circuitry, to aid one in the diagnostic check-out of the computer reliability. A computer malfunction usually halts the computer abruptly without compromising more than a small portion of the intensity data. Electronic errors and mechanical problems elsewhere in the system are somewhat more subtle. With the use of an on-line computer many of the possible types of errors can be checked for. Some types of errors which can occur are: (1) tape-punching mechanism malfunctioning, (2) scaler or timer dropping digits or entire numbers, (3) counting chain unstable, (4) shaft encoders reading improperly, and (5) generator unstable. All of these can be detected, with varying degrees of success, with an on-line computer. Error (1) can be detected with the generation of a parity bit and checking the output tape for the proper parity. Errors of type (2) can be detected if the data for each reflection are collected twice, spending one-half the normal time for each collection, and the two results compared for a statistically significant difference. Type (3) and (5) errors are manifested by changes in the periodically collected intensity of a standard reflection. Type (4) errors can be detected because the shaft encoders have independent sets of brushes, which permit a self-

checking code. This redundant code is capable of revealing incorrect angle readings of the diffractometer shaft settings.

The frequency and seriousness of errors arising from malfunctioning hardware depends, in large degree, on the quality of the maintenance given the equipment. The errors in the Bragg intensities can range from the insignificant (< 0.1 per cent) to several hundred per cent. Essentially all tape-punching errors and shaft encoder mis-readings were detected with the software written to collect the data. Only those scaler or timer errors which were less than the expected statistical error would not be detected. The standard reflection's intensity was observed to vary as much as 5 per cent. However, this change was over a period of several weeks and was linear over any time period less than a day. After the normalization carried out, the remaining error due to generator instability should be less than 0.1 per cent.

Systematic Factors

Absorption

The effects of absorption can, in principle, be corrected for if one knows: (1) the linear absorption coefficient of the specimen, (2) the shape of the specimen, and (3) the orientation of the specimen with respect to the primary and diffracted beam for each Bragg reflection observed. The absorption factor is:

$$A^{*}_{hk\ell} = \frac{V}{\int_V e^{-\mu x}\, dv} \quad , \tag{29}$$

where V is the irradiated volume of the specimen, μ is the linear absorption coefficient, and x is the total path length (primary and diffracted beam paths) in the specimen for the volume element dv. The integration is over the irradiated volume for the hkℓ reflection. In equation (29) the effects of extinction have been neglected. If the specimen is not completely bathed in the primary beam, the volume V will, in general, be different for each set of hkℓ. The integration of equation (29) can be simplified if one assumes certain special shapes and orientations for the specimen. For a spherically shaped specimen, A* is a function of only the Bragg angle and μR; where R is the radius of the sphere. For values of $\mu R \leq 0.2$, the absorption factor A* varies less than 1 per cent over the range of Bragg angles (θ) from 0° to 60°. For larger values of μR, tabulated values of A* may be found in the International Tables for X-Ray Crystallography. A major error in the absorption correction occurs in the determination of the specimen's radius and in the fact that the specimen is usually not a perfect sphere. Although A* (for values of $\mu R \leq 0.1$), may be reasonably considered a constant as the Bragg angle changes, the value of A* still has a marked dependence on μR. For a value of $\mu R = 0.1$ we find that $\frac{\partial A^*}{\partial \mu R} = 2$. For small values of μR (≤ 0.1), an error in determining μR will not affect the data (other than a change in scale), if the specimen is a perfect sphere. In practice, the specimens are not perfect spheres, but have, at the very least, small departures from sphericity. The proper radius for an approximating sphere is that radius for which equation (29) yields the correct value for A*. However, this effective radius differs for the various Bragg reflections, and the rapid variation in A* with respect to μR, results in an erroneous

absorption correction if a single value of R is used. Thus, the near constancy of A* with respect to θ is misleading for specimens which depart from sphericity. The value of R is usually chosen to yield a value of μR in the neighborhood of one. This value of μR will yield moderate intensities while, at the same time, the transmission factor will vary slowly with the Bragg angle.

Absorption correction errors can be reduced if one uses small (i.e., μR small) spheres. Radiation of shorter characteristic wavelength can be used to achieve a smaller value of μ for the specimen (because μ/p is proportional to λ^3 between absorption edges). Thus, at least for absorption-correction purposes, molybdenum Kα radiation would be preferred to copper Kα. For this work, all data were collected with MoKα radiation.

Extinction

The kinematical theory of x-ray diffraction is usually used in structure determination and refinement work. A major assumption in the kinematic theory is that of the absence of rescattering or multiple scattering. Kinematic theory predicts the scattered intensity $I_{hk\ell}$ for the hkℓ Bragg reflection to be proportional to the square of the structure amplitude, $|F_{hk\ell}|^2$. The dynamical theory of x-ray diffraction predicts $I_{hk\ell}$ to be proportional to the structure amplitude, $|F_{hk\ell}|$, for the special case of a perfect crystal of infinite extent, non-absorbing and in symmetrical reflection. For the crystals usually used in structure determinations the kinematical limit is approached. Departures of the intensities from proportionality with $|F|^2$ are referred to as extinction effects.

An accurate determination of the structure amplitudes will require application of an effective correction procedure to account for departures from the kinematical theory (extinction effects). The reduction of the intensities from the kinematical values can be ascribed to two mechanisms: (1) multiple scattering within a volume in which coherence between the scattered beams is maintained, and (2) reduction of the incident beam intensity for inner mosaic blocks by diffraction by outer mosaic blocks. The first mechanism is known as primary extinction, and the amplitudes of the various scattered beams must be added to obtain the total scattered intensity. With secondary extinction (the second mechanism), the intensities of the various scattered beams must be added to obtain the total intensity, because phase coherence is not maintained between the various blocks.

As mentioned previously, the effect of extinction is to decrease the intensities of the Bragg reflections. The strongest reflections are reduced in intensity the most, for both primary and secondary forms of extinction. Furthermore, the degree of extinction decreases with decreasing wavelength. The errors due to extinction can be reduced if one uses very small, mosaic crystals and a short wavelength for the incident radiation. Chandrasekhar, Ramaseshan, and Singh (1960) have devised a direct experimental method for the determination of the extinction correction factor. The method involves making two measurements of the intensity for each reflection, using x-rays which are polarized (i) perpendicular to and (ii) parallel to the plane of incidence. Since the polarization factor will, in general, differ for a perfect and an imperfect crystal, from these two measurements the

structure amplitude can be obtained free from the effects of both primary and secondary extinction. However, the method employs equations which have singularities at $\theta = 0^\circ$, 45°, and 90°.

Zachariasen (1963, 1967) has derived effective extinction correction factors from theory. The form of the correction in the 1963 paper is

$$|F_{corr}| \approx K|F_{obs}|(1 + \beta_{2\theta} C J_{obs}) \quad , \tag{30}$$

where $|F_{corr}|$ is the structure amplitude corrected for extinction, $|F_{obs}|$ is the observed structure amplitude, J_{obs} is the observed integrated intensity, K and C are adjustable scale factors and $\beta_{2\theta}$ is:

$$\beta_{2\theta} = \frac{2(1 + \cos^4 2\theta)}{(1 + \cos^2 2\theta)^2} \cdot \frac{A^{*\prime}(2\theta)}{A^{*\prime}(0^\circ)} \quad . \tag{31}$$

In equation (31), $A^{*\prime}(2\theta)$ is the derivative of the absorption factor with respect to μ at 2θ, and $A^{*\prime}(0)$ is the similar derivative at $2\theta = 0^\circ$. Equation (31) for $\beta_{2\theta}$ is for an unpolarized incident beam. One tacitly assumes in equation (30) that the specimen is what Zachariasen calls a type I crystal. For a type I crystal $r/\lambda g \gg 1$, where r is the mean radius of a perfect crystal domain, λ is the wavelength of the incident radiation, and $2g\pi^{\frac{1}{2}}$ is the reciprocal of the standard deviation associated with the isotropic Gaussian distribution of the orientations of the perfect crystal domains. For a type II crystal, $r/\lambda g \ll 1$. The

breadth of the angular distribution of mosaic blocks is much wider than the intrinsic angular width of the diffracted rocking curve from a single perfect domain with type I crystals. The reverse is true with type II crystals. The Borrmann effect becomes important with heavily absorbing type II crystals. As a result of the Borrmann effect, the intensity of a Bragg reflection undergoes an intensity enhancement rather than an extinction.

In his later paper Zachariasen (1967) developed an extinction correction valid for the full range from perfect to ideally imperfect crystals, for which the absorption is low. This new extinction correction is

$$|F_{corr}| \approx K|F_{obs}|(C'\beta_{2\theta}J_{obs} + (1 + (C'\beta_{2\theta}J_{obs})^2)^{\frac{1}{2}})^{\frac{1}{2}} \qquad (32)$$

and if one expands the radicals in equation (32) the following approximation for equation (32) is obtained,

$$|F_{corr}| \approx K|F_{obs}|(1 + \tfrac{1}{2} C'\beta_{2\theta}J_{obs} + \ldots) \qquad (33)$$

where higher powers in $C'\beta_{2\theta}J_{obs}$ have been omitted. Equation (33) reduces to equation (30) for small $C'\beta_{2\theta}J_{obs}$, if we allow the constant C in equation (30) to be equivalent to the constant $C'/2$ in equation (33). Thus equation (32), for small $C'\beta_{2\theta}J_{obs}(\leq 2)$, reduces to equation (30). For crystals of type II, those with high extinction and $\mu R \geq 0.5$, the extinction correction (32) has to be modified further to take into

account the Borrmann effect which is then no longer negiligible (Zachariasen, 1968).

Sudarsanan and Young (1969) have stressed the importance of performing an extinction correction to obtain physically significant precision, even when only a small degree of extinction exists. Without extinction corrections, they found differences, between the determination of the same thermal parameter in the various specimens, as large as 4σ. The unweighted R factor based on intensities was 5.4 per cent. A subsequent extinction correction reduced that R factor to 3.5 per cent, but, more significantly, the differences between all corresponding parameters (including the off-diagonal thermal parameters) were reduced to 1σ. Without the corrections for systematic errors in the intensities, due to a small degree of extinction, differences which were statistically but not physically significant would have been found between different specimens of the same material.

Correction of the intensities for systematic error due to extinction effects can be further complicated by anisotropy in the extinction effects. Both the sizes of the domains and the distribution of the misalignment of these domains may be anisotropic. Extinction anisotropy has been experimentally demonstrated with x-ray topographic techniques applied to a resonating quartz plate (Young and Wagner, 1966).

The extinction parameters may be determined experimentally or, as is the usual practice, they may be obtained among the results of a least-squares structure-refinement procedure. In the present work, the intensities from each specimen were corrected for extinction, using Zachariasen's (1963) correction incorporated into the least-squares

refinement program. An isotropic extinction correction was used because for the apatite samples used in this work significant anisotropy in the Bragg intensities (other than simultaneous diffraction effects) were not observed upon rotation of the specimens about the diffraction vector.

Thermal Diffuse Scattering

The incoherent inelastic scattering of the incident x-rays, by the various lattice vibrational modes (phonons) of the specimen, creates a background under the Bragg peaks which is not entirely removed by the usual background corrections. Thermal diffuse scattering involves the creation or annihilation of one or more phonons. The change in energy of the photon is small since the velocity of sound is small compared to the velocity of light. Thus, the elastically scattered Bragg photons are not energetically distinguishable, with the usual x-ray diffraction techniques, from the inelastically scattered photons (TDS). Fortunately, the multi-phonon scattering processes produce a slowly varying background which is, to a large degree, removed by the usual linear-background correction. However, the one-phonon scattering peaks exactly at the reciprocal-space positions of the Bragg reflections. Thus, a large part of the contribution of the one-phonon scattering to the integrated intensity is not removed by the usual methods of background correction.

A number of authors have consider analytical and numerical methods of determining the one-phonon contribution to the observed Bragg intensity (Nilsson, 1957; Cooper and Rouse, 1968; Lucas, 1969; Annaka, 1962; Lomer, 1966; Skelton and Katz, 1969). Young (1972) has reviewed

the problems involved in calculating the TDS contribution to the Bragg peak and the various attempts at solving these problems. O'Connor and Butt (O'Connor and Butt, 1963; Butt and O'Connor, 1967) have experimentally observed, with Mössbauer spectroscopy, the elastic and inelastic components of the scattered radiation. Since the intensities of Mössbauer sources are weak, this direct method of separating out the contribution of the inelastic scattering from the elastic is presently impractical for application to the thousands of Bragg reflections typically collected for a structure determination or refinement.

In principle, to evaluate the integrals which yield the intensity contributions of the various orders of TDS to the total intensity one needs detailed knowledge of the phonon dispersion curves of the specimen. In practice, this knowledge is not available and one must make certain simplifying assumptions in order to be able to evaluate the TDS contributions. One usually assumes that the one-phonon scattering by the acoustic modes is responsible for all observable peaking of the inelastic scattering about the reciprocal lattice point. Multiple-phonon scattering and scattering by optic modes are removed, to a good approximation (Cochran, 1969), by the background correction. The continuum or long-wavelength approximation is made, i.e., the dispersion curves of the acoustic modes are assumed to be linear for small wave numbers, corresponding to the volume of reciprocal space near a Bragg reflection. The high-temperature or classical and the harmonic approximations are made for the various normal modes of the crystal, thus the average energy kT can be assigned to each normal mode, where k is

Boltzmann's constant and T is the absolute temperature. Often, isotropy of the TDS about a relp is also assumed.

Aside from the above approximations made to facilitate the calculation of the one-phonon scattering, a complication of an experimental nature is that of determining the resolution function of the diffractometer. That is, to evaluate the one-phonon TDS integral, one must know which points of reciprocal space were sampled and with what weight for each point, for the particular experimental technique used. The resolution function is a convolution of several separate effects, such as source and specimen dimensions, mosaic spread, and the spectral distribution of the incident radiation. The resolution function can be determined experimentally (Cooper and Nathans, 1968), or, in what may be a preferable alternative, introduced into the least-squares refinements as additional adjustable parameters (Lucas, 1968; 1969).

The most significant effect, on the structure parameters, of neglect of the TDS contribution to the detected intensity, is the reduction of the apparent thermal parameters (Nilsson, 1957; Göttlicher, 1968). Thus, although the accuracy of the temperature factors obtained from intensity data which were not corrected for TDS will be poor, one should still be able to obtain high precision in the (incorrect) results for the temperature factors (with specimens maintained at the same temperature). Improvement in the accuracy of the temperature factors can be achieved if one collects the data from specimens which have been cooled, and/or calculates the TDS contribution for each Bragg reflection. While the accuracy of the temperature factors may suffer from the lack of an adequate TDS correction, the effects of TDS on the structure

amplitudes have been, to first approximation, accounted for by the application of a pseudo temperature factor.

For this work, explicit TDS corrections were not made. However, the multi-phonon contribution varies slowly with scattering angle and the linear background correction removes this from the apparent Bragg intensity. The one-phonon contribution (which peaks at the reciprocal lattice points) is not removed by this background correction and remains as a systematic error in the Bragg intensities. However, the one-phonon TDS scattering near the reciprocal lattice points is due primarily to long-wavelength phonons whose spectra are relatively unaffected (compared to short-wavelength phonons) by small differences in the atomic scale detail of the unit cell. Thus, for data collected at the same temperature from similar apatite specimens the precision in the structure amplitudes should be unaffected by the remaining one-phonon contribution.

Structural-Model Limitations

The accuracy, though perhaps not the precision, of the structure parameters obtained from least-squares refinements may be adversely affected by the limitations of the mathematical model used to calculate the structure amplitudes. The discrepancies between a hypothetically perfect set of observed structure amplitudes and a corresponding set of calculated structure amplitudes may be partially removed in the least-squares structure-refinement procedure by apparent changes (which do not have physical significance) in the structural parameters.

In what follows, the effect of asphericity of the form factors,

breakdown of the harmonic approximation, and anomalous dispersion on the calculated structure factors is discussed.

Asphericity of the Atomic Form Factors

If one makes the usual kinematic assumptions, the structure factor can be shown to be:

$$F(\bar{s}) = \int \rho(\vec{r}) e^{2\pi i \vec{S} \cdot \vec{r}} dv \qquad (34)$$

where S is the diffraction vector (i.e., the position vector in reciprocal space), and $\vec{r}$ is the position vector in direct space. The integration is carried out over the volume of the unit cell. Equation (34) is simply the Fourier transform of the electron density $\rho(\vec{r})$. The electron density ρ is actually the space-averaged electron density, where the average has been taken over many unit cells. Furthermore, ρ is also time-averaged, since the duration of an observation is long compared to thermal motion and the thermal motion is slow compared to the frequency of the incident radiation.

In practice, the electron density is assumed to be calculable from a linear superposition of discrete atoms. The Fourier transform over the unbound atom, whose electron density is spherically-averaged, yields the atomic form factor $\underline{f}$. Substituting the form factor $\underline{f}$ into equation (34) yields:

$$F(\bar{s}) = \sum_j f_j(s) T_j(\bar{s}) \exp(2\pi i \bar{s} \cdot \bar{r}_j) \quad , \qquad (35)$$

where f_j is the form factor for the j^{th} atom and T_j is a "smearing factor" which takes into account the effects of thermal motion.

The atomic form factors obtained in this way are subject to several deficiencies. One obvious fault is that the electrons are not usually distributed isotropically about the nucleus and the form factor $\underline{f}$ was obtained with the assumption of a spherical distribution. Generally speaking, this assumption will not hinder one's efforts in determining a structure (essentially all structure determinations which have been done have made use of the spherical atom approximation), but the non-spherical nature of some atoms in their crystal-field environment will affect the accuracy of the determination of the structure amplitudes. In an extreme case, a reflection which would otherwise be absent can be present because of a non-spherical charge distribution. The 222 reflection of diamond is the classic case of a reflection being present because of a non-spherical charge distribution (Dawson, 1967; Renninger, 1955). In this example, the covalent nature of the bond in diamond gives rise to an antisymmetric component in the electron density (Dawson, 1967).

Even in those instances where the spherical atom approach would be adequate, the atomic form factors in use can be significantly in error, since the wave functions for a free or isolated atom are usually utilized rather than the appropriate wave functions for the atom in its actual environment.

The aspherical nature of bonded atoms will primarily affect the valence electrons. The use of a short wavelength radiation, such as MoKα as used here, will permit the collection of substantially more

data at higher values of $\sin\theta/\lambda$, enabling one to use calculated structure amplitudes which are determined by that part of the f vs $\sin\theta/\lambda$ curve which is relatively unaffected by the valence states. This procedure would not be effective when accurate electron densities are desired and some formalism for the form factor curves should then be used which would allow for change in the atomic electron distribution due to bonding.

In the present work, the spherical atomic form factors of Cromer and Waber (1965) were used. The data were collected with the use of MoKα radiation and for $\sin\theta/\lambda > 0.3$ (in this region of $\sin\theta/\lambda$ the difference between the f factor for F^0 and F^{-1} is less than 1.5 per cent). The difference in the f factor curves (due to a change in valency) for the heavier atoms in apatite is even less (< 0.2 per cent for Ca). The errors in f due to an aspherical electron distribution should be even less than that expected for changes in valency.

Breakdown of Harmonic Approximation

The smearing function $T_j(\bar{s})$ which takes into account the effect of thermal motion of an atom on the scattering of x-rays, is usually used in the form (Cruickshank, 1956):

$$T_j = \exp(-(b_{11}h^2 + b_{22}k^2 + b_{33}\ell^2 + 2b_{12}hk + 2b_{13}h\ell + 2b_{23}k\ell)) \quad . \quad (36)$$

Equation (36) assumes that terms higher than quadratic in the expansion of the potential energy of the j^{th} atom can be neglected. With this harmonic assumption, the motion of the atoms can be described by ellipsoids. The surface of the ellipsoid forms an iso-probability surface

for encompassing of the center of the vibrating atom. The Fourier transform of this motion (another ellipsoid) yields the function T_j. Thus, the thermal parameters b_{ij} will describe a general ellipsoid in reciprocal space which will degenerate to a sphere for sites with cubic symmetry.

The harmonic approximation may break down because of the librational motion of the atoms or some other collective motion involving non-independent motion of the atoms. Also, higher order terms (cubic, etc.) may be important in the expansion of the energy of the atoms (becoming increasingly more important at higher temperatures).

The effects of anharmonicity have been reported to have been observed with neutron diffraction studies on fluorite (Willis, 1965) and on UO_2 (Rouse, Willis, and Pryor, 1968). An atom at a site of cubic symmetry does not necessarily have an isotropic smearing function. Departures from spherical symmetry (which satisfy the site symmetry) can occur if anharmonic forces are present. Anisotropic temperature factors were observed (Willis, 1965) for the anion of the fluorite structure. This anisotropy in the temperature factor of an atom located at a site of cubic symmetry was attributed to the breakdown of the harmonic approximation. The R factor of the least-squares refinement improved significantly (0.68 to 0.32 per cent) (Rouse, Willis, and Pryor, 1968) when a physically logical tetrahedral distortion was introduced into the smearing function of the anion.

In the present work, all of the specimens were fluorapatite or chlorapatite with small (< 3 weight per cent) substitutions of fluorine or neodymium. Thus, the basic structures of all the specimens were very

similar and hence, any differences in the structure amplitudes due to differences in anharmonicity (the effects of anharmonicity being small to begin with) should be negligible as far as precision is concerned.

Anomalous Dispersion

The assumption of scattering by free electrons is quite good as long as the energy of the incident photon is large compared to the binding energies of the electrons. This requirement is usually met for light atoms; however, for heavier atoms the K electrons are bound significantly even though weakly. Whenever the energy of the incident radiation approaches that of any of the absorption edges of the atoms, resonance absorption occurs and the phenomenon of anomalous dispersion results.

The electrons are treated as weakly bound harmonic oscillators and the Rayleigh scattering of x-rays is calculated as a correction to the atom form factor f. Since the major anomalous dispersion corrections arise from the x-rays scattered by the bound inner electrons, the corrections are effectively independent of the scattering angle. After anomalous dispersion correction have been applied, the atomic form factor becomes

$$f = f_0 + \Delta f' + i\Delta f'' \quad , \tag{37}$$

where f_0 is the form factor calculated for Thomson scattering, $\Delta f'$ is the real part of the dispersion correction to the form factor due to Rayleigh scattering, and $\Delta f''$ the imaginary part of the correction due to resonance absorption. Thus, we see that the atomic form factor is in

general a complex factor, the modulus of which determines the amplitude of the scattering. The form factor f could be represented as

$$f = |f|e^{i\phi} \tag{38}$$

where

$$\tan\phi = \frac{\Delta f''}{f_o + \Delta f'} \quad . \tag{39}$$

If corrections to f_o for anomalous dispersion are not made, observable errors will occur in the least-squares refinements of the structure parameters (Ueki, Zalkin, and Templeton, 1966; Cruickshank and McDonald, 1967). Failure to account for the advancement in phase of the scattered beam due to the dispersion corrections results in an apparent shift in position of the resonant atom along the diffraction vector. The magnitude of the shift $|\Delta r|$ is

$$|\Delta r| = \frac{\phi}{2\pi|\vec{S}|} \tag{40}$$

where ϕ is the advancement in phase due to anomalous dispersion and $|\vec{S}|$ is the magnitude of the diffraction vector. For centrosymmetric space groups the average shift $\langle\Delta r\rangle$ will be zero; however, the average square displacement $\langle\Delta r^2\rangle$ will not be equal to zero. The result will be that positions are unaffected while the isotropic component of the temperature

factors of the resonant atoms will be in error because of the neglect of anomalous dispersion. For non-centrosymmetric space groups, neglect of the anomalous dispersion correction will result in $\langle \Delta r \rangle \neq 0$ if an incomplete set of data is collected. This is a consequence of the fact that Friedel's law no longer holds true if the correction $\Delta f''$ is significant.

The anomalous dispersions constants $\Delta f'$ and $\Delta f''$ are now tabulated for many atoms and incident radiations. Both the real and imaginary parts of the anomalous dispersion corrections (Cromer, 1965) have been included in all parts of this work.

CHAPTER IV

EXPERIMENTAL APPROACH

Selection of Specimens

Apatites were chosen for examination, among other reasons, because their basic structure is already well known (Brown, W. E. and Young, R. A., 1972) and hence the determination of the phases of the structure amplitudes would not present any undue hindrance. Furthermore, flux-grown apatites were chosen rather than the naturally occuring apatites which are noted for the variety of atomic species which may occur as substitutions or defects in the apatite structure. By carefully controlling the composition of the flux, one can obtain apatites of a high degree of purity and can thereby greatly reduce the effects which unknown and variable compositions would have on the structure amplitudes.

Fluorapatite ($Ca_{10}(PO_4)_6F_2$) and chlorapatite ($Ca_{10}(PO_4)_6Cl_2$), both of which had compositions which were essentially stoichiometric, were chosen for observations as well as several fluor-chlorapatites of two different F/(F+Cl) ratios. Hereinafter, fluorapatite and chlorapatite will be referred to as FAp and CLAp respectively. Two fluorapatite specimens which were doped with neodymium (FAp:Nd) were also investigated. The source of neodymium in one FAp specimen was Nd_2O_3 in the melt, whereas NdF_3 was used in the melt to produce the other Nd-doped FAp. The interest in the FAp:Nd specimens lies in their

potential use as laser materials. The FAp:Nd material obtained with NdF_3 in the melt has proved to be the poorer laser host of the two despite its higher optical quality and greater growth rate (Eaglet, 1970). The composition of the melt was such that the resulting crystals should contain approximately 0.4 weight per cent of Nd, if a segregation coefficient of one is assumed. It has been suggested that Nd substitutes for Ca in the apatite structure (Mazelsky, Ohlmann, and Steinbruegge, 1968; Eaglet, 1970). Because of the multiplicity of Ca sites which the Nd may be distributed among, it was recognized that the precision structure refinement techniques (including data collection) would be severely tested in locating the Nd. The question of how charge balance is maintained is also raised because of the substitution of the trivalent Nd^{+3} for the divalent cation Ca^{+2}. Several self-compensating mechanisms for charge balance exist and will be discussed later.

Specimen Preparation

For single-crystal intensity measurements, one requires a crystal which is free from cracks and inclusions, is untwinned and, of course, is single. In practice, the specimens are mosaic but the mosaic spread should be small enough so that the spots on a Laue photograph will be well defined (half-width of the mosaic distribution $\leq 1^{\circ}$). Of course, one must keep in mind that extinction effects will become greater as the crystal becomes less mosaic. Laue photographs were taken of each specimen used in this work and examined for evidence of a multiple-crystalline nature which would make them unsuitable for single-crystal measurements.

Each prospective specimen used in this work was examined optically with a polarizing microscope while the specimen was immersed in a refractive index oil which closely matched the average index of refraction of the crystal. It was required that the specimens appear homogeneous under crossed polarizers, indicating single crystals free from stain, to be accepted for data collection with the diffractometer. The possibility that the specimens were twinned was checked further before data collection with the diffractometer was begun. Weissenberg or precession photographs, or both, were taken of each prospective specimen and examined for evidence of twinning or any other unusual character in the scattering which would be difficult to detect with counter methods.

Lattice constants and indices of refraction were determined for each specimen (see Table 2). Lattice constants were measured with the single-crystal diffractometer. Indices of refraction were measured with the help of calibrated index oils.

Prior to any x-ray work being done on it, each specimen was ground to a spheroidal shape. The samples were ground in a cylindrical cavity, the wall of which was lined with a diamond abrasive grit. The material was made to tumble in a circular path by means of a jet of dry air. As the material rubbed against the abrasive coated wall a spherical shape developed.

The spherical shape permitted the use of an absorption correction which was a function of 2θ only. The resulting spheres were ground until their radii were such that the corresponding values of μr were $\sim$ 1, insuring that the transmission factor would vary slowly with 2θ. Crystals with small volumes will increase the total time of the experiment

Table 2. Specimen Characteristics

Specimen	a(Å)	b	c(Å)	n_ω	n_ϵ	NOMINAL COMPOSITION (wt %) Ca	PO_4	Cl	F	Nd
G-6-6-1	9.623	b = a	6.779	1.646	1.646	38.7	54.5	6.4	0.4	-
G-6-6-3	9.619	b = a	6.778	1.646	1.646	38.7	54.5	6.4	0.4	-
NdF_3-FAp-2	9.380	b = a	6.885	1.635	1.630	36.4	57.0	-	3.4	3.3
Nd_2O_3-FAp-1	9.383	b = a	6.887	1.642	1.640	36.2	57.1	-	3.4	3.3
G-10-1	9.552	b = a	6.825	1.652	1.650	38.8	54.8	5.1	1.3	-
Syn FAp 35-7	9.366	b = a	6.884	1.633	1.629	39.7	56.5	-	3.8	-
Syn ClAp L1-24	9.628	b = 2a	6.764	1.668	1.669	38.5	54.2	6.7	-	-

if one tries to maintain the statistical precision, however, the effects of extinction and multiple Bragg scattering on the structure amplitudes will decrease as the volume is decreased (see equation (32) Chapter 3). The maximum and minimum radii of the specimens used in this work are 0.349 mm and 0.159 mm, respectively.

Data Collection Strategy

Writing and checking the control program for the computer-controlled diffractometer, although seemingly ancillary to the main purpose of the investigation, did require a considerable effort. About one man year was used in modifying and making extensive additions to the programs supplied with the FACS-I system. The resulting control program has been described at meetings (Mackie, 1971; Young and Mackie, 1971) and further detailed descriptions are given in Appendixes A and C. Written descriptions have also been distributed to various laboratories in response to requests.

The salient features of the data-collection strategy, selected on the basis of the considerations in Chapter III and incorporated in the control program, are discussed briefly in the following paragraphs.

Two-Pass Method

The data for each Bragg reflection were collected in two passes. In the first-pass, a rough experimental determination was made of the signal-to-noise ratio and integrated intensity of the Bragg reflection. This information was used to adjust the ratio of the time spent on the peak to the time spent determining the background. The optimum time

Page missing from thesis

were designed to allow the data collection to proceed uninterrupted and to include error flags in the output data which would indicate the nature of the error or malfunction. Programmatic tests were made for filter balance, unexpected character in the background, diffractometer collision, and bad readings of the shaft encoders.

Selection of Reflections

Reflections to be observed were chosen by one of two methods: (1) by any programmable method by altering the (h,k,ℓ) selection subroutine, (2) from a list of reflections stored on the disk. Standard reflections were placed into the data collection at specified time intervals by making use of the programmable hardware clock in the FACS-I system.

CHAPTER V

ANALYTICAL APPROACH

Data Reduction

Absorption Factor

The spherical shapes of the samples and the relatively short wavelength (MoKα) used in this work simplified the absorption-correction problem (see Chapter IV). The relative intensities were corrected for absorption by multiplying them by A*, the reciprocal of the transmission coefficient A. For a spherical specimen, A* is a function of two independent variables, the Bragg angle θ and μR (μ is the linear absorption coefficient and R the radius of the specimen). To obtain A* for a specific μR value and Bragg reflection, a four-point bivariate interpolation procedure was performed, on tabulated data (International Tables for X-Ray Crystallography, 1969):

$$A^*_{i+\Delta,j+\epsilon} \approx (1-\Delta)(1-\epsilon)A^*_{i,j} + \Delta(1-\epsilon)A^*_{i,j+1} + \epsilon(1-\Delta)A^*_{i+1,j}$$

$$+ \epsilon\,\Delta A^*_{i+1,j+1} \quad , \tag{41}$$

where $A^*_{i,j}$ is the table entry for A* at the i^{th} row j^{th} column, Δ and ϵ are the fractional differences of the inter-row and inter-column

spacings to obtain A* at the desired values of μR and θ. The value of the linear absorption coefficient used was:

$$\mu = \rho \sum_j p_j \left(\frac{\mu}{\rho}\right)_j \quad , \tag{42}$$

where ρ is the density of the crystal, $\left(\frac{\mu}{\rho}\right)_j$, is the mass absorption coefficient for element j and p_j is the percentage, by weight, of element j in the crystal. Table (3) lists the values of R, μR, and μ for the crystals which were used. For $\mu R = 0.48$, A* changes by about 6 per cent over the range of θ used. For the worst case, $\mu R = 1.08$, A* changes by about 27 per cent.

Lp Factor

The data were corrected for polarization and the Lorentz factor

$$(Lp)^{-1} = \sin(2\theta)/(1+\cos^2(2\theta)) \quad . \tag{43}$$

In equation (43) an unpolarized incident beam is assumed and that the specimen was treated as ideally mosaic. Departures from the ideal mosaic behavior produced extinction effects which were corrected for with the Zachariasen method (Zachariasen, 1963).

Normalization of the Intensities

A plot of the periodically-observed intensity of the standard reflection versus time was made for each sample and displayed on the storage-scope display. From this display one could see any anomalous behavior of the intensity of the standard reflection versus time. If

Table 3. Linear Absorption Coefficients and Radii of Specimens Used.

Specimen	(Cm^{-1})	R(Cm)	μR
G-6-6-1	30.9	0.0310	0.96
G-6-6-3	30.9	0.0349	1.08
NdF_3-FAp	33.3	0.0302	1.01
Nd_2O_3-FAp	33.3	0.0238	0.79
G-10-1	31.3	0.0159	0.50
Syn FAp	31.7	0.0165	0.52
Syn ClAp	30.8	0.0155	0.48

the intensity of the standard reflection was constant within 3 standard deviations throughout the data collection run, the data were not normalized. Otherwise, a 2nd degree polynomial was fitted to the series of standard intensities by conventional least-squares techniques (see Figures 8 and 9, Chapter III). The data were then normalized to this 2nd degree polynomial.

Observed Zeroes

The intensities of those reflections for which the experimentally derived net integrated intensities were less than $+3\sigma$ (where σ is the standard deviation due to counting statistics only) were set equal to zero. These reflections were included in subsequent least-squares refinements of the structures with weights which were equal to the reciprocals of the variances of the respective reflections.

Flagged Data Which Were Not Used

The teletype output for each reflection occupied one line. One column of this line was reserved as space for an error-code indicator. There were eight error conditions which were recognized and flagged with an integer (1 through 8). A reflection was consider unacceptable for least-squares refinement if its error-code indicator was non-zero.

The error code "1" indicated that the net integrated intensities obtained at the two settings of the diffraction vector differed by more than three standard deviations (the standard deviation used was that obtained from counting statistics for one of the integrated intensity measures). An error code "2" indicated that the background obtained with the α-filter exceeded the background obtained with the β-filter by more than 4σ. An error code "3" indicated either a lack-of-balance

of the α-β filter pair or implied angular dependence of the non-Bragg scattered radiation of pass-band wavelengths.

Error codes "4", "5", "6", and "7" were used to indicate bad encoder readings on the 2θ, ω, χ, and ϕ axes, respectively. Error code "8" indicated that a collision had occured while the reflection was being scanned.

Visual Monitoring

Before least-squares refinements were started, the intensity profile of each reflection was checked visually on the strip-chart recording, for any signs of unusual character or structure which would disqualify that reflection from inclusion in the least-squares refinements. Any indication of a peak in the intensity profile, other than that due to the $K\alpha_1$ and $K\alpha_2$ wavelengths of Mo, resulted in an automatic rejection of that reflection. Furthermore, a reflection was removed from the data set if the ratio of the $K\alpha_1$ peak to the $K\alpha_2$ peak did not roughly satisfy the 2:1 relationship.

Least-Squares Refinements

Least-squares refinements involve the adjustment of the various independent variables of a structural model until a best fit, in a least-squares sense, is obtained between the sets of observed and calculated intensities. Since the intensities of the Bragg reflections are non-linear functions of the parameters of the structure model, it becomes efficacious for one to linearize (keep the first two terms of a Taylor's series expansion) the system of equations obtained by minimizing the agreement factor with respect to the variable parameters of

the model. As a result of the linearization, second and higher order derivatives of the calculated intensities (or the calculated structure factors if the agreement factor is based on differences in the observed and calculated structure amplitudes) are ignored. The "best-fit" parameters are not determined by the straight forward first solution of the linearized normal equations since the higher order derivatives have been ignored. Because of the non-linear nature of the structural model, the second and successive solutions to the normal equations do not, in general, yield zero changes in the parameters (for each cycle of refinement one uses the values of the parameters obtained in the previous solution of the normal equation). The parameters are adjusted by successive cycles of least-squares adjustments until the parameter shifts are smaller than their estimated standard deviations. The refinement process is prolonged if two or more parameters are strongly correlated since the correlations are not properly handled in the linearized version of the normal equations. In cases of strong correlation, it may become impossible to vary simultaneously the parameters which are strongly correlated without the least-squares process diverging from the true solution or an ill-conditioned matrix occurring.

Anomalous Dispersion and Extinction Corrections

The least-squares program used was that written by Busing, Martin, and Levy (1962), and modified by many different users. A modification to include anomalous dispersion corrections, corrected both the real and the imaginary parts of the atomic scattering factor $\underline{f}$. The anomalous dispersion constants which were used in this work were those computed by Cromer (1965). The corrections $\Delta f'$ and $\Delta f''$ for the

real and imaginary parts of $\underline{f}$ are independent of the scattering angle, 2θ, for molybdenum Kα wavelengths and the atoms which occur in apatite. The extinction correction (Zachariasen, 1963) was added by Sudarsanan (1967). The extinction correction (see equations 30 and 31, Chapter III) was applied to the observed structure amplitude and the constants K and c were obtained from least-squares, in a separate cycle from the least-squares adjustment of the other variable parameters. The adjustment of K and $\underline{c}$, of the extinction correction, was not incorporated into the system of normal-equations, consequently, the least-squares adjustment of K and $\underline{c}$ had to be iterated alternately with the adjustment of the other parameters to overcome the effects of correlation between the extinction parameters and the other parameters which were varied.

Weighting Scheme

Ideally, in a least-squares adjustment, one wants to place more weight on those data which are the most reliable. One widely used method of trying to achieve this objective is the weighting of the data by the reciprocal of their individual variances. In the present work, the variances in $|F|^2$ were obtained from the fact that $\sigma(|F|^2)/|F|^2 = \sigma(I_N)/I_N$, the latter being obtained from

$$\sigma(I_N) = \left[1 + \frac{1 + (1 + S)^{\frac{1}{2}}}{S}\right]^{\frac{1}{2}} \left(I_N\right)^{\frac{1}{2}} \qquad (44)$$

where S is the signal-to-noise ratio of the Bragg peak and I_N is its net integrated intensity. If the total variance of each datum point is assigned accurately, the expression

$$S^2 = \sum_i (\Delta F_i^2/\sigma_i F_i)^2/(m-n) \qquad (45)$$

will have a value close to unity. The term ΔF_i^2 is the difference between the observed and calculated F^2 for the i^{th} reflection, while F_i is its structure amplitude, m is the number of observations and n is the number of variables. The factor S^2 is an estimate of the variance of an observation of unit weight. S^2 can depart from unity due to several causes; the weights may be assigned wrongly, the refinement process may not have converged yet, and the structural model used may be inherently incapable of duplicating a set of, hypothetically, error-free intensity observations for the actual specimen.

Multiple-Component Structure Models

The calculated structure factors used in least-squares refinements are usually obtained from:

$$F_{hk\ell} = \sum_i^n f_i \exp(2\pi i(hk_i + ky_i + \ell z_i)) \quad , \qquad (46)$$

where x_i, y_i, and z_i are the co-ordinates of the i^{th} atom and there are n atoms in the unit cell. (In practice, full use is made of the symmetry of the unit cell and the sum is carried out over the atoms in the asymmetric unit on a symmetrized version of equation (46)). The intensity of the h, k, ℓ reflection is proportional to $F_{hk\ell}F_{hk\ell}^*$ after due consideration has been given to such factors as extinction, simultaneous diffraction, absorption, polarization, etc. However, the implicit assumption has been made that throughout the volume of the crystal,

the content of each "unit cell" is the same(*). In real crystals, this homogeneity from "unit cell" to "unit cell" can be lost because of displacement disorder and substitutional disorder. Substitutional disorder can arise from substitutions of vacancies as well as from the substitution or different atomic species. Displacement disorder is the static distribution of atoms about a set of equivalent sites as opposed to the distribution due to the dynamics of the thermal motion.

These variations in the unit cells contents can be incorporated, in some cases, into the least-squares refinements. The ease with which this can be done varies greatly with the type of inhomogeneity. In the event that these "defects" occur in randomly chosen unit cells then a least-squares refinement can be made easily since the refinement is made on the contents of an average "unit cell." That is, to simulate substitutional disorder, one could place two or more atoms at one site in the model of the unit cell, and refine their respective site occupancy factors. The refined site occupancy factors would yield the fraction of such sites occupied by each atomic species. For those specimens in which the various distinct unit cells occur randomly throughout the specimen such an amplitude-adding model is sufficient. However, if the "defects" do not occur randomly but with some correlation, the amplitude adding model is no longer adequate. An extreme departure from the amplitude-adding limit occurs when the scattering from different volumes is independent and the intensity is obtained by adding the intensities

---

(*) In fact, the unit cell is by definition a unit which is repeated exactly to build up the entire crystal.

from the various independent volumes. (For example, merohedral twinning in a specimen can be handled by using a multiple-component intensity-adding least-squares model. In favorable cases, the ratio of the twin volumes can be obtained from a rather simple least-squares process; Sudarsanan and Young, 1970). The amplitude-adding multi-component model was used exclusively in this work to study substitutional disorder, displacement disorder, and non-stoichiometry in the fluor-chlorapatites.

CHAPTER VI

EVALUATION OF PRECISION TECHNIQUES

Introduction

In this chapter, some of the factors which can affect the attainable precision of the structure amplitudes are considered. Experimental evaluations of the effect of these factors were made and the discussion is limited to the effect on the precision of the final least-squares parameters. The physically interesting details of the several different apatite structures studied are not considered here, but are discussed in detail in Chapter VII.

Random errors were added to a set of experimentally observed intensities to determine what effect, if any, this would have on the least-squares parameters. Data were also collected at essentially two different acquisition rates to test the apparent difference in precision between the "typical" and "controlled-precision" scanning techniques. The frequency of occurrence of simultaneous diffraction under various conditions was studied, as well as the effect of simultaneous diffraction on the least-squares adjusted structural parameters. Other correction factors considered are extinction and anomalous dispersion.

Two samples obtained from the same fragment of fluor-chlorapatite were studied with the same technique ("controlled-precision" scanning) to assess the physical reality of specimen-to-specimen differences.

Random Errors

The effect of random normal errors on convergence and on the adjustable least-squares parameters was investigated. The data collected from the synthetic chlorapatite crystal, ClAp L1-24 were used in least-squares structure refinements (i) as initially obtained and after (ii) 5 per cent and (iii) 25 per cent random error had been added to them by the following means.

A set of random numbers drawn from a normal population was obtained when repeated fixed time counts were made of quanta arriving from an x-ray source. The set of counts (scalar readings) was converted to a set of standard normal deviates, d_i, by means of the transformation:

$$d_i = (S_i - \mu)/\sigma \quad , \tag{47}$$

where S_i is the i^{th} reading of the scalar, μ is the arithmetric mean of the n readings of the scalar, and σ is the standard deviation of the set of scalar readings. The first four moments of the distribution of d_i were compared with the values expected theoretically. The distribution of d_i was thus verified to be normal with a mean of zero and a standard deviation of one. In addition to the original data, two more sets of data were prepared from the original with random error contributions calculated from the d_i. The intensities with random errors added were then obtained with the following equation:

$$I'_{OBS_i} = I_{OBS_i}(1 + (RE)d_i) \quad , \tag{48}$$

where RE is the fractional standard deviation for the distribution of standard-normal deviates d_i and I_{OBS_i} are the observed intensities. The final refined parameters, positional and thermal, and individual site occupancy factors are presented in Table 4. All parameter values in Table 4 have been multiplied by 10^4. Standard errors are indicated in parentheses after each parameter value. The refinements, in each case, were continued until all parameter shifts were less than the associated standard deviations. The number of observations was 2232 and individual weights based on counting statistics were used. Both a weighted (wR_2) and an unweighted R factor (R_2) based on $|F|^2$ were used as indicators of agreement:

$$R_2 = \frac{\sum \left| |F_o|^2 - |F_c|^2 \right|}{\sum |F_o|^2} \tag{49}$$

and

$$wR_2 = \frac{\left(\sum w \left(|F_o|^2 - |F_c|^2 \right)^2 \right)^{\frac{1}{2}}}{\left(\sum w |F_o|^4 \right)^{\frac{1}{2}}} \quad , \tag{50}$$

where w is the reciprocal of the variance for each observation and the summation is carried out over all observations. The weighted R factor (wR_2) increased from 3.5 per cent for RE equal to 0.0 to 9.7 per cent and 28.8 per cent for RE equal to 0.05 and 0.25, respectively. As is shown in Table 4, nearly all parameters (94 per cent of the 210

Table 4. Final Least-Squares Parameters of Chlorapatite: Data Used Which Had Random Errors Added.

ATOM	RE*	MULT	x	y	z	β_{11}	β_{22}	β_{33}	β_{12}	β_{13}	β_{23}
O_{Ia}	0%	1.017(10)	3436(1)	4960(1)	2563(3)	52(2)	10(1)	37(2)	18(1)	- 5(2)	- 1(1)
	5%	1.002(18)	3437(2)	4963(2)	2564(3)	50(3)	9(1)	44(4)	18(1)	- 3(2)	1(1)
	25%	1.035(45)	3440(5)	4972(4)	2569(6)	49(6)	8(3)	49(8)	17(3)	- 2(3)	2(3)
O_{Ib}	0%	1.008(9)	4924(1)	3241(1)	7554(3)	38(1)	3(1)	38(2)	0(1)	- 1(2)	- 1(1)
	5%	0.995(18)	4921(2)	3239(2)	7558(3)	37(2)	3(1)	39(4)	0(1)	0(2)	- 1(1)
	25%	1.011(45)	4914(5)	3235(4)	7560(6)	42(5)	3(3)	52(8)	4(2)	3(3)	0(3)
O_{Ic}	0%	1.018(9)	1485(1)	5783(1)	2480(3)	16(1)	13(1)	39(2)	7(1)	- 2(2)	- 1(1)
	5%	1.012(16)	1484(2)	5784(2)	2481(3)	14(2)	14(1)	44(3)	7(1)	- 3(2)	- 1(1)
	25%	1.035(40)	1474(5)	5776(4)	2480(5)	17(4)	15(3)	44(7)	7(2)	- 3(3)	- 4(2)
O_{IIa}	0%	0.993(9)	5923(1)	4827(1)	2391(3)	16(1)	7(1)	59(3)	3(1)	7(2)	0(1)
	5%	0.989(16)	5925(2)	4830(2)	2393(3)	15(2)	6(1)	61(4)	3(1)	4(2)	2(1)
	25%	0.964(38)	5923(4)	4831(4)	2390(6)	10(4)	6(3)	56(7)	2(2)	1(3)	5(3)
O_{IIb}	0%	1.012(9)	5342(1)	3138(1)	2447(3)	25(1)	9(1)	65(3)	8(1)	- 3(2)	- 1(1)
	5%	1.034(18)	5340(2)	3136(2)	2448(3)	27(2)	9(1)	80(5)	10(1)	- 5(2)	- 3(1)
	25%	1.042(42)	5347(5)	3136(4)	2447(7)	30(5)	10(3)	98(11)	15(2)	- 3(3)	- 6(3)
O_{IIc}	0%	0.996(10)	1269(1)	5462(1)	7367(3)	28(1)	5(1)	58(4)	5(1)	5(2)	4(1)
	5%	1.029(17)	1269(2)	5462(2)	7365(3)	29(2)	7(1)	66(5)	7(1)	3(2)	3(1)
	25%	1.096(43)	1262(5)	5461(4)	7364(6)	33(5)	10(3)	78(9)	1-(2)	0(3)	3(3)
O_{IIIa}	0%	1.014(11)	3414(2)	3805(1)	769(3)	70(2)	11(1)	44(4)	16(1)	-32(2)	-10(1)
	5%	1.007(17)	3414(2)	3805(2)	771(4)	66(3)	10(1)	48(5)	17(1)	-31(2)	- 9(2)
	25%	0.975(37)	3407(5)	3801(4)	777(8)	63(5)	8(3)	52(8)	16(2)	-27(5)	- 8(3)
O_{IIIb}	0%	0.992(11)	7359(2)	2918(1)	723(4)	34(2)	8(1)	50(5)	3(1)	19(2)	- 4(1)
	5%	0.988(16)	7356(2)	2918(1)	719(4)	34(2)	8(1)	46(4)	2(1)	16(2)	- 6(2)
	25%	1.039(38)	7346(4)	2913(3)	711(7)	31(4)	13(3)	51(7)	1(2)	13(4)	- 8(3)
O_{IIIc}	0%	0.991(11)	827(2)	4206(1)	5773(3)	41(2)	15(1)	38(4)	17(1)	-13(2)	-13(1)
	5%	1.006(16)	828(2)	4206(2)	5768(4)	39(2)	17(1)	35(4)	17(1)	-12(2)	-14(2)
	25%	1.014(35)	824(4)	4203(3)	5760(6)	41(4)	13(3)	29(6)	17(2)	-11(3)	-14(3)
O'_{IIIa}	0%	1.012(10)	3642(2)	3865(1)	4414(3)	43(2)	10(1)	39(3)	13(1)	16(2)	7(1)
	5%	1.006(16)	3646(2)	3868(1)	4414(4)	43(2)	9(1)	39(4)	12(1)	18(2)	6(2)
	25%	0.948(35)	3650(4)	3871(3)	4418(7)	41(5)	6(3)	34(6)	11(2)	15(4)	2(3)
O'_{IIIb}	0%	0.972(10)	7301(2)	2949(1)	4371(4)	35(2)	7(1)	34(4)	3(1)	-18(2)	4(1)
	5%	0.996(16)	7301(2)	2952(1)	4380(4)	34(2)	8(1)	44(4)	3(1)	-13(2)	5(2)
	25%	1.040(38)	7300(4)	2951(3)	4388(7)	30(4)	10(3)	58(7)	1(2)	- 6(4)	8(3)
O'_{IIIc}	0%	0.990(10)	893(2)	4325(1)	9420(3)	27(2)	12(1)	37(3)	9(1)	3(2)	11(1)
	5%	1.013(15)	895(2)	4328(2)	9420(3)	29(2)	13(1)	30(4)	10(1)	4(2)	11(2)
	25%	1.026(35)	896(4)	4330(3)	9422(6)	32(4)	14(3)	30(6)	12(2)	7(3)	14(3)
Ca_I	0%	0.959(4)	3275(0)	5811(0)	34(1)	26(1)	7(0)	19(1)	6(0)	0(0)	- 1(0)
	5%	0.962(5)	3276(1)	5812(0)	33(1)	27(1)	7(0)	21(1)	6(0)	0(0)	- 1(0)
	25%	0.981(12)	3277(1)	5812(1)	32(2)	30(1)	8(1)	28(2)	8(1)	1(1)	- 1(1)
Ca'_I	0%	0.953(4)	3388(0)	5856(0)	4966(1)	25(1)	7(0)	16(1)	7(0)	0(0)	0(0)
	5%	0.950(5)	3388(1)	5857(0)	4967(1)	25(1)	7(0)	17(1)	7(0)	0(0)	- 1(0)
	25%	0.960(11)	3389(1)	5857(1)	4968(2)	26(1)	8(1)	23(2)	8(1)	- 1(1)	- 1(1)
Ca_{IIa}	0%	0.962(3)	2594(0)	2523(0)	2481(1)	23(0)	7(0)	25(0)	6(0)	3(0)	1(0)
	5%	0.956(5)	2594(1)	2523(0)	2480(1)	22(1)	8(0)	26(1)	6(0)	3(0)	0(0)
	25%	0.969(13)	2593(1)	2523(1)	2479(1)	24(1)	10(1)	32(2)	9(1)	2(1)	0(1)
Ca_{IIb}	0%	0.965(2)	53(0)	6229(0)	7481(1)	27(0)	7(0)	26(0)	8(0)	0(1)	2(0)
	5%	0.958(5)	53(1)	6230(0)	7482(1)	28(1)	7(0)	29(1)	9(0)	1(0)	3(0)
	25%	0.966(13)	54(1)	6229(1)	7481(2)	28(1)	8(1)	38(2)	10(1)	1(1)	3(1)
Ca_{IIc}	0%	0.962(3)	2549(0)	3798(0)	7513(1)	27(0)	6(0)	25(0)	5(0)	2(0)	1(0)
	5%	0.961(5)	2550(1)	3798(0)	7513(1)	28(1)	6(0)	25(1)	5(0)	1(0)	1(0)
	25%	0.991(13)	2551(1)	3799(1)	7513(1)	30(1)	8(1)	32(2)	7(1)	1(1)	0(1)
P_a	0%	1.026(3)	4077(0)	4377(0)	2531(1)	18(0)	4(0)	22(1)	5(0)	- 1(1)	0(0)
	5%	1.025(7)	4077(1)	4377(1)	2532(1)	18(1)	4(0)	23(1)	5(0)	- 1(1)	0(0)
	25%	1.044(17)	4076(2)	4377(1)	2532(2)	21(2)	5(1)	29(2)	7(1)	- 1(1)	0(1)
P_b	0%	1.024(3)	6245(0)	2665(0)	2522(1)	16(0)	4(0)	21(1)	3(0)	0(1)	0(0)
	5%	1.023(7)	6246(1)	2665(1)	2523(1)	16(1)	4(0)	24(1)	3(0)	1(1)	0(0)
	25%	1.026(17)	6246(2)	2666(1)	2524(2)	15(2)	4(1)	28(2)	3(1)	1(1)	0(1)
P_c	0%	1.027(3)	324(0)	4538(0)	7516(1)	15(0)	5(0)	22(1)	4(0)	- 1(1)	- 1(0)
	5%	1.037(7)	324(1)	4539(1)	7518(1)	15(1)	6(0)	24(1)	5(0)	- 1(1)	- 1(0)
	25%	1.068(17)	323(1)	4539(1)	7520(2)	17(2)	8(1)	33(2)	6(1)	- 1(1)	- 2(1)
Cl	0%	0.932(4)	15(1)	2494(0)	4439(1)	28(0)	7(0)	92(1)	7(0)	1(1)	- 1(1)
	5%	0.921(5)	16(1)	2494(1)	4443(2)	30(1)	8(0)	91(2)	8(0)	0(1)	- 1(1)
	25%	0.932(13)	17(1)	2496(1)	4436(3)	33(1)	9(1)	93(4)	10(1)	1(1)	- 1(1)

*RE ≡ random error added to data prior to least-squares refinement; i.e. $F'^2_{obs_i} = F^2_{obs_i}(1 + RE\ d_i)$ where d_i were drawn from a random sample of a normal distribution with mean zero and standard deviation 1.

parameters varied) refined to within three calculated standard deviations* of the same value in the three cases. The differences in the parameters in the two cases RE = 0.0 and RE = 0.25 are normally distributed, as can be seen from the linear half-normal probability plot (Abrahams and Keve, 1971) in Figure 11 of the 210 experimental δp. The experimental δp_i are:

$$\delta p_i = \| p(1)_i | - | p(2)_i \| / (\sigma^2(1)_i + \sigma^2(2)_i)^{\frac{1}{2}} \qquad (51)$$

where $p(1)_i$ and $p(2)_i$ are the i^{th} parameter of data set one and two respectively, and $\sigma^2(1)_i$ and $\sigma^2(2)_i$ are the variances of the i^{th} parameter obtained with data sets one and two. The expected δp_i values are those for a normal distribution. The quasi-linear behavior of δp implies that the δp have a random normal distribution and, furthermore, that the $p(1)_i$ and $p(2)_i$ are from the same population. As the random error contributions were increased the standard errors obtained from the least-squares refinements also increased. Figure 12 illustrates the behavior of the mean thermal and positional standard deviations as the random error is increased. The mean values were obtained by averaging over the 72 independent thermal parameters and over the 36 independent position parameters of the oxygens of synthetic chlorapatite. Although the differences in the parameters are small (with the exception of several site occupancy factors) and normally distributed, the

---

* Based on the standard deviations in the added-error case.

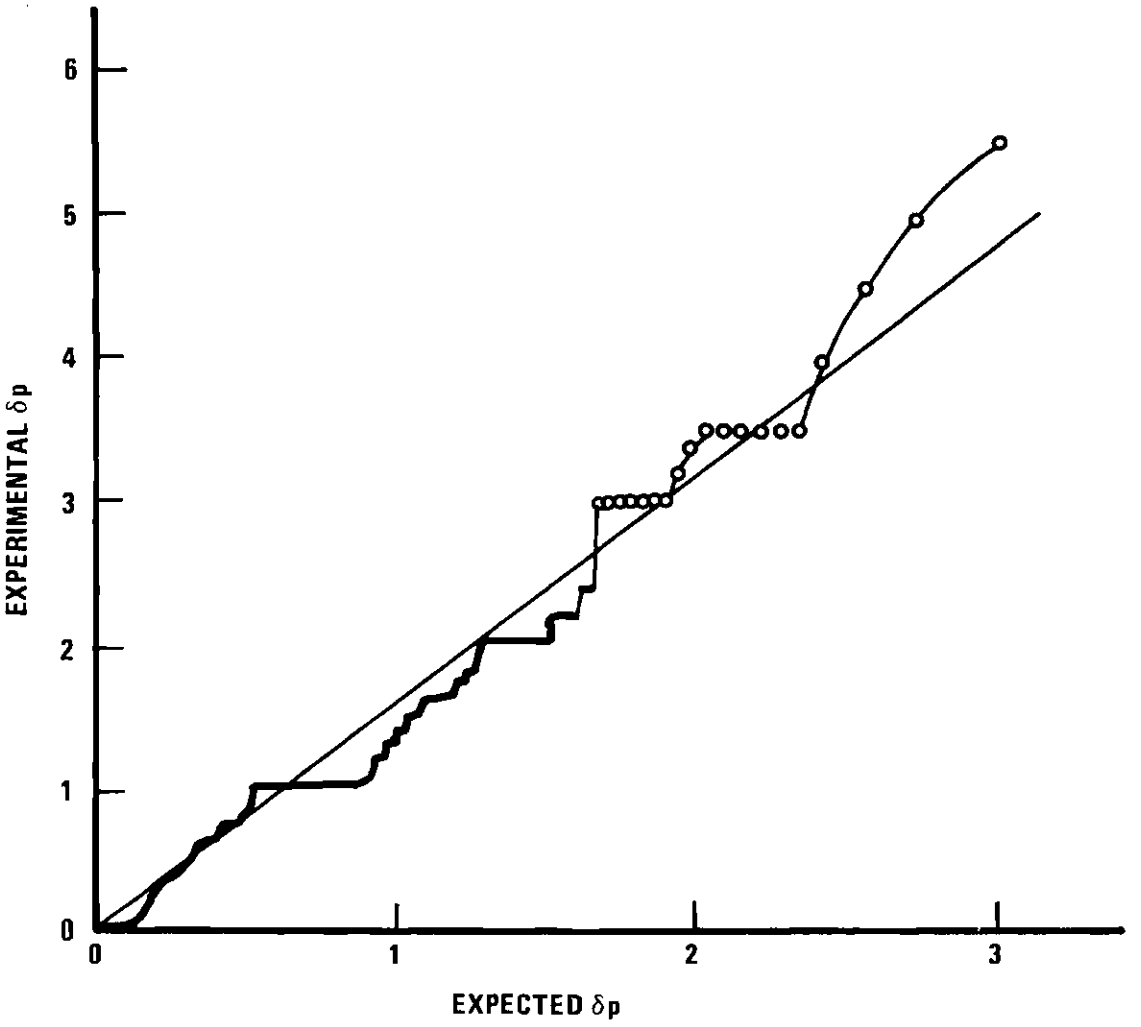

Figure 11. Half-Normal Probability Plot of Parameter Differences Obtained With RE=0% and RE=25% Data.

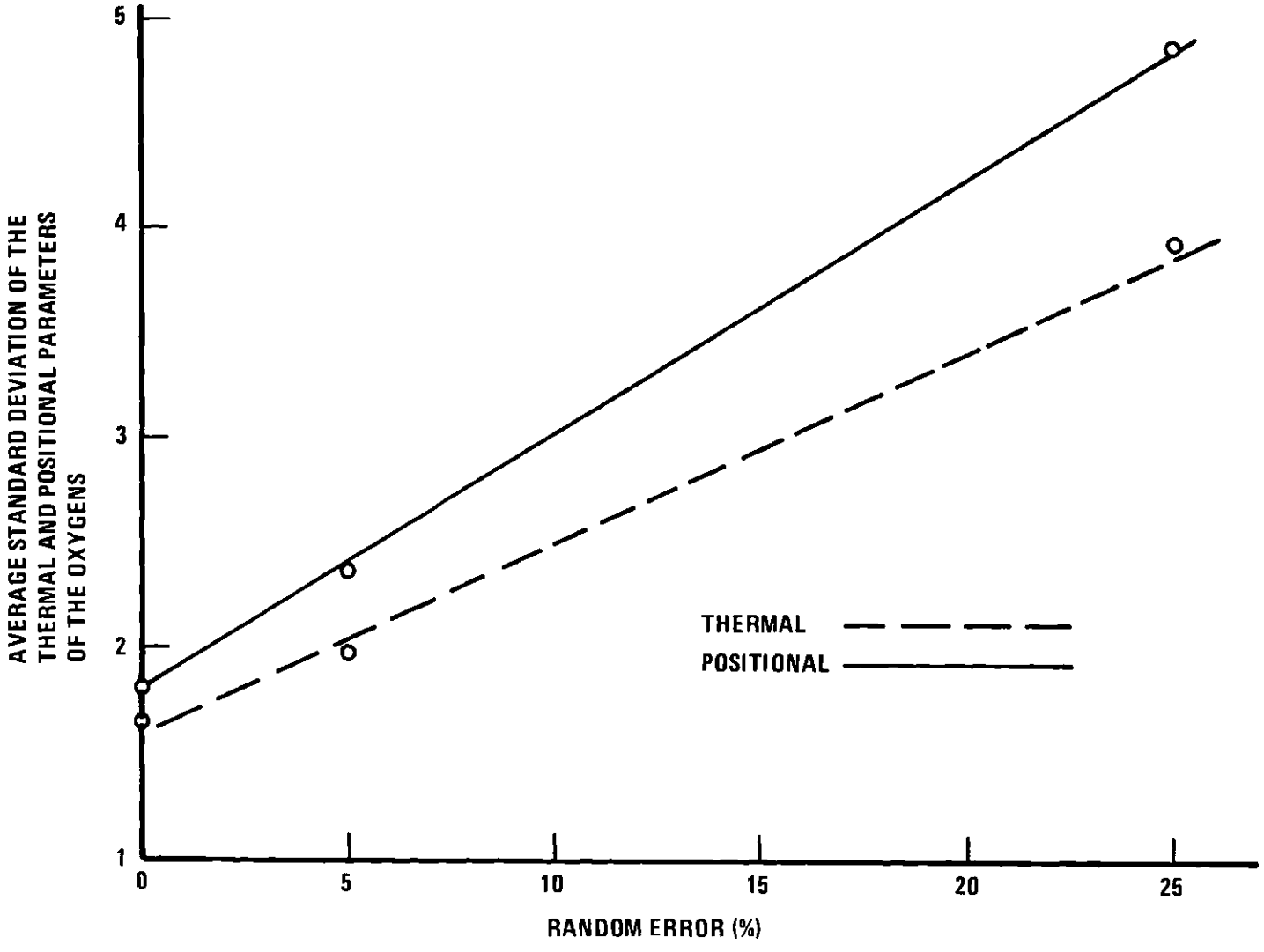

Figure 12. Variation of Average Standard Deviation of Chlorapatite Oxygens vs Random Error.

precision which one can assign to the refined parameters through the usual standard deviations is decreased, as would be expected, by the introduction of random artifical errors. The standard deviations in the RE = 0.25 case are at least 100 per cent greater than the standard deviations in the RE = 0.0 case. Although the differences in the parameters for the RE = 0.0 and RE = 0.25 cases are small, the slope of the line in Figure 11 indicates that (i) the differences are significantly greater than would be expected for the standard deviations obtained by the least-squares procedure or (ii) the least-squares estimated variances of the parameters are too small or (iii) both conditions may be applicable. The δp_i can be too large only if there is present in the data a systematic error such as to cause most of the $p(1)_i$ values to differ from the true values in a direction opposite from that in which the $p(2)_i$ differ. A systematic error would be revealed as a non-linear plot in Figure 11. The linear appearance of Figure 11 implies that such a systematic error does not exist in the data (or in this particular case, the same systematic error is present in both sets of data; the only difference in the two sets of data is the addition of a normally distributed random error). Thus, by analysis similar to Abrahams and Keve (1971), one can infer that each $\sigma(p_i)$ is 30 to 40 per cent too small.

Data Acquisition Rate and "Typical vs "Controlled-Precision" Scanning Techniques

Differences in the refined structure parameters produced by attributable differences between the "typical" and "controlled-precision"

reflection scanning techniques were directly assessed. Intensity data for reflections in the same range of $\sin\theta/\lambda$ were collected from a fluorapatite crystal with both techniques. The "typical" technique allocates approximately the same time to each reflection and, in this case, fixed the ratio of the time-on-peak to time-on-background at ~ 3.5 (variations of $\pm$ 23 per cent in this ratio occurred due to the increased angular width of the peak scan, with increasing 2θ, to account for spectral dispersion). The "controlled-precision" technique is that permitted by the algorithms developed for the computer-controlled diffractometer and described in Appendix C. (In that technique longer times are devoted to weaker reflections and the ratio of time-on-peak to time-on-background is adjusted in accord with the signal-to-noise ratio). An important difference is the total time devoted to the overall experiment; the acquisition rates were approximately 30 and 4 reflections per hour for the "typical" and "controlled-precision" techniques, respectively. Figure 13 shows the half-normal probability plot of the differences in the parameters obtained by least-squares analysis of the data acquired by the two methods. The differences appear to be distributed normally, but with standard deviations larger than those standard deviations obtained from the least-squares refinement. The fluorapatite specimen used was Syn FAp 35-7 and the final refined parameters are presented in Table 5. The final agreement factors (wR_2) for the refinements on the "typical" and "precision" data were 7.7 per cent and 2.8 per cent respectively. Standard errors, obtained by least-squares, are enclosed in parenthesis after each independent variable. Dependent variables are presented as decimals without

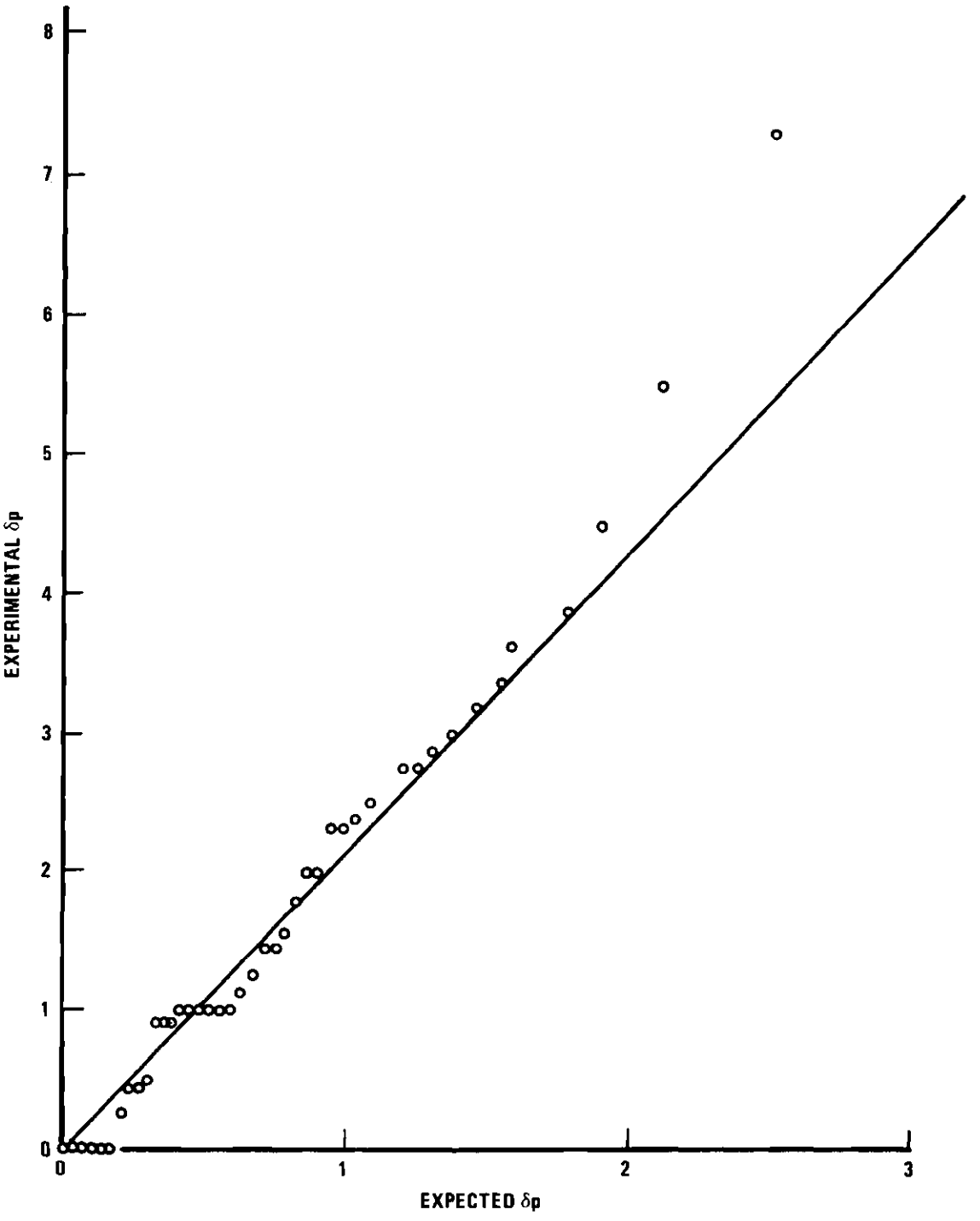

Figure 13. Half-Normal Probability Plot of Parameter Differences Obtained With "Typical" and "Controlled-Precision" Techniques Applied to Specimen FAp 35-7.

Table 5. Refined Structure Parameter of Fluorapatite (35-7)
Data Collected by "Typical" and "Precision" Methods

ATOM	TECHNIQUE	SITE OCCUPANCY FACTOR	X	Y	Z
O_I	PREC.	0.500(3)	0.3262(1)	0.4843(1)	1/4
	TYP.	0.496(2)	0.3261(2)	0.4850(2)	1/4
O_{II}	PREC.	0.506(3)	0.5880(1)	0.4668(1)	1/4
	TYP.	0.494(2)	0.5885(2)	0.4666(2)	1/4
O_{III}	PREC.	0.999(4)	0.3416(1)	0.2568(1)	0.0704(1)
	TYP.	1.006(3)	0.3411(2)	0.2564(1)	0.0708(2)
Ca_{II}	PREC.	0.488(1)	0.2416(0)	-0.0071(0)	1/4
	TYP.	0.481(1)	0.2414(1)	-0.0072(1)	1/4
Ca_I	PREC.	0.325(1)	1/3	2/3	0.0011(0)
	TYP.	0.326(1)	1/3	2/3	0.0011(1)
P	PREC.	0.497(1)	0.3981(0)	0.3688(0)	1/4
	TYP.	0.505(1)	0.3980(1)	0.3688(1)	1/4
F	PREC.	0.157(1)	0	0	1/4
	TYP.	0.156(1)	0	0	1/4

(Continued on next page)

Table 5. Refined Structure Parameter of Fluorapatite (35-7) Data Collected by "Typical" and "Precision" Methods (Continued)

ATOM	TECHNIQUE	β_{11}	β_{22}	β_{33}	β_{12}	β_{13}	β_{23}
O_I	PREC.	0.0035(1)	0.0026(0)	0.0041(1)	0.0023(0)	0	0
	TYP.	0.0035(2)	0.0027(2)	0.0039(2)	0.0023(2)	0	0
O_{II}	PREC.	0.0016(0)	0.0024(1)	0.0070(1)	0.0007(0)	0	0
	TYP.	0.0011(1)	0.0023(2)	0.0066(3)	0.0004(1)	0	0
O_{III}	PREC.	0.0061(1)	0.0031(0)	0.0031(1)	0.0029(0)	-0.0021(0)	-0.0014(0)
	TYP.	0.0067(2)	0.0034(1)	0.0029(2)	0.0033(1)	-0.0021(1)	-0.0013(1)
Ca_{II}	PREC.	0.0022(0)	0.0020(0)	0.0027(0)	0.0011(0)	0	0
	TYP.	0.0021(0)	0.0019(0)	0.0026(0)	0.0010(0)	0	0
Ca_I	PREC.	0.0030(0)	0.0030	0.0020(0)	0.0015	0	0
	TYP.	0.0031(0)	0.0031	0.0021(1)	0.0016	0	0
P	PREC.	0.0014(0)	0.0012(0)	0.0017(0)	0.0007(0)	0	0
	TYP.	0.0015(1)	0.0013(1)	0.0019(1)	0.0007(1)	0	0
F	PREC.	0.0025(1)	0.0025	0.0129(3)	0.0012	0	0
	TYP.	0.0030(2)	0.0030	0.0118(6)	0.0015	0	0

a standard error, while those parameters which have values fixed by symmetry are represented by zeroes or as fractions.

If the difference in the final agreement factors is attributed to differences in counting statistics, one should spend n times longer on the entire experiment with the "typical" technique to obtain the same agreement factor as one obtains with the "precision-scanning" technique, where

$$n = \left(\frac{7.7}{2.8}\right)^2 \approx 7.5 \quad . \tag{52}$$

(In equation (52) the square of the agreement factor wR_2 has been assumed proportional to the total time for the experiment). This implies that 25 per cent more time (in this case) will be required to obtain the same wR_2 with the "typical" techniques than with the "controlled-precision" techniques. The requirement of extra time to acquire the same precision may arise from two sources: (i) additional time will be required to obtain the same precision since the optimum ratio of time spent-on-peak to time spent-on-background is not used with the "typical" technique (see Appendixes B and C), and (ii) with the "typical" technique the data for a substantial number of reflections may be collected under conditions of simultaneous diffraction (the principal effect of inclusion of simultaneous diffraction effects is the increase in the agreement factor; see the section on simultaneous diffraction, this chapter).

The conclusion one can draw from the above is that for an allotted total time T for an experiment one will be able to detect smaller

differences which are physically significant with the "controlled-precision" technique than with the "typical" technique.

Simultaneous Diffraction

Effectiveness and Reliability of "Flag-Test"

Simultaneous diffraction can result in very significant changes in the integrated Bragg intensities (see Chapter III). Our procedure for detecting simultaneous diffraction effects was to collect the data for each reflection at two angular settings of the diffraction vector and to reject ("flag") those reflections for which the two net integrated intensities differed by more than 3σ (σ is the standard deviation from counting statistics of one of the integrated intensity measures). The effectiveness and reliability of this "flagging" was assessed directly. The same set of data (approximately 400 reflections) was collected twice under identical conditions. The specimen Syn FAp 35-7 was used and an asymmetrical setting of the crystal was utilized (the angle between ϕ and c* was 15°). During the two runs, 31 and 29 per cent of the reflections, respectively, were flagged as possibly suffering from simultaneous diffraction. Sixty-two per cent of those reflections which were flagged were flagged in both runs. Thus, in this case, approximately one-fifth of the data, and possibly another 10 per cent, appears to be collected under conditions of simultaneous diffraction. This frequency of occurrence, of implied simultaneous diffraction, is disquietingly large. Additional studies were undertaken to assess the frequency of occurrence vs the setting asymmetry of the specimen and the specimen size.

Frequency of Occurrence vs Setting Asymmetry and Specimen Size

As discussed by Burbank (1965), the frequency of occurrence of intrinsic simultaneous diffraction (that arising as a consequence of the intrinsic symmetry of the crystal under investigation) may be reduced if the data are collected with the crystal specimen in an asymmetric setting. However, the frequency with which detectable simultaneous diffraction events occur was found still to be significantly large even with asymmetrical settings. Table 6 presents the results for six different specimens of various values of angular missetting of the nearest symmetry axis of the crystal from the ϕ axis of the goniostat. There was an effective one degree rotation about the diffraction vector between the two settings. Since a reflection was flagged, implying occurrence of simultaneous diffraction, if the two intensity measures differed by more than three standard deviations, one would expect only 0.36 per cent of the intensities to differ by more than three standard deviations on the basis of counting statistics. As can be seen from Table 6, the frequency of flagged reflections far exceeds that expected from counting statistics. Shape asymmetry of the specimen could contribute to intensity variations as one rotates about the diffraction vector, but it is improbable that this significantly increased the flag frequency, for the x-ray paths through the specimens changed by only one degree. Blunders, such as misreadings of the scalar or physical obstructions in the x-ray beam, could also have resulted in an increased expected flag-rate. However, on several occassions the same sets of data were collected twice without rotation about $\vec{S}$. That experience showed that the rate at which blunders occur is certainly far less than

Table 6. Percentages of Reflections Flagged for Each Specimen

Specimen	Angle Between	$\Delta\psi$	Number of Reflections	Reflections Flagged (%)	μR
G-6-6-1	ϕ & (0,0,1) 1.0°	1°	1512	31.5	0.96
G-6-6-3	ϕ & (0,0,1) 1.9°	1°	2180	31.7	1.08
NdF_3-FAp #2	ϕ & (0,0,1) 2.4°	1°	1472	34.0	1.01
Nd_2O_3-FAp #1	ϕ & (0,0,1) 1.9°	1°	1484	28.1	0.79
G-10-1	ϕ & (0,0,1) 1.9°	1°	1508	14.1	0.50
Syn FA 35-7	ϕ & (1,1,0) 7.0°	1°	1375	17.5	0.52

one per cent and cannot account for the 14 to 34 per cent rate at which reflections were observed to be flagged.

In order further to assess the effectiveness of missetting the crystal from a symmetry axis to reduce the occurrence of simultaneous diffraction, the crystal, fluorapatite 35-7, was repeatedly further misset and the intensities of the reflections which were flagged in the previous data collection were remeasured (see Table 7). On the third repetition of this procedure the c* direction had been misset by 20.9 degrees from the ϕ axis and only 0.59 x 0.475 x 0.315 per cent, or eight per cent of the initial 1512 reflections were flagged.

Figure 14 shows that the relationship between the frequency of occurrence of flagged reflections and the μR for the specimen is approximately linear. This conclusion agrees with that of Åsbrink (1970), who has shown theoretically and observed experimentally that with decreasing crystal size, the intensity of a reflection affected by simultaneous diffraction decreases faster than that of a non-affected reflection.

Extinction, a closely related phenomenon, would also be expected to decrease with crystal volume and to vanish at the limit of infinitesimal volumes.

Effect of Simultaneous Diffraction on the Extinction Constant c

Åsbrink (1970) points out that the principal effect of the simultaneous diffraction errors in least-squares structure refinements is to increase the apparent extinction correction. It might have been possible to foresee this result intuitively since the physical effect of both simultaneous diffraction and extinction is to compress the

Table 7. Number of Reflections Flagged for Various Settings of the Specimen Fluorapatite 35-7.

Angular Misseting Between ϕ & c* (degrees)	Number of Reflections Collected	Percentage Flagged (%)
1.0	1512	31.5
9.1	469	47.5
20.9	212	59.0

Table 8. Values of the Extinction Constant, $\underline{c}$, Obtained for the Various Apatite Specimens.

Specimen	$\underline{c}$ ($\times 10^{-5}$)
G-6-6-1*	4.2
G-6-6-1	1.9
G-6-6-3	1.0
NdF_3FAp	2.5
NdO_3FAp	1.9
G-10-1	1.3
Syn FAp 35-7	1.6

*Flagged reflections included in the extinction correction for this entry.

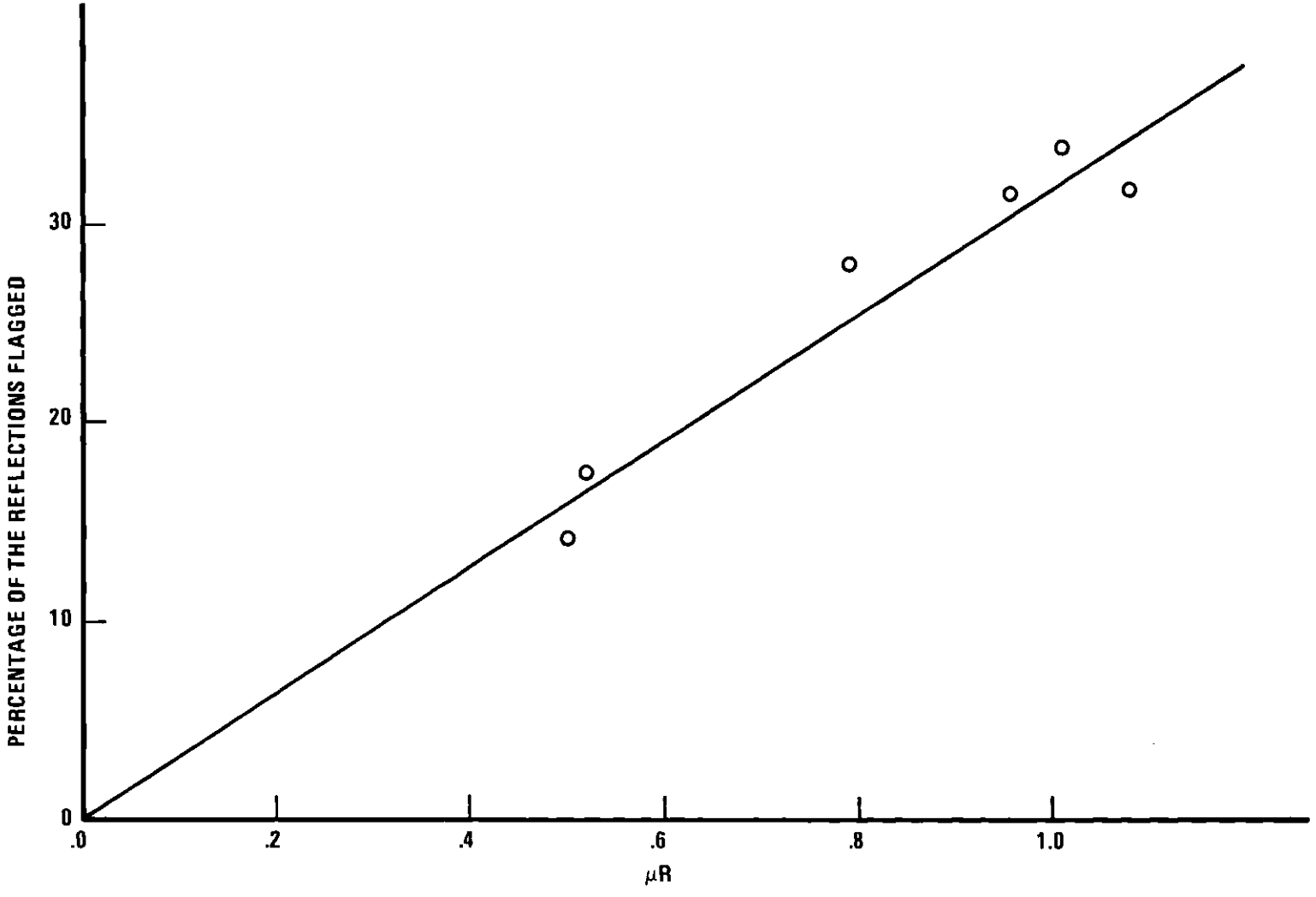

Figure 14. Percentage of Flagged Reflections vs μR.

range of the observed intensities. A least-squares extinction correction (see equation (30) of Chapter III and the following section here) was made for the data obtained from specimen G-6-6-1, both with and without those reflections which had been flagged, during data collection, as possibly suffering from simultaneous diffraction effects. The values of the extinction constant, c, were 4.2×10^{-5} and 1.9×10^{-5} for the data sets which, respectively, included and did not include the flagged reflections. The c values obtained for the various specimens examined are listed in Table 8. The c value obtained for the data set which included the flagged reflections is significantly larger than the c value obtained from the data set without the flagged reflections. The difference between these two extinction constants is approximately twice as great as the variation observed among the various apatites examined in this work. Thus, it is concluded that differences in the extinction constants can only be of physical significance if the effects of simultaneous diffraction are properly taken into account or if those reflections with large simultaneous diffraction effects are removed from the extinction correction procedure.

Effect of Simultaneous Diffraction on the Structure Parameters and Their Standard Deviations

To assess the effect of simultaneous diffraction on the least-squares structure parameters and their associated standard deviations, the data which were collected from specimen G-6-6-1 (a fluor-chlorapatite) were used in least-squares refinements with and without the data which had been flagged.

Because the parameters of the fluorine and chlorine atoms in

fluor-chlorapatite are highly correlated, these parameters were held fixed during refinements, at the best previously determined values, for the purpose of this test. For this reason the parameters of the fluorine and chlorine atoms are not included in Table 9. The values at which the parameters of fluorine and chlorine were held fixed are those in Table 16.

While the extinction correction constant was significantly changed by simultaneous diffraction, the other parameters were not (see Table 9). All of the final parameters except two agreed within one standard deviation and all agreed within three standard deviations. The average standard deviation for the parameters obtained with the data containing simultaneous diffraction effects was about 40 per cent greater than the average standard deviation obtained with the data which was relatively free from simultaneous diffraction. Furthermore, wR_2 increased from 4.35 to 6.04 per cent with the inclusion of the data affected by simultaneous diffraction.

Extinction and Anomalous Dispersion Corrections

The procedures used in this work for correcting for secondary extinction and anomalous dispersion are those described and evaluated by Sudarsanan and Young (1969). Sudarsanan and Young (1969) found that even seemly minor extinction corrections, on several specimens of Holly Springs hydroxyapatite, improved the mutual agreement between the parameters obtained from the refinement of data collected from three different specimens of the same origin. Prior to application of the extinction correction some of the thermal parameters differed by more

Table 9. Comparison of Least-Squares Parameters for G-6-6-1 (Fluor-Chlorapatite) Using Data With and Without Flagged Reflections.

ATOM	PARAMETERS	PARAMETER VALUE: WITHOUT FLAGGED REFLECTIONS	PARAMETER VALUE: WITH FLAGGED REFLECTIONS
O_I	x	0.3416(1)	0.3418(2)
	y	0.4912(1)	0.4912(1)
	z	1/4	1/4
	β_{11}	0.0056(1)	0.0054(2)
	β_{22}	0.0038(1)	0.0038(1)
	β_{33}	0.0046(1)	0.0046(2)
	β_{12}	0.0039(1)	0.0039(1)
	β_{13}	0	0
	β_{23}	0	0
O_{II}	x	0.5920(1)	0.5921(1)
	y	0.4650(1)	0.4650(1)
	z	1/4	1/4
	β_{11}	0.0020(1)	0.0021(1)
	β_{22}	0.0027(1)	0.0028(1)
	β_{33}	0.0092(2)	0.0094(2)
	β_{12}	0.0009(1)	0.0009(1)
	β_{13}	0	0
	β_{23}	0	0
O_{III}	x	0.3532(1)	0.3531(2)
	y	0.2661(1)	0.2659(1)
	z	0.0670(1)	0.0671(1)
	β_{11}	0.0098(1)	0.0096(2)
	β_{22}	0.0051(1)	0.0050(1)
	β_{33}	0.0065(1)	0.0063(2)
	β_{12}	0.0054(1)	0.0053(1)
	β_{13}	-0.0056(1)	-0.0053(1)
	β_{23}	-0.0037(1)	-0.0036(1)

(Continued on next page)

Table 9. Comparison of Least-Squares Parameters for G-6-6-1 (Fluor-Chlorapatite) Using Data With and Without Flagged Reflections (Continued)

ATOM	PARAMETERS	PARAMETER VALUE: WITHOUT FLAGGED REFLECTIONS	PARAMETER VALUE: WITH FLAGGED REFLECTIONS
P	x	0.4064(0)	0.4063(0)
	y	0.3741(0)	0.3741(0)
	z	1/4	1/4
	β_{11}	0.0021(0)	0.0021(0)
	β_{22}	0.0018(0)	0.0018(0)
	β_{33}	0.0024(0)	0.0025(1)
	β_{12}	0.0012(0)	0.0012(0)
	β_{13}	0	0
	β_{23}	0	0
Ca_I	x	1/3	1/3
	y	2/3	2/3
	z	0.0032(0)	0.0033(0)
	β_{11}	0.0034(0)	0.0034(1)
	β_{22}	0.0034	0.0034
	β_{33}	0.0021(0)	0.0021(1)
	β_{12}	0.0017	0.0017
	β_{13}	0	0
	β_{23}	0	0
Ca_{II}	x	0.2594(0)	0.2594(0)
	y	0.0027(0)	0.0027(0)
	z	1/4	1/4
	β_{11}	0.0030(0)	0.0030(0)
	β_{22}	0.0033(0)	0.0033(0)
	β_{33}	0.0029(0)	0.0030(0)
	β_{12}	0.0014(0)	0.0014(0)
	β_{13}	0	0
	β_{23}	0	0

than four standard deviations. In their worst case, application of the extinction correction changed the value of R_2 from 5.4 to 3.5 per cent. Iterative application of the seemingly minor extinction correction eventually resulted in excellent agreement (within one standard deviation) between the separate measures of all the final parameters, even anisotropic thermal parameters. For their final results (Sudarsanan and Young, 1969) a standard deviation was typically less than five per cent even for thermal parameters. Thus, the application of the extinction correction resulted in a significant improvement in the precision of the final parameters. Physical significance may be attributed to differences in parameters which exceed this demonstrated precision.

The addition of the real and imaginary terms of the anomalous dispersion to the atomic form factors of Ca and P ($f' = 0.24$, $f'' = 0.36$ for Ca; $f' = 0.11$, $f'' = 0.12$ for P) did not result in any significant changes in the refined parameters (Sudarsanan and Young, 1969). One-third of the parameters were changed by less than one part in ten thousand and none were changed by as much as one standard deviation with the introduction of the anomalous dispersion corrections. The wR_2 values found by Sudarsanan and Young (1969) were not changed by the incorporation of the additional anomalous dispersion terms.

In Table 10, the agreement factors (wR_2) obtained before and after the extinction correction was made are presented along with the maximum extinction correction observed (expressed as a percentage) and the extinction constant $\underline{c}$ for six of the apatite specimens used. In every case, the extinction correction significantly improved the agreement factor.

Table 10. Agreement Factors and Extinction Constants of the Various Apatites Observed.

SPECIMEN	wR_2 (%) BEFORE EXTINCTION CORRECTION	wR_2 (%) AFTER EXTINCTION CORRECTION	EXTINCTION CONSTANT ($x10^{-5}$)	MAXIMUM EXTINCTION CORRECTION (%)
G-6-6-1	10.15	4.35	1.9	15.3
G-6-6-3	6.07	5.90	1.0	5.9
NdF_3-FAp	5.41	2.92	2.5	5.9
NdO_3-FAp	8.00	2.81	1.9	8.4
G-10-1	7.31	4.34	1.3	10.7
Syn FAp 35-7	6.39	2.84	1.6	13.2

Physical Reality of Specimen-To-Specimen Differences

Although the two samples G-6-6-1 and G-6-6-3 were both obtained from the same fragment of fluor-chlorapatite, they exhibited the greatest extremes in the extinction correction. The differences in the positional parameters were all less than three standard deviations ($\sigma \approx 0.0001$), while the differences in the anisotropic thermal parameters exceeded three standard deviations for six parameters (as high as 14σ for β_{33} of Ca_{II}). The independent variables for the two types of halogen atoms, both located on the screw-axis of the apatite structure, could not all be varied simultaneously because of high correlations between their parameters. These parameters were refined by an iterative step-wise procedure, whereby only one parameter out of each set of highly correlated parameters was varied while the remainder were held fixed. On alternate cycles of refinement, the set of parameters held constant during the previous cycle are allowed to vary while those previously allowed to vary are now held constant. This process is repeated as many times as needed to overcome (indicated by progressively smaller changes in the parameter values) the high correlations of the parameters.

Many descriptions of the apatite structure can be found in published literature. Beevers and McIntyre (1946) have illustrated the apatite structure with color overlays. The content of an hexagonal fluorapatite or hydroxyapatite unit cell can be described in four parts: (1) Ca_I atoms at $z \approx 0$ and $z \approx \frac{1}{2}$ forming columns parallel to $\underline{c}$ at $x = 1/3$, $y = 2/3$ and at $x = 2/3$, $y = 1/3$; (2) a column of F or OH ions on the screw-axis parallel to $\underline{c}$ at $x = 0$, $y = 0$; (3) two triangular arrays

of Ca_{II} atoms on the mirror planes at z = 1/4 and z = 3/4 and centered on the screw axis coinciding with the F or OH columns; and (4) six phosphate tetrahedra on the mirror planes. The F ion occurs at (0, 0, 1/4) and (0, 0, 3/4) at the centers of the Ca_{II} triangles whereas OH is in two-fold disorder, about the mirror planes, at 0, 0, 1/4-Δ and 0, 0, 1/4+Δ ($\Delta \approx 0.19$ for H and 0.05 for O, Sudarsanan and Young, 1969). A description of the chlorapatite structure is in Chapter VII.

Fourier-difference maps were prepared (see "Synthetic Fluor-Chlorapatite," Chapter VII), and used in determining the site-occupancy factors of F_I and F_{II}. F_I is the designation given the fluorine atom which is located on the mirror at z = 1/4 and F_{II} the designation of the off-mirror-plane fluorine atom at $z \approx 0.16$. A comparison of the refined parameters of G-6-6-1 and G-6-6-3 is made in Table 11. The large differences in the anisotropic thermal parameters are greater than what one would expect, for these data collection and analysis techniques (Sudarsanan and Young, 1969), if the two specimens were really the same. Electron microprobe analysis of the G-6 material, with a 10 micron spot size, indicated a compositional variation from point-to-point on the sample (Johnson, 1971). Thus, the observed differences in the parameters may have a structural origin and, hence, physical significance.

The agreement factors (R_1) were 2.17 and 3.22 per cent for G-6-6-1 and G-6-6-3, respectively, while the average value of R_1 obtained for the seven specimens used in this study was 2.14 per cent. A difference Fourier-map was prepared of the asymmetric unit of G-6-6-1 which did not reveal any peaks significantly greater than the ambient "noise" level of the map. Thus the refined structure can be assumed to

Table 11. Comparison of Refined Parameters of Two Fluor-Chlorapatite Specimens (G-6-6-1 and G-6-6-3).

ATOM	SPECIMEN	MULT	X	Y	Z
O_I	6-1	0.5224(39)	0.3416(1)	0.4912(1)	1/4
	6-3	0.5298(51)	0.3411(2)	0.4908(2)	1/4
O_{II}	6-1	0.5269(44)	0.5920(1)	0.4650(1)	1/4
	6-3	0.5353(54)	0.5918(1)	0.4651(1)	1/4
O_{III}	6-1	1.0849(59)	0.3532(1)	0.2661(1)	0.0670(1)
	6-3	1.0715(95)	0.3534(2)	0.2660(1)	0.0674(1)
P	6-1	0.5473(14)	0.4064(0)	0.3741(0)	1/4
	6-3	0.5489(17)	0.4064(0)	0.3741(0)	1/4
Ca_I	6-1	0.3513 (8)	1/3	2/3	0.0032(0)
	6-3	0.3510(10)	1/3	2/3	0.0032(0)
Ca_{II}	6-1	0.5220(11)	0.2594(0)	0.0027(0)	1/4
	6-3	0.5252(12)	0.2594(0)	0.0028(0)	1/4
F_I	6-1	0.0081(11)	0	0	1/4
	6-3	0.0067(18)	0	0	1/4
F_{II}	6-1	0.0194(16)	0	0	0.1593(40)
	6-3	0.0223(33)	0	0	0.1566(40)
Cl	6-1	0.1488(14)	0	0	0.4430(2)
	6-3	0.1539(22)	0	0	0.4433(3)

(Continued on next page)

Table 11. Comparison of Refined Parameters of Two Fluor-Chlorapatite Specimens (G-6-6-1 and G-6-6-3). (Continued)

ATOM	SPECIMEN	β_{11}	β_{22}	β_{33}	β_{12}	β_{13}	β_{23}
O_I	6-1	0.0056(1)	0.0038(1)	0.0046(1)	0.0039(1)	0	0
	6-3	0.0053(1)	0.0037(1)	0.0053(2)	0.0037(1)	0	0
O_{II}	6-1	0.0020(1)	0.0027(1)	0.0092(2)	0.0009(1)	0	0
	6-3	0.0020(1)	0.0028(1)	0.0096(2)	0.0009(1)	0	0
O_{III}	6-1	0.0098(1)	0.0051(1)	0.0065(1)	0.0054(1)	-0.0056(1)	-0.0037(1)
	6-3	0.0095(2)	0.0047(1)	0.0047(1)	0.0068(2)	-0.0055(1)	-0.0035(1)
P	6-1	0.0021(0)	0.0018(0)	0.0024(0)	0.0012(0)	0	0
	6-3	0.0019(0)	0.0016(0)	0.0028(0)	0.0011(0)	0	0
Ca_I	6-1	0.0034(0)	0.0034	0.0021(0)	0.0017	0	0
	6-3	0.0033(0)	0.0033	0.0026(0)	0.0017	0	0
Ca_{II}	6-1	0.0030(0)	0.0033(0)	0.0029(0)	0.0014(0)	0	0
	6-3	0.0028(0)	0.0032(0)	0.0035(0)	0.0013(0)	0	0
F_I	6-1	0.0028(22)	0.0028	0.0086(38)	0.0014	0	0
	6-3	0.0028(28)	0.0028	0.0086(74)	0.0014	0	0
F_{II}	6-1	0.0040(21)	0.0040	0.0091(30)	0.0020	0	0
	6-3	0.0052(20)	0.0052	0.0091(38)	0.0026		
Cl	6-1	0.0034(1)	0.0034	0.0199(4)	0.0017	0	0
	6-3	0.0036(1)	0.0036	0.0192(4)	0.0018	0	0

be essentially correct. The residual R factor, at the conclusion of the least-squares refinements, has contributions from error sources of both a systematic and random nature. The random errors arise from both counting statistics and the reproducibility of the instrumentation. With one per cent as the nominal standard error, Sudarsanan and Young (1969) have shown that the most probable value of R_2 due to counting statistics for hydroxyapatite specimens is from one to two per cent. The reproducibility of the computer-controlled diffractometer was shown to yield a mutual R factor (R_2) of 0.67 per cent.

CHAPTER VII

MATERIAL RESULTS

Introduction

The experimental techniques and the analytical approach discussed in previous chapters were used to collect single-crystal Bragg-intensity data and to refine the structures of several variant forms of the common mineral apatite. The intensity data have been deposited with the School of Physics, Georgia Institute of Technology.

Apatites were chosen for the following reasons:

(1) The basic structures of the more common forms of apatite are well known and thus provide a good starting point for refinement of the interesting structural details without distraction from the phase problem (i.e., the initial phase determination can be avoided).

(2) Single crystals of apatite can be readily grown with various controlled compositions.

(3) A wide variety of substitutions and vacancies occur readily in the apatite structure. A good test of the precision techniques will be to find the structural location and role of substituents occurring in relatively small amounts ($\leq$ 1 atomic weight per cent).

(4) The apatites are of biological importance; the model system for the major inorganic component of tooth and bone is hydroxyapatite.

(5) The fluor-chlorapatites are important in the lighting

industry as phosphor in fluorescent lamps and in agriculture for the production of fertilizers.

(6) Neodymium-containing fluorapatite is a possible laser material.

In order to facilitate the detection of differences in the apatite structure due to substitution of fluorine or neodymium, the structures of stoichiometric fluorapatite ($Ca_{10}(PO_4)_6F_2$) and chlorapatite ($Ca_{10}(PO_4)_6Cl_2$) were first refined extensively. In addition to these two stoichiometric apatites, data from two chlorapatites with different degrees of fluorine substitution were also collected as well as from two fluorapatites with, possibly, different forms of neodymium substitutions. The sources of neodymium were the NdF_3 or Nd_2O_3 in the melt composition from which the crystals were grown.

Comparison of Mineral and Synthetic Fluorapatite

The methods described in the previous chapters were used to collect integrated Bragg intensities from a spherically-shaped single crystal of flux-grown fluorapatite. After the flagged data had been eliminated, 1086 crystallographically unique reflections remained. Least-square refinements of the fluorapatite structure were then made. The final conventional R factor (R_1) was 1.6 per cent. The results are in essential agreement with the earlier works of Beevers and McIntyre (1946) and Young, Sudarsanan and Mackie (Chapter II of: Structural Properties of Hydroxapatite and Related Compounds, Brown and Young, Eds.). It is instructive to compare the results of Young, Sudarsanan and Mackie on the mineral sample of fluorapatite (origin: Auburn, Maine)

with the final refined parameters of the synthetic fluorapatite specimen (Table 12). The parameters show remarkable agreement for two specimens from such dissimilar origins. The excellent agreement must be considered somewhat fortuitous when one considers the size of the discrepancies observed between the two fluor-chlorapatites (G-6-6-1 and G-6-6-3 discussed in Chapter VI), both obtained from the same small chip of synthetic material.

Although the inter-specimen agreement is good for most of the parameters, five anisotropic thermal parameters exhibit significant and systematic differences. These parameters are β_{33} of O_I, O_{II}, and F; and β_{11} of O_{III} and F. In each of these cases, the thermal parameter obtained in the refinement of the mineral sample is larger than the corresponding parameter for the synthetic sample. One cannot distinquish, by least-squares techniques alone, between dynamic and static disorder. The least-squares structure-refinement program used in this work treats the static disorder as an apparent increase in the temperature factor of the atom which is dispersed statically. Thus, for those atoms in mineral fluorapatite with a thermal parameter larger than in synthetic fluorapatite, the increase may be due to either increased static or dynamic dispersal, perhaps both.

The data which were collected from the mineral specimen were not selected to be free from significant ($> 3\sigma$) simultaneous diffraction effects, while the data collected from the synthetic sample were. Thus the close agreement between the two sets of refined parameters is further evidence to support the conclusion, set forth in the previous chapter, that simultaneous diffraction will have little effect on the

Table 12. Least-Squares Structure Parameters of Mineral and Synthetic Fluorapatite.

ATOM	SPECIMEN	MULTIPLIER	X	Y	Z
O_I	Mineral	1/2	0.3266(1)	0.4848(1)	1/4
	Synthetic	0.500(3)	0.3262(1)	0.4843(1)	1/4
O_{II}	Mineral	1/2	0.5879(1)	0.4668(1)	1/4
	Synthetic	0.500(3)	0.5880(1)	0.4668(1)	1/4
O_{III}	Mineral	1	0.3415(1)	0.2571(1)	0.0702(1)
	Synthetic	0.998(4)	0.3416(1)	0.2568(1)	0.0704(1)
P	Mineral	1/2	0.3982(1)	0.3689(1)	1/4
	Synthetic	0.496(1)	0.3981(0)	0.3688(0)	1/4
Ca_I	Mineral	1/3	1/3	2/3	0.0012(1)
	Synthetic	0.325(1)	1/3	2/3	0.0011(0)
Ca_{II}	Mineral	1/2	0.2415(1)	-0.0071(1)	1/4
	Synthetic	0.488(1)	0.2416(0)	-0.0071(0)	1/4
F	Mineral	1/6	0	0	1/4
	Synthetic	0.157(2)	0	0	1/4

(Continued on next page)

Table 12. Least-Squares Structure Parameters of Mineral and Synthetic Fluorapatite (Continued)

ATOM	SPECIMEN	β_{11}	β_{22}	β_{33}	β_{12}	β_{13}	β_{23}
O_I	Mineral	0.0035(1)	0.0024(1)	0.0047(2)	0.0024(1)	0	0
	Synthetic	0.0035(1)	0.0026(0)	0.0041(1)	0.0023(0)	0	0
O_{II}	Mineral	0.0015(1)	0.0022(1)	0.0085(2)	0.0007(1)	0	0
	Synthetic	0.0016(0)	0.0024(1)	0.0070(1)	0.0007(0)	0	0
O_{III}	Mineral	0.0068(1)	0.0031(1)	0.0033(1)	0.0032(1)	-0.0024(1)	-0.0015(1)
	Synthetic	0.0061(1)	0.0031(0)	0.0031(1)	0.0029(0)	-0.0021(0)	-0.0014(0)
P	Mineral	0.0013(1)	0.0011(1)	0.0019(1)	0.0007(1)	0	0
	Synthetic	0.0014(0)	0.0012(0)	0.0017(0)	0.0007(0)	0	0
Ca_I	Mineral	0.0026(1)	0.0026	0.0018(1)	0.0013	0	0
	Synthetic	0.0030(0)	0.0030	0.0020(0)	0.0015	0	0
Ca_{II}	Mineral	0.0018(1)	0.0018(1)	0.0024(1)	0.0009(1)	0	0
	Synthetic	0.0020(0)	0.0020(0)	0.0027(0)	0.0011(0)	0	0
F	Mineral	0.0031(1)	0.0031	0.0144(4)	0.0015	0	0
	Synthetic	0.0025(1)	0.0025	0.0129(3)	0.0012	0	0

final values of the refined parameters if an extinction correction has been applied to the data. However, the R factors will in general be larger for the data set compromised by simultaneous diffraction. In this case, the R_1 for the mineral sample data was 2.9 per cent for 1185 reflections compared to 1.6 per cent for 1086 reflections from the synthetic sample. It must be held in mind, however, that the difference between the two final R_1 factors is most probably not due entirely to simultaneous diffraction for other differences in the data collection strategy existed also (in particular, the nominal statistical precision with which each reflection was collected was different in the two examples).

From Table 12 we see that the site-occupancy factors of Ca_I, Ca_{II} and F are significantly lower (based on the least-squares derived standard deviations) than the stoichiometric values of 1/3, 1/2 and 1/6. The most obvious explanation for departure from stoichiometry would be the loss of CaF_2 during the growth of the crystal. However, this simple model ($Ca_{10-x}(PO_4)_6F_{2(1-x)}$) is not adequate to account for the departures from stoichiometry indicated by the least-squares-refinement site-occupancy factors. The deficiency of divalent calcium in apatite structures has been considered by many authors (e.g., Posner and Perloff, 1957; Brown, 1971) and controversy still exists as to the mechanism by which it can occur. Theoretically the ratio Ca/P = 1.667 (10/6); however, the experimental ratio of Ca/P observed for this fluor-apatite (Syn FAp 35-7) was 1.640 ± 0.002. While this value of Ca/P is low, it is still above the lower limit of 1.33 observed for synthetic calcium deficient apatites (Posner and Perloff, 1957). Although the

mechanism of the Ca deficiency is not known at this time the results are nevertheless consistent with the fact that many of the synthetic calcium apatites have been found by least-squares structure-refinement to be calcium deficient (Sudarsanan, 1971).

Although charge balance was not introduced into the least-squares refinement as a constraint on the variation of the site-occupancy factors, the total ionic charges do nevertheless balance to within 0.4 of an electron per unit cell. The expected standard deviation in the charge balance (obtained as the square root of the sum of the variances of the individual site-occupancy factors) is 0.8 electrons. That is to say, through refinement of the site-occupancy factors the total number of electrons in the unit cell have been determined with a standard deviation equal to 0.2 per cent of the stoichiometric value.

Synthetic Chlorapatite

The investigation of the structure of synthetic chlorapatite proved to be interesting in itself as well as to provide an "ideal" chlorapatite structure model for reference in the later study of fluorine substituting for the chlorine. Most of this section, dealing with chlorapatite is based, in part or in whole, on the paper Monoclinic Structure of Synthetic $Ca_5(PO_4)_3Cl$, Chlorapatite (Mackie, Elliott, and Young, 1972). Most apatites have the hexagonal space group, $P6_3/m$. However, nearly stoichiometric chlorapatite ($Ca_{10}(PO_4)_6\ Cl_2$) exhibits the monoclinic space group $P2_1/b$ (Young and Elliott, 1966). A mineral chlorapatite with nearly stoichiometric chlorine content has been similarly reported to be monoclinic (Hounslow and Chao, 1970), as have

both mineral and synthetic mimetite, $Pb_{10}(AsO_4)_6Cl_2$ (Keppler, 1968 and 1969) and synthetic hydroxyapatite (Elliott, 1971). Stoichiometric chlorapatite has been observed to undergo a reversible phase transition at about 200°C. In the monoclinic form (the low-temperature form) the interaxial angles remain unchanged (within experimental error) from the hexagonal values and the b axis is twice that of the hexagonal b axis. Thus, one would expect the monoclinic structure of chlorapatite to have a pseudo-hexagonal character. Initial refinements in the hexagonal space group ($P6_3/m$) with anisotropic temperature factors, and with simulation of the monoclinic glide plane by two-fold disorder of the chlorine atoms about the mirror planes, yielded an R_2 of 5.5 per cent. These refinements in the hexagonal space group were based on 441 reflections from a 0.18 mm diameter spherical specimen and a structure model with 40 independent variables.

The final refinements of the chlorapatite structure were carried out in space group $P2_1/b$. They were based on 2232 reflections, of which 976 could occur only in the monoclinic space group, collected from a 0.31 mm diameter spherical specimen. The final refined parameters for synthetic monoclinic chlorapatite, as well as the parameters obtained in the hexagonal refinement transformed to the monoclinic cell for easy comparison with the monoclinic refinement, are presented in Table 13.

The precision structure refinement of chlorapatite provided atomic-scale details which could be related to the monoclinic-to-hexagonal phase transition as well as to the observed ferroelectric behavior (which occurs rather than the expected antiferroelectric

behavior) under the action of an applied electric field (Elliott and Young, 1968).

Pseudohexagonal Character and $P2_1/b$ and to $P6_3/m$ Transition

The pseudohexagonal character of specimen L1-24 (synthetic chlorapatite) can be easily seen from Table 13. Figure 15 is presented as an aid to visualizing the structure represented in Table 13. The figure is a plan view of the structure, the c axis normal to the drawing, with the height above the plane of the paper represented schematically by the numbers indicated for each atom. The figure also shows the relationship between the cell chosen for the $P2_1/b$ refinement and that of the conventional cell for apatite when refined in $P6_3/m$. The monoclinic cell is indicated by a solid outline and the hexagonal cell by the dashed outline. Not only is the b axis doubled for $P2_1/b$, but the origin of the $P2_1/b$ cell is shifted 1/4 of the monoclinic b axis along the b direction relative to the hexagonal cell. From this figure, the near hexagonal symmetry is also quite apparent.

The change in origin was necessitated by the very small (~ 0.8 Å) interatomic separation for the chlorine atoms if the change were not made.

The designation with a letter and Roman numeral subscript is identical with the atomic designation used in the literature for hexagonal apatites. In addition, primes and a lower-case letter subscript have been appended to the established designations to distinguish atoms which are not crystallographically equivalent in $P2_1/b$ but which were in $P6_3/m$. The subscripts "a", "b", and "c" differentiate between atoms in different asymmetric units which are not equivalent in $P2_1/b$ (because

Table 13. Final Refined Parameters of Synthetic Monoclinic Chlorapatite in $P2_1/b$ and $P6_3/m$.

Atom Parameters (1)	$P6_3/m$ (2)	$P2_1/b$ (3)		
ATOM	O_I	O_{Ia}	O_{Ib}	O_{Ic}
X	3436_5	3436_3 [3430_8]	4924_4 [4929_5]	1885_2 [1494_8]
Y	4928_5	4960_3 [4964_3]	3240_3 [3248_4]	5783_3 [5782_8]
Z	1/4	2563_4 [1/4]	7554_3 [3/4]	2480_3 [1/4]
β_{11}	457_{45}	533_{14} [457_{40}]	$980_{,}$ [1639_{40}]	163_{11} [134_{8}]
β_{22}	439_{40}	404_9 [405_{12}]	35_8 [34_3]	174_6 [214_{10}]
β_{33}	502_{53}	404_{23} [502_{51}]	400_{27} [502_{53}]	408_{19} [952_{63}]
β_{12}	371_{36}	184_6 [186_{28}]	3_4 [24_7]	70_5 [43_7]
β_{13}	0	-59_{20} [0]	$-8_{,4}$ [0]	-27_{17} [0]
β_{23}	0	-9_{18} [0]	$-7_{,3}$ [0]	-51_4 [0]
MULTIPLIER	1/2	1.017_{16} [1]	1.008_9 [1]	1.018_8 [1]
ATOM	O_{II}	O_{IIa}	O_{IIb}	O_{IIc}
X	5927_4	$5924_{,}$ [5927_4]	5342_4 [5343_4]	$1270_{,}$ [1270_4]
Y	4658_5	4827_3 [4829_3]	$3138_{,}$ [3135_5]	5467_3 [5466_4]
Z	1/4	2390_3 [1/4]	2447_3 [1/4]	7366_3 [3/4]
β_{11}	153_{28}	156_{31} [153_{28}]	247_{17} [242_{31}]	276_{12} [277_5]
β_{22}	242_{31}	67_6 [61_8]	$82_{,}$ [69_7]	32_6 [38_4]
β_{33}	773_{65}	581_{80} [773_{65}]	637_{25} [773_{65}]	370_{34} [773_{65}]
β_{12}	59_{26}	34_5 [30_{15}]	85_4 [92_3]	53_5 [67_7]
β_{13}	0	73_{16} [0]	-32_{19} [0]	52_{16} [0]
β_{23}	0	6_{11} [0]	-18_{13} [0]	44_{12} [0]
MULTIPLIER	1/2	0.993_8 [1]	1.012_5 [1]	0.997_{16} [1]
ATOM	O_{III}	O_{IIIa}	O_{IIIb}	O_{IIIc}
X	3542_4	3411_7 [3541_4]	7360_2 [7326_3]	820_3 [868_5]
Y	2677_5	$3804_{,}$ [3838_2]	2918_3 [2933_7]	4704_3 [4731_3]
Z	671_5	769_3 [670_4]	723_3 [670_5]	5774_3 [5670_5]
β_{11}	713_{33}	644_{27} [713_{57}]	337_{17} [393_{22}]	405_{17} [388_7]
β_{22}	393_{22}	102_8 [98_7]	83_8 [92_5]	147_8 [128_8]
β_{33}	530_{34}	429_{39} [$530_{,4}$]	$503_{,3}$ [530_{39}]	409_{34} [530_{39}]
β_{12}	358_{23}	154_8 [179_{13}]	29_5 [17_8]	168_8 [178_4]
β_{13}	-631_{18}	-329_{25} [-631_{36}]	199_{18} [310_{18}]	$+130_{17}$ [-101_7]
β_{23}	-310_{35}	-95_{13} [-355_{61}]	-41_{13} [-53_8]	-133_{13} [-206_{14}]
MULTIPLIER	1	1.014_{31} [1]	0.992_{13} [1]	0.991_{13} [1]
ATOM		$O_{III'a}$	$O_{III'b}$	$O_{III'c}$
X		3645_2 [3541_4]	$7300_{,}$ [7324_3]	894_3 [868_7]
Y		$3866_{,}$ [3838_2]	$2930_{,}$ [2933_2]	4327_3 [4271_3]
Z		6413_3 [6330_5]	6373_3 [6330_5]	9619_3 [9330_5]
β_{11}		431_{18} [713_{57}]	345_{17} [393_{22}]	280_{15} [388_7]
β_{22}		100_8 [98_7]	72_8 [92_5]	110_8 [128_8]
β_{33}		366_{32} [530_{39}]	412_{15} [530_{39}]	344_{26} [530_{39}]
β_{12}		123_7 [179_{13}]	30_7 [17_8]	88_7 [178_4]
β_{13}		147_{18} [631_{36}]	-134_{17} [-310_{35}]	24_{15} [101_8]
β_{23}		74_{13} [355_{61}]	40_{13} [53_8]	104_{12} [206_{13}]
MULTIPLIER		0.997_{15} [1]	0.972_{10} [1]	0.990_{17} [1]

Atom Parameters (1)	$P6_3/m$ (2)	$P2_1/b$ (3)		
ATOM	Ca_I	Ca_{Ia}	Ca_{Ib}	
X	1/3	3276_3 [1/3]	3387_3 [1/3]	
Y	2/3	5811_2 [7/12]	5836_0 [7/12]	
Z	38_2	34 [38_2]	$4986_{,}$ [4962_2]	
β_{11}	316_4	263_4 [316_6]	251_5 [316_6]	
β_{22}	316	70_5 [79_2]	70_3 [79_2]	
β_{33}	210_1	194_8 [210_{11}]	166_8 [210_{11}]	
β_{12}	158	61_2 [79_2]	69_2 [79_2]	
β_{13}	0	0_3 [0]	-2_3 [0]	
β_{23}	0	-6_2 [0]	-7_2 [0]	
MULTIPLIER	1/3	0.939_4 [1]	0.953_4 [1]	
ATOM	Ca_{II}	Ca_{IIa}	Ca_{IIb}	Ca_{IIc}
X	2598_1	2594_2 [2596_3]	53_2 [52_1]	$2559_{,}$ [2544_2]
Y	52_1	2523_3 [2526_6]	6229_4 [6228_4]	3398_5 [3398_5]
Z	1/4	2480_2 [1/4]	7481_2 [3/4]	7513 [3/4]
β_{11}	238_1	230_3 [239_8]	280_1 [272_8]	$273_{,}$ [272_7]
β_{22}	273_1	74_2 [68_2]	72_2 [68_2]	59_2 [69_2]
β_{33}	293_1	256_4 [293_{10}]	$267_{,}$ [$293_{,}$]	$256_{,}$ [293]
β_{12}	120_1	62_1 [60_4]	81_1 [77_3]	54_1 [60_4]
β_{13}	0	27_5 [0]	4_3 [0]	17_4 [0]
β_{23}	0	1_3 [0]	19_3 [0]	10_4 [0]
MULTIPLIER	1/2	0.962_4 [1]	0.965_2 [1]	0.962_4 [1]
ATOM	P	P_a	P_b	P_c
X	4078_1	$4076_{,}$ [4078_3]	6265_2 [6244_3]	$124_{,}$ [124]
Y	3754_1	4376_3 [4377_3]	2665_2 [2662_3]	4538_5 [4539_3]
Z	1/4	2533_3 [1/4]	$2522_{,}$ [1/4]	7517_3 [1/4]
β_{11}	163_3	182_4 [163_9]	163_4 [$159_{,6}$]	$151_{,}$ [136_4]
β_{22}	159_{15}	43_3 [40_3]	40_3 [34_3]	$50_{,}$ [41_3]
β_{33}	235_{15}	221_4 [235_{15}]	215_4 [$235_{,}$]	227_7 [$235_{,}$]
β_{12}	93_8	48_3 [46_4]	$32_{,}$ [33_3]	$47_{,}$ [45_3]
β_{13}	0	-10_8 [0]	4_4 [0]	$-10_{,}$ [0]
β_{23}	0	-4_4 [0]	-4_3 [0]	$-6_{,5}$ [0]
MULTIPLIER	1/2	1.027_3 [1]	$1.024_{,}$ [1]	$1.027_{,}$ [1]
ATOM	Cl	Cl	Cl'	
X	0	361_3 [0]	3438 [0]	
Y	0	2493_3 [1/4]	2483_{31} [1/4]	
Z	4438_6	4439_7 [4438_6]	5758_{84} [5562_4]	
β_{11}	339_1	287_5 [339_1]	161_{28} [339_1]	
β_{22}	339	74_2 [85_2]	31_{113} [85_2]	
β_{33}	955_5	914_{12} [955_5]	999_{1177} [955_5]	
β_{12}	170	73_2 [85_2]	3_{121} [85_2]	
β_{13}	0	12_5 [0]	9_{123} [0]	
β_{23}	0	-4_6 [0]	-68_{395} [0]	
MULTIPLIER	1/6	0.938_4 [1-Ncl']	0.021_4 [1-Ncl']	

NOTES:

(1) All positional parameters, except those written as fractions, have been multiplied by 10^4. All temperature parameters have been multiplied by 10^3. Standard deviations are shown as subscripts.

(2) This column gives the results in $P6_3/m$ with the Cl assumed to be in two-fold disorder about the mirror plane.

(3) Enclosed in brackets after the results obtained in $P2_1/b$ are the parameters obtained in $P6_3/m$ transformed to the equivalent position in the monoclinic cell. The origin of the monoclinic cell was taken at (0, -4, 0) of the hexagonal cell

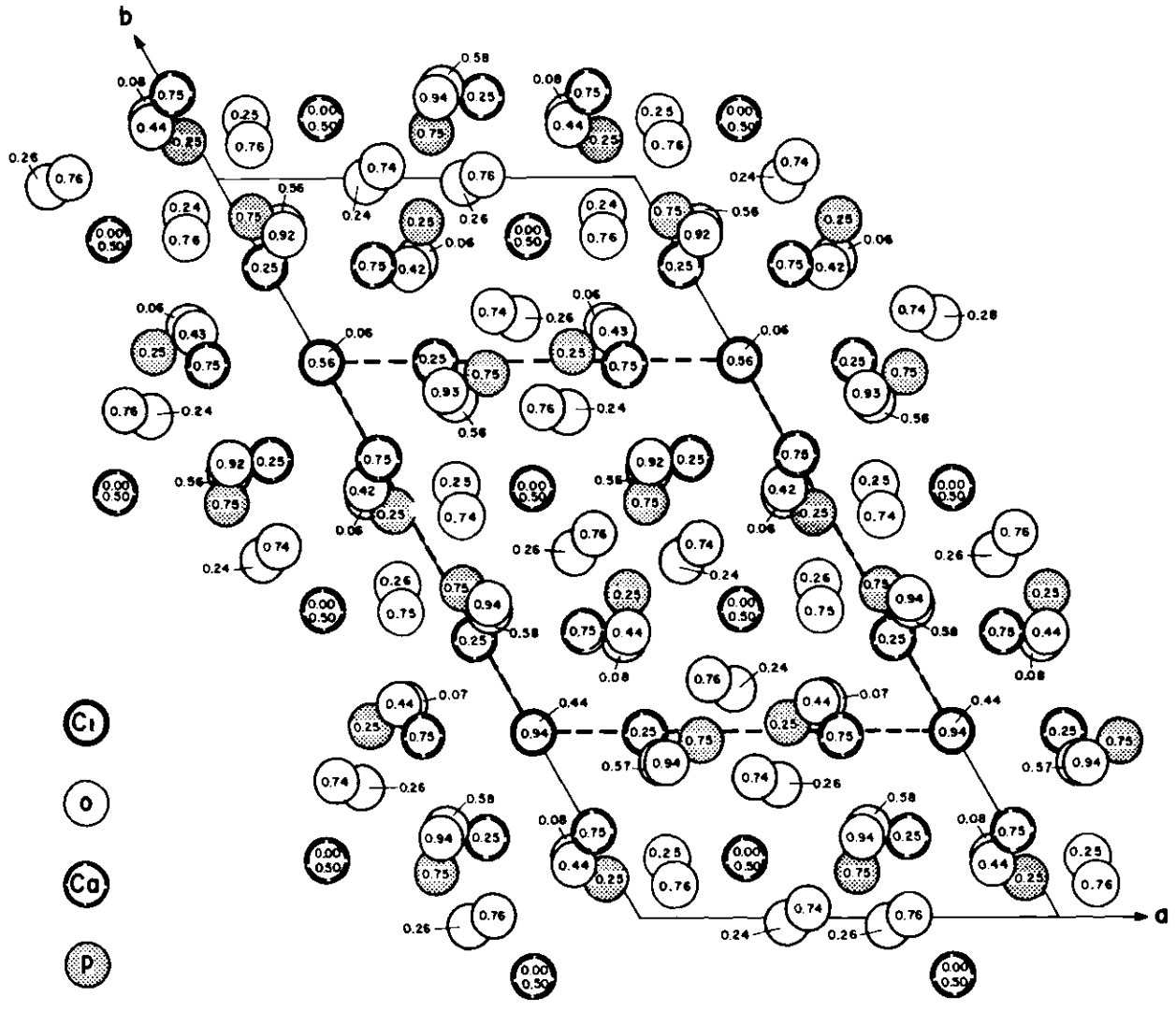

Figure 15. Plan View of Chlorapatite Structure.

of the change of the 6_3 axis to a 2_1 axis). The atom with a prime superscript was, in $P6_3/m$, the mirror image equivalent of the unprimed atom.

The principal departures from the values of the parameters obtained in the hexagonal refinement are the shifts away from z = 1/4 and z = 3/4 of all the atoms previously placed on mirror planes (in $P6_3/m$ mirror planes occur at z = 1/4 and z = 3/4). Furthermore, the β_{33}'s of all the atoms (with the exception of Cl′which has an associated uncertainty greater than 100 per cent) are significantly greater in the hexagonal refinement than in the monoclinic refinement, whereas most of the other thermal parameters are comparable. This is a predictable result because the temperature factors, obtained with the refinement in the space group $P6_3/m$, are trying to simulate the dispersal of the atoms about the mirror planes (in the $P6_3/m$ refinements the O_I, O_{II}, P, and Ca_{II} atoms were constrained to lie on the mirror planes). The thermal parameters parallel to the x-y plane for Ca_I, Ca_I', and Cl are also significantly greater in the $(P6_3/m)$-refinement compared to those in the $(P2_1/b)$-refinement. The positions for these atoms, unlike the others, differ significantly in the x-y plane for the two refinements. In retrospect, all the major differences in the spatial parameters are to be expected if one closely inspects the two sets of anisotropic temperature factors. Thus, the essential differences in the two structures, aside from the new off-mirror-plane atomic positions, are the different positions in the x-y plane for the columnar calciums (i.e., Ca_I and Ca_I') and the chlorine atom. The position of the chlorine atom along the c axis is not at the special position,

$z = 1/2$, as generally presumed (Hendricks, Jefferson, and Mosley, 1932) but is some 0.38 Å away. This position yields a Ca-Cl bond length of 2.80 Å in reasonable agreement with the 2.73 Å bond distance quoted in Sutton (1958) and in contradistinction to a 3.01 Å bond distance that would occur if the chlorine atoms were at $z = 1/2$.

The chlorine atoms which simulated the glide plane by disordered displacements about the mirror planes in $P6_3/m$ now occupy positions which have an ordered displacement from $z = 1/2$. with the direct consequence that the monoclinic b axis is twice that of the hexagonal axis. The doubling of the b axis permits Bragg reflections (those for which k is odd and ℓ nonzero) which do not occur in $P6_3/m$. The presence of these "extra" reflections provided a convenient means of detecting mimetic twinning (twins related by a 120 degree rotation about the pseudohexagonal c axis) which occurred frequently. For an untwinned crystal, only the b axis should be doubled; however, frequently "extra" reflections occurred along the h and $-(h+k)$ directions in reciprocal space also. Single untwinned crystals were selected by taking upper-layer precession and Weissenberg photographs and choosing those crystals for which only one of the three equivalent a axes were doubled.

Of particular interest is the mechanism by which the ordering of chlorine atoms on columns 9.6 Å apart is accomplished and how this doubling of a cell dimension can occur preferentially in one of the three a directions which are equivalent in $P6_3/m$.

The development of a monoclinic structure from the ordering of the Cl-displacements requires both ordering within a column and ordering between columns. The ordering within a column is easily understood in

terms of the rather short Cl-Cl distance of 3.38 Å (compared with 3.87 Å in $CaCl_2$). The question then remains as to how the glide plane is enforced. As is shown by Table 13, the other atoms are displaced rather little from the positions they would occupy in $P6_3/m$. Although the displacement of the chlorine atom from the ideal symmetry position permits formation of electric dipoles, it is probably not reasonable to expect direct dipole-dipole coupling, over a distance of 9.6 Å through many intervening atoms, to be the mechanism of ordering between columns. Instead of such a mechanism, then, one looks for a steric reason, such as a rumpling in the structure, involving displacements from the mirror-plane positions of the hexagonal structure, twisting of the tetrahedra, etc.

Figure 16 and Table 14 are presented at this point for a convenient reference in the discussion to follow. Figure 16 is a stereo-drawing of the immediate surroundings of the screw-axis in the chlorapatite structure. The ellipsoids represent the thermal motion, not atomic size, and correspond to a 90 per cent probability that the center of the atom would be found within the ellipsoid. The phosphorus-oxygen bonds are represented by solid lines whereas atomic co-ordinations are represented with dashed lines. Table 14 contains some of the more important interatomic distances and angles for the synthetic monoclinic chlorapatite structure. The PO_4 tetrahedra are significantly distorted, being elongated along the $P\text{-}O_{II}$ direction. This direction lies essentially in the glide plane. The various dihedral angles within a given tetrahedron differ by as much as 6 degrees, which is $> 50\sigma$. In fluorapatite and hydroxyapatite the PO_4 tetrahedra show this same type

Table 14. Interatomic Distances and Angles for Monoclinic Chlorapatite.

a. IN PO_4 TETRAHEDRA

Atoms*	Angle** (degrees)	Atoms*	Interatomic** distance (Å)
$O_{Ia(0,0)}$ - $P_{a(0,0)}$ - $O_{IIa(0,0)}$	111.33 (8)	$P_{a(0,0)}$ - $O_{Ia(0,0)}$	1.529 (2)
$O_{Ia(0,0)}$ - $P_{a(0,0)}$ - $O'_{IIIa(0,0)}$	111.23 (10)	$P_{a(0,0)}$ - $O_{IIa(0,0)}$	1.544 (1)
$O_{Ia(0,0)}$ - $P_{a(0,0)}$ - $O'_{IIIa(0,0)}$	112.34 (10)	$P_{a(0,0)}$ - $O_{IIIa(0,0)}$	1.530 (2)
$O_{IIa(0,0)}$ - $P_{a(0,0)}$ - $O'_{IIIa(0,0)}$	107.76 (10)	$P_{a(0,0)}$ - $O'_{IIIa(0,0)}$	1.532 (2)
$O_{IIa(0,0)}$ - $P_{a(0,0)}$ - $O'_{IIIa(0,0)}$	106.22 (9)		
$O_{IIIa(0,0)}$ - $P_{a(0,0)}$ - $O'_{IIIa(0,0)}$	107.70 (10)		
$O_{Ib(2,2)}$ - $P_{b(4,3)}$ - $O_{IIb(4,3)}$	111.21 (8)	$P_{b(4,3)}$ - $O_{Ib(2,2)}$	1.531 (2)
$O_{Ib(2,2)}$ - $P_{b(4,3)}$ - $O'_{IIIb(4,3)}$	111.88 (10)	$P_{b(0,0)}$ - $O_{Ib(0,0)}$	1.544 (2)
$O_{Ib(2,2)}$ - $P_{b(4,3)}$ - $O'_{IIIb(4,3)}$	112.07 (10)	$P_{b(0,0)}$ - $O_{IIb(0,0)}$	1.532 (2)
$O_{IIb(0,0)}$ - $P_{b(0,0)}$ - $O_{IIIb(0,0)}$	107.30 (11)	$P_{b(0,0)}$ - $O'_{IIIb(0,0)}$	1.529 (2)
$O_{IIb(0,0)}$ - $P_{b(0,0)}$ - $O'_{IIIb(0,0)}$	106.51 (11)		
$O_{IIIb(0,0)}$ - $P_{b(0,0)}$ - $O'_{IIIb(0,0)}$	107.58 (8)		
$O_{Ic(0,3)}$ - $P_{c(5,0)}$ - $O_{IIc(5,0)}$	111.25 (8)	$P_{c(5,0)}$ - $O_{Ic(0,3)}$	1.529 (2)
$O_{Ic(0,3)}$ - $P_{c(5,0)}$ - $O_{IIIc(5,0)}$	111.49 (9)	$P_{c(0,0)}$ - $O_{IIc(0,0)}$	1.545 (2)
$O_{Ic(0,3)}$ - $P_{c(5,0)}$ - $O'_{IIIc(5,0)}$	112.23 (10)	$P_{c(0,0)}$ - $O'_{IIIc(0,0)}$	1.532 (2)
$O_{IIc(0,0)}$ - $P_{c(0,0)}$ - $O_{IIIc(0,0)}$	107.70 (10)	$P_{c(0,0)}$ - $O_{IIIc(0,0)}$	1.532 (2)
$O_{IIc(0,0)}$ - $P_{c(0,0)}$ - $O'_{IIIc(0,0)}$	106.11 (10)		
$O'_{IIIc(0,0)}$ - $P_{c(0,0)}$ - $O_{IIIc(0,0)}$	107.79 (10)		

b. IN OXYGEN TRIANGLES

Oxygen Triangle with Cl at Center

Atoms*	Interatomic** distance (Å)	Atoms*	Angle** (degrees)
$O'_{IIIa(0,0)}$ - $O'_{IIIb(1,0)}$	5.446 (4)	$O'_{IIIa(0,0)}$ - $O'_{IIIb(0,0)}$ - $O'_{IIIc(2,1)}$	60.00 (4)
$O'_{IIIa(0,0)}$ - $O'_{IIIc(2,1)}$	5.480 (4)	$O'_{IIIa(0,0)}$ - $O'_{IIIc(2,1)}$ - $O'_{IIIb(1,0)}$	59.97 (4)
$O'_{IIIc(2,1)}$ - $O'_{IIIb(1,0)}$	5.466 (4)	$O'_{IIIb(1,0)}$ - $O'_{IIIa(0,0)}$ - $O'_{IIIc(2,1)}$	60.03 (4)

Greatest difference in z coordinates = 0.005 Å, Greatest difference in side lengths = 0.046 (7) Å,

Perimeter = 16.398 (7) Å

Oxygen Triangle without Cl at Center

Atoms*	Interatomic** distance (Å)	Atoms*	Angle** (degrees)
$O_{IIIa(0,0)}$ - $O_{IIIb(1,0)}$	5.189 (4)	$O_{IIIc(2,1)}$ - $O_{IIIb(1,0)}$ - $O_{IIIa(0,0)}$	59.59 (4)
$O_{IIIa(0,0)}$ - $O_{IIIc(2,1)}$	5.154 (4)	$O_{IIIc(2,1)}$ - $O_{IIIa(0,0)}$ - $O_{IIIb(1,0)}$	60.24 (4)
$O_{IIIb(1,0)}$ - $O_{IIIc(2,1)}$	5.185 (4)	$O_{IIIa(0,0)}$ - $O_{IIIc(2,1)}$ - $O_{IIIb(1,0)}$	60.18 (4)

Greatest difference in z coordinates = 0.005 Å, Greatest difference in side lengths = 0.035 (7) Å,

Perimeter = 15.528 (7) Å

c. O-O INTERATOMIC DISTANCES

Atoms*	Interatomic** Distance (Å)
$O_{Ia(0,0)}$ - $O_{IIa(0,0)}$	2.537 (2)
$O_{Ia(0,0)}$ - $O_{IIIa(0,0)}$	2.524 (3)
$O_{Ia(0,0)}$ - $O_{III'a(0,0)}$	2.543 (3)
$O_{IIa(0,0)}$ - $O_{IIIa(0,0)}$	2.483 (2)
$O_{IIa(0,0)}$ - $O_{III'a(0,0)}$	2.460 (2)
$O_{IIIa(0,0)}$ - $O_{III'a(0,0)}$	2.473 (3)
$O_{Ib(7,1)}$ - $O_{IIb(0,0)}$	2.538 (3)
$O_{Ib(7,1)}$ - $O_{IIIb(0,0)}$	2.537 (2)
$O_{Ib(7,1)}$ - $O_{III'b(0,0)}$	2.538 (2)
$O_{IIb(0,0)}$ - $O_{IIIb(0,0)}$	2.477 (2)
$O_{IIb(0,0)}$ - $O_{III'b(0,0)}$	2.463 (2)
$O_{IIIb(0,0)}$ - $O_{III'b(0,0)}$	2.470 (3)
$O_{Ic(3,3)}$ - $O_{IIc(0,0)}$	2.537 (2)
$O_{Ic(3,3)}$ - $O_{IIIc(0,0)}$	2.530 (2)
$O_{Ic(3,3)}$ - $O_{III'c(0,0)}$	2.541 (2)
$O_{IIc(0,0)}$ - $O_{IIIc(0,0)}$	2.484 (3)
$O_{IIc(0,0)}$ - $O_{III'c(0,0)}$	2.459 (3)
$O_{IIIc(0,0)}$ - $O_{III'c(0,0)}$	2.476 (3)

d. Ca_{II}-O INTERATOMIC DISTANCES

Atoms*	Interatomic** Distance (Å)
$Ca_{IIa(0,0)}$ - $O_{Ic(6,2)}$	2.964 (2)
$Ca_{IIb(3,3)}$ - $O_{Ia(0,0)}$	2.973 (2)
$Ca_{IIc(0,0)}$ - $O_{Ib(0,0)}$	2.973 (2)
$Ca_{IIa(0,0)}$ - $O_{IIb(0,0)}$	2.295 (2)
$Ca_{IIb(3,3)}$ - $O_{IIc(3,3)}$	2.301 (2)
$Ca_{IIc(0,0)}$ - $O_{IIa(4,3)}$	2.299 (2)
$Ca_{IIa(0,0)}$ - $O_{IIIa(0,0)}$	2.471 (2)
$Ca_{IIb(3,3)}$ - $O_{IIIb(1,0)}$	2.507 (2)
$Ca_{IIc(0,0)}$ - $O_{IIIc(0,0)}$	2.460 (2)
$Ca_{IIa(0,0)}$ - $O'_{IIIa(0,0)}$	2.609 (2)
$Ca_{IIb(3,3)}$ - $O'_{IIIb(1,0)}$	2.557 (2)
$Ca_{IIc(0,0)}$ - $O'_{IIIc(0,0)}$	2.621 (2)
$Ca_{IIa(0,0)}$ - $O_{IIIb(1,1)}$	2.361 (3)
$Ca_{IIb(3,3)}$ - $O_{IIIc(0,0)}$	2.357 (3)
$Ca_{IIc(0,0)}$ - $O_{IIIa(8,0)}$	2.351 (3)
$Ca_{IIa(0,0)}$ - $O'_{IIIb(7,1)}$	2.314 (3)
$Ca_{IIb(3,3)}$ - $O'_{IIIc(2,0)}$	2.323 (3)
$Ca_{IIc(0,0)}$ - $O'_{IIIa(0,0)}$	2.321 (3)

e. Ca_I-O INTERATOMIC DISTANCES

Atoms*	Interatomic** Distance (Å)
$Ca_{I(0,0)}$ - $O_{Ia(0,0)}$	2.427 (2)
$Ca_{I(0,0)}$ - $O_{Ib(4,3)}$	2.416 (2)
$Ca_{I(0,0)}$ - $O_{Ic(0,0)}$	2.370 (2)
$Ca_{I(0,0)}$ - $O_{IIa(5,3)}$	2.395 (2)
$Ca_{I(0,0)}$ - $O_{IIb(5,3)}$	2.447 (2)
$Ca_{I(0,0)}$ - $O_{IIc(2,0)}$	2.477 (2)
$Ca'_{I(0,0)}$ - $O_{IIa(4,3)}$	2.498 (2)
$Ca'_{I(0,0)}$ - $O_{IIb(4,3)}$	2.438 (2)
$Ca'_{I(0,0)}$ - $O_{IIc(0,0)}$	2.413 (2)
$Ca'_{I(0,0)}$ - $O_{Ia(0,0)}$	2.388 (2)
$Ca'_{I(0,0)}$ - $O_{Ib(4,3)}$	2.397 (2)
$Ca'_{I(0,0)}$ - $O_{Ic(0,0)}$	2.436 (2)
$Ca_{I(8,0)}$ - $O_{IIIa(4,3)}$	2.942 (2)
$Ca_{I(8,0)}$ - $O_{IIIb(4,3)}$	2.850 (2)
$Ca_{I(8,0)}$ - $O_{III'a(0,0)}$	2.655 (2)
$Ca_{I'(0,0)}$ - $O_{III'a(4,3)}$	2.665 (2)
$Ca_{I'(0,0)}$ - $O_{III'b(4,3)}$	2.729 (2)
$Ca_{I'(0,0)}$ - $O_{IIIc(0,0)}$	2.941 (2)

f. Ca_{II}-Cl INTERATOMIC DISTANCES

Atoms*	Interatomic** Distance (Å)
Cl - $Ca_{IIa(0,0)}$	2.789 (1)
Cl - $Ca_{IIb(3,3)}$	2.811 (2)
Cl - $Ca_{IIc(2,1)}$	2.800 (1)

g. O_{III}-Cl INTERATOMIC DISTANCES

Atoms*	Interatomic** Distance (Å)
Cl - $O'_{IIIa(0,0)}$	3.150 (2)
Cl - $O'_{IIIb(1,0)}$	3.148 (2)
Cl - $O'_{IIIc(2,1)}$	3.159 (2)

*$ATOM_{(i,j)}$ is $ATOM_{(0,0)}$ after cell translation i and symmetry operation j have been performed.

j	x'	y'	z'
0	x	y	z
1	x-1	y	z
2	x	y	z-1
3	x	y-1	z-1
4	x-1	y-1	z-1
5	x-1	y-1	z
6	x	y-1	z
7	x-1	y	z-1
8	x	y	z+1

j	x''	y''	z''
0	x'	y'	z'
1	x'	1/2-y'	1/2+z'
2	x'	1/2+y'	1/2-z'
3	x'	y'	z'

**The cell parameters and associated errors used in the interatomic distance and angle calculations were:

a = 9.626±0.005 Å

b = 19.256±0.010 Å

c = 6.764±0.005 Å

$\cos\beta = 0$, $\cos\beta = 0$, $\cos\gamma = -1/2$.

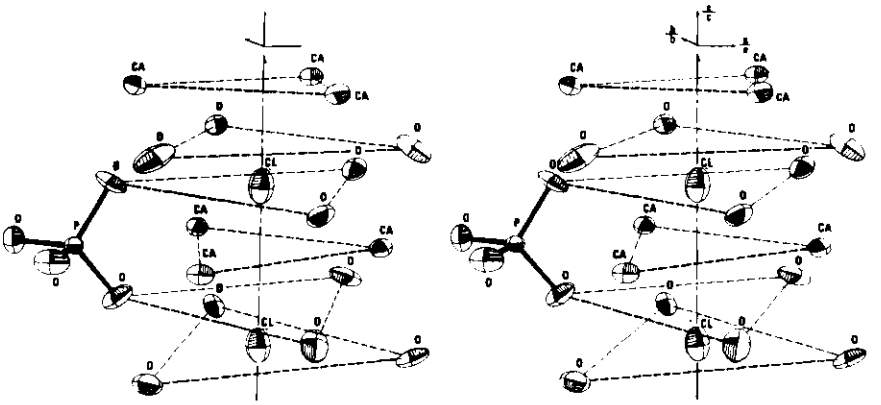

Figure 16. Stereo-View of 6_3 Axis Environment of Monoclinic Chlorapatite.

of distortion in very similar degree (Young, Sudarsanan and Mackie, 1968).

Table 14 shows that statistically significant differences exist along the three crystallographically distinct PO_4 tetrahedra in this monoclinic chlorapatite. Thus, present results support Prener's (1967) expectation of real differences among the phosphate tetrahedra in chlorapatite, on the basis of which he was able to account for the threefold splitting of a fluorescence emission line at about 8600 cm^{-1} in crystals doped with MnO_4-3. Similarly doped fluorapatite did not show such splitting.

The three oxygen atoms nearest the chlorine atom (Figure 16) have very nearly the same z coordinate as does the chlorine atom and thus one might regard the chlorine atom as being approximately in the center of a triangle of O_{III}' atoms in which the chlorine-oxygen distances are 3.15 Å. From Table 14 we see that the perimeter of the O_{III}' triangle, which contains a chlorine atom, is nearly 0.9 Å larger than that of the O_{III} triangle, which does not contain a chlorine atom (Figure 15). In Figure 16 one sees that enlargement of the chlorine-containing O_{III}' triangle tilts the associated PO_4 groups. This tilt carries the ordering information nearly halfway to the next chlorine-atom column. We then require to understand (i) how the ordering information is passed on to the next set of phosphate tetrahedra (attached to the O_{III} triangle surrounding the next chlorine-atom column) and (ii) how the information is now passed differently along the three hexagonal a-axis directions so that they are no longer equivalent, the overall symmetry is lowered and the glide-plane ordering can occur. The answer

to both questions appears to lie in the shift of the position of the Ca_I ion (Table 13). In the hexagonal cell these ions are on a three-fold axis. In the monoclinic cell they are not. The two Ca_I ions at 1/3, 2/3, $\underline{z}$ and 1/3, 2/3, 1/2-$\underline{z}$ in the hexagonal cell are shifted in the monoclinic cell by about 0.05 Å in opposite directions. The sense of these Ca_I shifts is then communicated to the co-ordinating PO_4 groups and their responding small changes, in turn, impose the preferred choice of chlorine position (e.g., z = 0.56 $\underline{vs}$ 0.44) in the next column. In Figure 15, all of the Ca_I shifts are approximately along the [11.0] direction. Such shifts are commensurate with 2_1 symmetry but not 6_3. Thus, the ordering information is propagated differently along the three directions that would be equivalent in an hexagonal structure. This reduction of symmetry is reflected to a lesser degree in the x and y positions of all of the atoms. For example the O_{III} triangle becomes distorted from equilateral (in accord with the change from 6_3 to 2_1) and the chlorine atom moves slightly off the screw axis.

This model for the ordering is also consistent with the observed prevalence of mimetic twinning. The tilting of neighboring PO_4 groups apparently causes the minimum energy position for the Ca_I to occur nearer one PO_4 group than the others (Table 14, part $\underline{e}$), thus destroying the 3-fold symmetry of the Ca_I position. During growth or ordering of the crystal, the initial choice of Ca_I displacement direction would seem to be statistically based. Once made, this initial choice then determines all other Ca_I displacement directions until some interruption in the ideal growth pattern (e.g., vacancies) would permit another initial choice to be made statistically, thus leading to mimetic twinning.

Since the ordering information can reach each column from more than one direction, the absence of one chlorine from one column will not block the ordering. However, it is also clear that, if enough chlorine or Ca_I atoms (or both) are missing, the ordering information could become lost between filled Cl columns. Further it is implied from the structure-refinement results that the occurrence of a chlorine vacancy tends to result in the shift of an adjacent chlorine atom past $z = 1/2$ to the second type of site. Each such "misplaced" chlorine atom will expand the "wrong" oxygen triangle (Figure 16), thus imparting to the adjacent phosphate tetrahedra a tilt counter to that expected for propagation of the glide plane symmetry.

Using synthetic crystals, Prener (1967) experimented with replacing chlorine by fluorine (which then goes to 0, 0, 1/4 in the hexagonal cell) and with driving off chlorine by heating in vacuum. In mineral chlorapatite, Hounslow and Chao (1970) have made observations of the dependence of monoclinic character on chlorine content. Both these works suggest that 10 to 15 per cent of the chlorine atoms can be lost before the glide-plane ordering information fails to be propagated adequately and, in consequence, the hexagonal form becomes observed optically and also (Young and Elliott, 1966) with x-ray diffraction. Prener notes, however, that the splitting of the $\sim 8600\ cm^{-1}$ fluorescence line persists in the observed hexagonal form, which suggests that on a very local level the environment of the phosphate groups has symmetry lower than that imposed by hexagonal space group $P6_3/m$. One could suspect that a similar ordering might occur in hydroxyapatite; that would be a very interesting result in

view of the reported bioelectric effect on bone growth (Bassett, Pawluk and Becker, 1964).

Prener (1967) has commented on the tendency of these flux-grown crystals to be Cl-deficient and has shown (Prener, 1971) that the deficiency occurs by loss of $CaCl_2$ with consequent change in lattice parameters. By comparison with Prener's values, our lattice parameters suggest a Cl deficiency of 3 to 5%. The atomic multipliers in Table 13 corroborate such a Cl deficiency, indicating that only about 95% of the stoichiometric amount of Cl is present. The atomic multipliers for Ca suggest that there is also a deficiency of Ca at least sufficient to affirm loss of $CaCl_2$.

Such implied Cl vacancies would remove the steric restraint, otherwise imposed by Cl-Cl contact, on strict ordering within a Cl-ion column. This would permit individual or groups of Cl ions within a given column to occur, for example, at or near z = 0.06 and 0.56 rather than 0.44 and 0.94. In fact, the rather short Cl-Cl distance along the column (3.38 Å *vs* 3.92 Å for the sum of ionic radii) would seem to promote such displacements of individual Cl ions adjacent to Cl vacancies. On the basis of least-squares analyses of single-crystal x-ray data, Hounslow (1968) and Hounslow and Chao (1970) have reported such disordering in a monoclinic mineral chlorapatite which is also somewhat Cl deficient. Hence, least-squares refinements and difference maps were employed to assess the possibility that, although most of the Cl ions occur at the z = 0.44 and 0.94 sites, some might be present at z = 0.06 and 0.56 sites in the same columns. Least-squares adjustments of all variable parameters led to wR_2 = 3.53% with Cl at only the first

sites. With Cl also permitted at the second sites (refined values $z = 0.08$ and 0.58), $wR_2 = 3.35\%$ was obtained and the site occupancy factor did not fall below approximately 2% (see Cl′ in Table 13). A difference synthesis relating to this point and leading to a similar conclusion, that approximately 2% of the Cl sites of the second kind are filled, is shown in Figure 17.

It seems most probable that this small amount of Cl occurs at the second site because of vacancy-induced disordering, as discussed above. It seems improbable that the apparent occupancy of the second Cl site is due to a small amount of twinning, as the extra reflections associated with it were not observed either with the diffractometer or with long-exposure photographs (precession and Weissenberg).

Dielectric Behavior

A preliminary search for the antiferroelectric character permitted (but not required) by the glide-plane ordering of dipoles has been reported elsewhere (Elliott and Young, 1968). No antiferroelectric effect but, rather, an apparent ferroelectric effect was found. If correct, these observations must mean that the Cl ions are very easily caused to pass to their nearly equivalent positions on the opposite side of 0, 1/4, 1/2 (0, 0, 1/2, in the pseudohexagonal cell) until all (or, at least, more than one-half) of the Cl ions are on the "same" side of the symmetry position, thus destroying the glide plane and leading to a polar space group, probably a subgroup of $P6_3$. The implied movement, for the one half or fewer of the Cl ions that need to move, is from the center of the O_{III}' triangle containing a Cl ion in Figure 16 to the center of the one shown without Cl, the rather small ratio

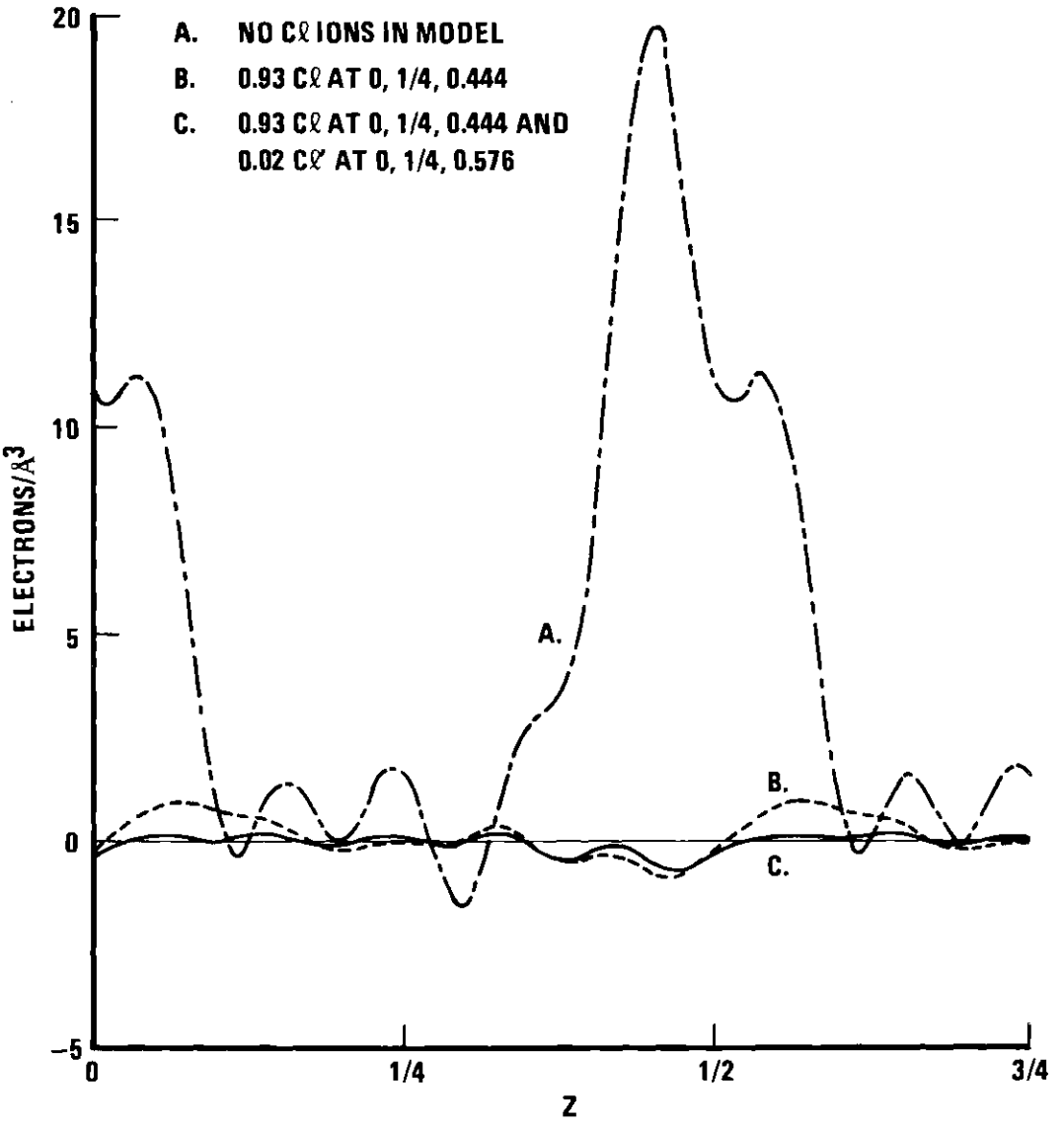

Figure 17. Electron Density Difference Synthesis Along the Screw Axis of Chlorapatite.

($\sim$ 0.4) of r.m.s. thermal-vibrational-amplitude to distance-to-midpoint notwithstanding. The vacancy mechanism postulated to explain occurrence of a small percentage of the Cl ions at the second sites (z = 0.56 and 0.06) could also contribute strongly to such easy shifting of Cl positions. A mechanism would thereby be provided for relatively easy motion of the boundary between antiferroelectrically and ferroelectrically ordered domains and, thus, the occurrence of the ferroelectric property under action of an applied electric field (Elliott and Young, 1968) could be explained.

Synthetic Fluor-Chlorapatite

In this work, calcium-phosphate apatites have been studied for which the F/(F+Cl) ratios varied from zero to one, i.e., from that of stoichiometric chlorapatite ($Ca_{10}(PO_4)_6Cl_2$) to that of stoichiometric fluorapatite ($Ca_{10}(PO_4)_6F_2$). In addition to the fluorapatite and chlorapatite structures, already discussed, the structure refinements were carried out for two fluor-chlorapatites with nominal F/(Cl+F) ratios of 1/10 and 1/3. The composition of the two fluor-chlorapatite samples are presented in Table 15, as obtained from both chemical (Braun, 1970) and x-ray diffraction analyses. The F determination was by the Willard-Winter steam distillation method followed by titration with thorium nitrate. The experimental error in this method of fluorine analysis was estimated to be 10 per cent for G-6-6-1 and 2 to 4 per cent for G-10-1. The site-occupancy factors, which were not constrained to maintain charge balance, indicate a charge imbalance of -0.08 $\pm$ 0.04 electrons per asymmetric unit for sample G-6-6-1 and -0.14 $\pm$ 0.05 for

Table 15. Sample Compositions for G-6-6-1 and G-10-1 (weight per cent)

	CHEMICAL ENTITY	METHOD		
		X-RAY DIFFRACTION	CHEMICAL ANALYSIS	THEORETICAL*
G-6-6-1	Ca	38.12	38.65	38.66
	PO_4	55.59	54.46	54.97
	Cl	5.73	6.44	5.81
	F	0.55	0.40	0.55
G-10-1	Ca	38.01	38.81	38.79
	PO_4	55.50	54.76	55.15
	Cl	4.65	5.13	5.15
	F	1.83	1.29	0.92

*Based on a cell content of $Ca_{10}(PO_4)_6Cl_{2-x}F_x$; where x = 0.3 for G-6-6-1 and x = 0.5 for G-10-1.

sample G-10-1. The asymmetric unit of stoichiometric fluorchlorapatite contains 254 electrons if F/(F+Cl) = 0.5.

The study of these two fluor-chlorapatites provided clues about the mechanism of (i) the observed loss of the ordering responsible for the glide plane, with consequent reversion to $P6_3/m$, (ii) the shift of the Cl position by as much as 0.15 Å from the position found in stoichiometric chlorapatite and (iii) the observed initial stabilization of the monoclinic structure by the substitution of small amounts of F for Cl (Mackie and Young, 1971).

The final refined parameters are presented in Table 16. The values of F/(F+Cl) for G-6-6-1 and G-10-1 were respectively 0.15 and 0.43. The final agreement factors, R_1,

$$R_1 = \frac{\sum \left| |F_{OBS}| - |F_{CAL}| \right|}{\sum |F_{OBS}|} \qquad (53)$$

were 2.2 per cent for G-6-6-1 and 2.6 per cent for G-10-1. Before the single-crystal Bragg-intensity data were collected, long-exposure ($\sim$ 120 hours) upper-layer Weissenberg photographs were obtained of the G-6-6-1 and G-10-1 fluor-chlorapatites. These photographs did not show evidence of twinning nor the presence of monoclinic reflections. Thus, the structures were refined in the space group $P6_3/m$. (Later attempts at refinement of G-6-6-1 in $P2_1/b$ were not successful).

Structure Refinements of the Fluor-Chlorapatites

The final refined parameters of chlorapatite (specimen Syn ClAp-L1-24), transformed to the hexagonal space group, were used as

Table 16. Final Refined Parameter Values of G-6-6-1 and G-10-1 (F/(F+Cl) = 0.15, 0.43).

ATOM	PARAMETER	Parameter Value G-6-6-1	G-10-1
O_I	x	0.3416(1)	0.3366(1)
	y	0.4912(1)	0.4885(1)
	z	1/4	1/4
	β_{11}	0.0056(1)	0.0051(1)
	β_{22}	0.0038(1)	0.0036(1)
	β_{33}	0.0046(1)	0.0046(1)
	β_{12}	0.0039(1)	0.0035(1)
	β_{13}	0	0
	β_{23}	0	0
	MULTIPLIER	0.489(4)	0.505(4)
O_{II}	x	0.5920(1)	0.5905(1)
	y	0.4650(1)	0.4655(1)
	z	1/4	1/4
	β_{11}	0.0020(1)	0.0024(1)
	β_{22}	0.0027(1)	0.0040(1)
	β_{33}	0.0092(2)	0.0104(2)
	β_{12}	0.0009(1)	0.0016(1)
	β_{13}	0	0
	β_{23}	0	0
	MULTIPLIER	0.493(4)	0.512(4)
O_{III}	x	0.3532(1)	0.3501(1)
	y	0.2661(1)	0.2632(1)
	z	0.0670(1)	0.0686(1)
	β_{11}	0.0098(1)	0.0111(2)
	β_{22}	0.0051(1)	0.0052(1)
	β_{33}	0.0065(1)	0.0056(1)
	β_{12}	0.0054(1)	0.0059(1)
	β_{13}	-0.0056(1)	-0.0055(1)
	β_{23}	-0.0037(1)	-0.0038(1)
	MULTIPLIER	1.015(6)	0.984(6)

(Continued on next page)

Table 16. Final Refined Parameter Values of G-6-6-1 and G-10-1 (F/(F+Cl) = 0.15, 0.43). (Continued)

ATOM	PARAMETER	Parameter Value G-6-6-1	G-10-1
P	x	0.4064(0)	0.4036(0)
	y	0.3741(0)	0.3721(0)
	z	1/4	1/4
	β_{11}	0.0021(0)	0.0024(0)
	β_{22}	0.0018(0)	0.0021(0)
	β_{33}	0.0024(0)	0.0023(0)
	β_{12}	0.0012(0)	0.0015(0)
	β_{13}	0	0
	β_{23}	0	0
	MULTIPLIER	0.512(1)	0.525(1)
Ca_I	x	1/3	1/3
	y	2/3	2/3
	z	0.0032(0)	0.0025(0)
	β_{11}	0.0034(0)	0.0035(0)
	β_{22}	0.0034	0.0035
	β_{33}	0.0021(0)	0.0019(0)
	β_{12}	0.0017	0.0017
	β_{13}	0	0
	β_{23}	0	0
	MULTIPLIER	0.329(1)	0.328(1)
Ca_{II}	x	0.2594(0)	0.2545(0)
	y	0.0027(0)	-0.0018(0)
	z	1/4	1/4
	β_{11}	0.0030(0)	0.0050(0)
	β_{22}	0.0033(0)	0.0029(0)
	β_{33}	0.0029(0)	0.0031(0)
	β_{12}	0.0014(0)	0.0014(0)
	β_{13}	0	0
	β_{23}	0	0
	MULTIPLIER	0.489(1)	0.497(1)

(Continued on next page)

Table 16. Final Refined Parameter Values of G-6-6-1 and G-10-1 (F/(F+Cl) = 0.15, 0.43). (Continued)

ATOM	PARAMETER	Parameter Value G-6-6-1	G-10-1
F_I	x	0	0
	y	0	0
	z	1/4	1/4
	β_{11}	0.0028(22)	0.0047(8)
	β_{22}	0.0028	0.0047
	β_{33}	0.0086(38)	0.0127(33)
	β_{12}	0.0014	0.0024
	β_{13}	0	0
	β_{23}	0	0
	MULTIPLIER	0.006(1)	0.038(9)
F_{II}	x	0	0
	y	0	0
	z	0.1604(40)	0.1757(34)
	β_{11}	0.0040(21)	0.0025(8)
	β_{22}	0.0040	0.0025
	β_{33}	0.0091(30)	0.0112(43)
	β_{12}	0.0020	0.0013
	β_{13}	0	0
	β_{23}	0	0
	MULTIPLIER	0.019(1)	0.046(8)
Cl	x	0	0
	y	0	0
	z	0.4429(2)	0.4203(5)
	β_{11}	0.0034(1)	0.0034(2)
	β_{22}	0.0034	0.0034
	β_{33}	0.0200(3)	0.0142(9)
	β_{12}	0.0017	0.0017
	β_{13}	0	0
	β_{23}	0	0
	MULTIPLIER	0.139(1)	0.114(4)

the starting point for the refinements of the two fluor-chlorapatites structures. The least-squares parameters converged rapidly with the exception of the parameters of the fluorine atom located on the screw axis of the structure. The β_{33} thermal parameter of F, perpendicular to the mirror plane of the apatite structure with space group $P6_3/m$, was greatly enlarged. Furthermore, the position of the chlorine atom had shifted along the c axis from that position normally found for chlorine in nearly stoichiometric chlorapatite. In G-6-6-1 (F/(F+Cl)) = 0.15, the chlorine atom was located at z = 0.4429(2) and in G-10-1 (F/(F+Cl) = .43) at z = 0.4203 (c.f., z = 0.4439(2) in pure chlorapatite). It is of interest to note that the chlorine atom was located at z = 0.42 in (F, O, OH, Cl)-apatite (Sudarsanan and Young, 1968). The enlarged β_{33} of the fluorine atom indicated that either (i) the fluorine was not located on the mirror plane or (ii) the scattering density was dispersed about the mirror plane. Difference syntheses were prepared of the electron densities in the volumes surrounding the screw axes of the two fluor-chlorapatites. For these syntheses, chlorine was placed in the model at its refined position (z = 0.4429 for G-6-6-1 and z = 0.4203 for G-10-1) while the fluorine atom was not included in the structure model. Figures 18 and 19 show iso-difference-electron-density contours for the immediate environment of the screw axis of the two structures. Positive difference densities, in units of electron charge, are represented by solid curves and the negative difference densities by dashed curves. Centered at x = 0, y = 1/4 a trimodal distribution of scattering density can be discerned in both structures. To determine the physical

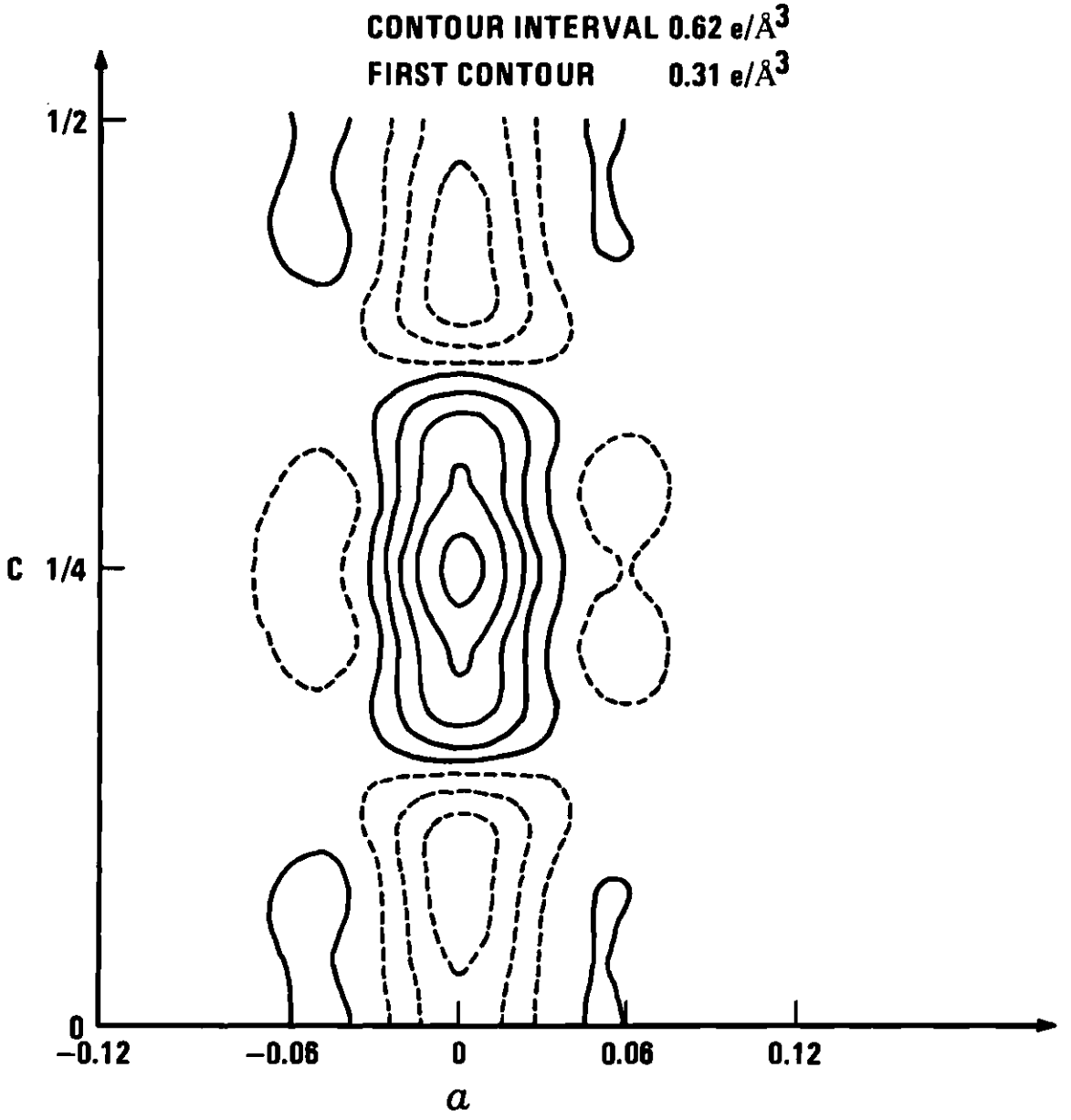

Figure 18. Difference Synthesis In 6_3 Axis Vicinity for G-10-1 (F/(F+CL)=0.43).

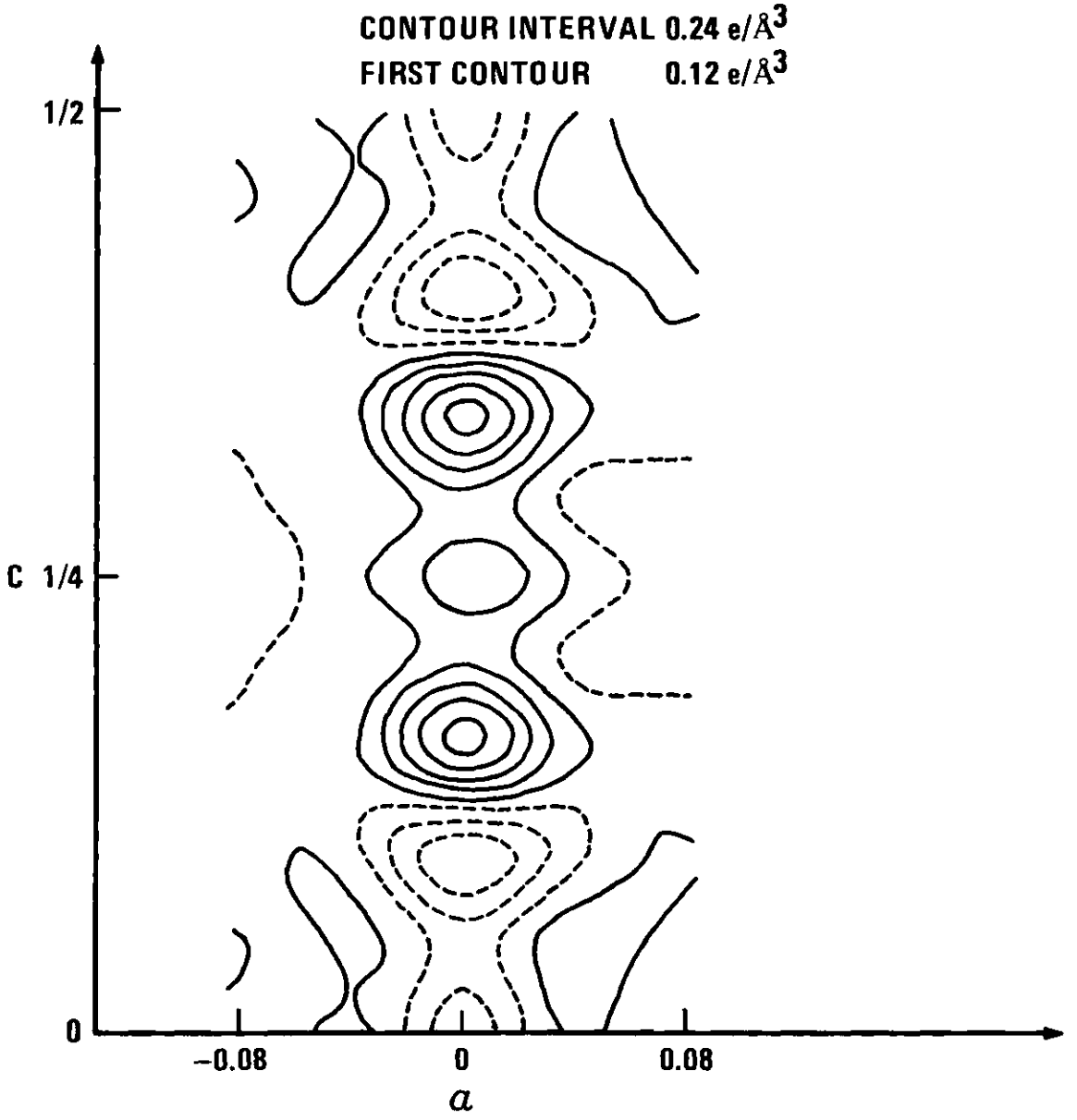

Figure 19. Difference Synthesis In 6_3 Axis Vicinity for G-6-6-1 (F/(F+Cl)=0.15).

significance of this distribution, we first treat the two structures separately.

F/(F+Cl) = 0.43 Fluor-Chlorapatite

Fluorine atoms were then next introduced into the structure model at x = 0, y = 0, z = 1/4, (F_I) and x = 0, y = 0, z = 0.18, (F_{II}). Least-squares structure refinements then led to wR_2 = 4.34 per cent, which compared to 6.3 per cent without F atoms in the model. A subsequent difference synthesis was featureless when contours were drawn with the same contour intervals as used in Figure 18; all residual difference peaks were less than 0.2 electrons /Å^3. At the fluorine sites the residual difference-electron-density was reduced to less than 0.1 electrons /Å^3. In addition, the large negative difference contours, at x = 0, y = 0 above and below the mirror plane, were not present in the full difference synthesis. These negative values were attributed to truncation-of-series effects.

The close proximity of the three fluorines (F_I and two F_{II}) in the structure model prohibited the simultaneous adjustment of all of the fluorine variables. The fluorine thermal parameters, site occupancy factors, and the z of F_{II} were refined in a step-wise iterative procedure; that is, one member of each highly correlated pair of parameters were held constant in each cycle of the refinement. On alternate cycles of refinement, the set of parameters held constant in the previous cycle were allowed to vary while those previously allowed to vary were now held constant.

F/(F+Cl) = 0.15 Fluor-Chlorapatite

The electron density difference synthesis presented in Figure 19 was initially made to verify the correctness of the structural model. However, the structural details were partially masked by large termination-of-series effects. The termination-of-series effects can be eliminated if all of the scattering density is accounted for correctly in the scattering model. Thus, centers of scattering density which appeared in the difference synthesis were added to the scattering model (in the form of F atoms). As each scattering density was placed in the scattering model the termination-of-series effects became smaller and permitted the observation of even smaller residual electron densities. The ultimate goal was a correct model which is implied by a completely zero electron density difference synthesis.

Fluorine was introduced into the structure model for this material at x = 0, y = 0, and z = 0.16. (Initially no fluorine was placed at x = 0, y = 0, and z = 1/4 for it was felt that this central peak in the difference density distribution might be due to a termination-of-series effect. This central peak, in Figure 19, appears to be smaller than the negative termination-of-series peaks at x = 0, y = 0, and z = 0.25 ± 0.15). The data for nine reflections, previously omitted from the least-squares and Fourier analyses, were collected in order to improve the signal-to-noise ratio of any difference peak that might be at x = 0, y = 0, z = 1/4. These nine reflections were selected because their intensities were sensitive to the presence of electron density at that point. The inclusion of these data in the difference syntheses resulted in the mirror-plane

fluorine peak being positive rather than negative. The resulting difference synthesis revealed that a substantive difference peak did indeed exist on the mirror plane at x = 0, y = 0 and that this peak was at least as strong as the off-mirror-plane peaks (Figure 20). For subsequent refinements, a fluorine atom was incorporated into the model on the mirror plane at the screw axis (i.e., at 0, 0, 1/4). Again, as in the refinements of the (0.43)-fluor-chlorapatite only a step-wise iterative refinement procedure could be followed in varying the fluorine parameters. A third difference synthesis revealed that only minor site-occupancy factor adjustments needed to be made (Figure 21) for the fluorine and chlorine atoms. After these adjustments had been made the difference electron density at the fluorine sites was reduced to less than 0.1 electrons /$\mathring{A}^3$. Without fluorine in the model wR_2 was 4.78 per cent; with fluorine in the model this factor was reduced to 4.35 per cent.

It is of interest to note that, while the effect of the inclusion of the trimodal distribution of fluorines in the model was to reduce the R factor from 4.78 to 4.35 per cent, the effect of the inclusion of reflections collected under conditions of simultaneous diffraction was to increase the R factor from 4.35 to 6.04 per cent (see Chapter VI, topic: Simultaneous Diffraction). If the Bragg reflections collected under conditions of simultaneous diffraction had not been removed, it is probable that the central fluorine atom (x = y = 0, z = 1/4) could not have been located unambiguously because (i) the ambient noise level of the difference synthesis would have been greater (indicated by the large increase in the R factor) with a subsequent decrease in the

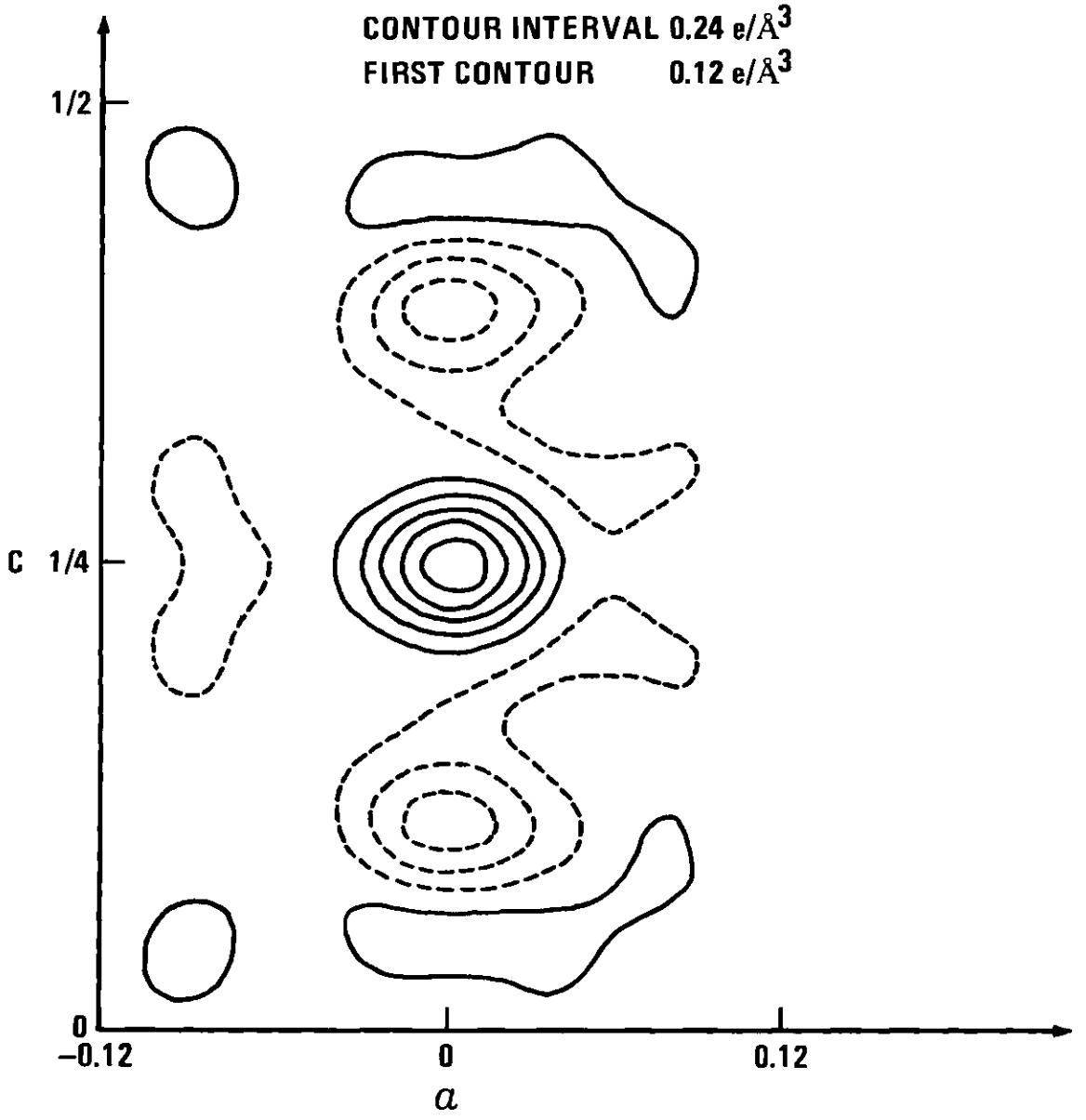

Figure 20. Difference Synthesis In 6_3 Axis Vicinity for G-6-6-1 (F/(F+Cl)=0.15), F_{II} included In the Model.

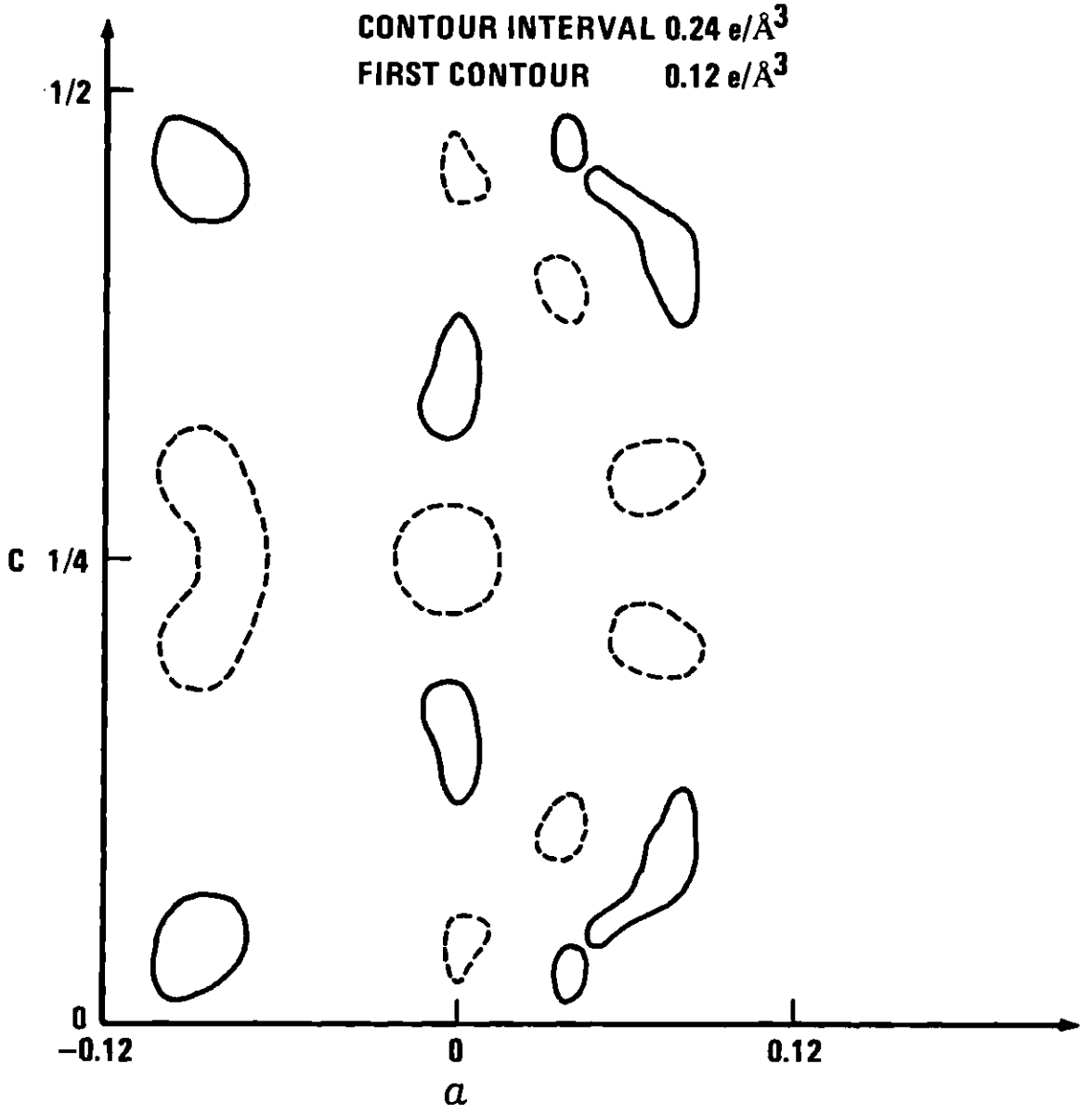

Figure 21. Difference Synthesis In 6_3 Axis Vicinity for G-6-6-1 (F/(F+Cl)=0.15), F_I and F_{II} Included in the Model.

signal-to-noise ratio of the difference peaks; and (ii) at points of high symmetry (e.g., 001/4) the error effects of simultaneous diffraction can build up to as much as 0.5 electron /$Å^3$ (Panke and Wölfel, 1968). The difference peak due to the fluorine atom on the mirror plane was approximately 0.8 electrons /$Å^3$.

Substitutional Models

Several plausible substitution mechanisms are presented in Figure 22 for the assimilation of the fluorine atom into the chlorapatite structure accompanied by changes in the chlorine atom position and site occupancy factor. Each column in Figure 22 is a schematic representation of a possible configuration of fluorine and chlorine atoms along the screw axis of the apatite structure (Mackie and Young, 1971). The open and filled-in circles represent the chlorine and fluorine atoms, respectively. The solid lines represent an edge view of the Ca_{II} triangles which are centered on the screw axis and lie on the mirror planes at z = 1/4 and 3/4. The dashed lines indicate positions mid-way between the mirror planes at z = 0 and 1/2. Each of the four models (A,B,C,D) is for a stoichiometric apatite (no vacancies and two halogens per unit cell). That this is so can be seen if one associates each halogen with the nearest calcium triangle and continues the motif indefinitely. Each calcium triangle will have one, and only one, halogen atom associated with it.

Substitution models with vacancies could readily be devised for defect-apatite structures. But, for those fluor-chlorapatites used in this work, no halogen deficiency was indicated; in fact, an excess of halogens was indicated by both x-ray and chemical analyses. How the

structure might accommodate an excess of halogens will be discussed later.

In each of the four models in Figure 22 a single chlorine atom has been removed and a fluorine placed on the screw axis. In each case, the substitution is not iso-structural; in fact, the fluorine atoms not only occur at positions different from those of the chlorine atoms but the chlorine atom positions also differ from those in pure chlorapatite. Furthermore, the fluorine atom positions differ from those in pure fluorapatite. Substitution models A and B maintain the ordered displacements of the chlorine atoms, required for the monoclinic form of chlorapatite. These two substitutions can be thought of as occurring in two steps; (i) the removal of a chlorine atom from z = 0.44 (the position found in pure chlorapatite) and an accompanying general relaxation of the remaining chlorines on the column toward the vacancy, (ii) the placement of a fluorine atom at z = 1/4 (the ideal position for F in fluorapatite) and the relaxation of the fluorine atom away from the mirror plane toward the chlorine vacancy and away from the nearest, negatively charged, chlorine atom. Thus, although the ordered displacements of the chlorine atoms are maintained, the chlorine atoms are shifted ($\Delta_{z_{Cl}} = 0.0010_3$ and 0.0236_5 for G-6-6-1 and G-10-1 respectively) from their positions in pure chlorapatite and the fluorine atoms is in an off-mirror-plane position.

In models A and B it is clear that, initially, the effect of small amounts of fluorine would be to reinforce the ordered displacements of the chlorines with a concomitant increase in the $P2_1/b$ to $P6_3/m$ transition temperature. Prener (1967) measured optically the

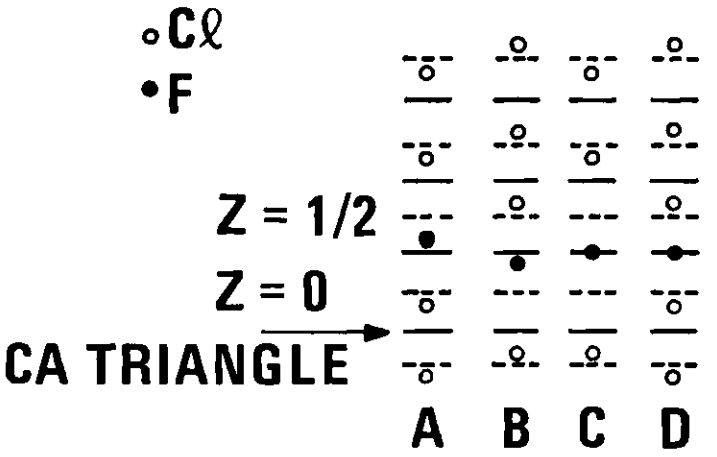

Figure 22. Proposed Substitution Models; ClAp:F.

transition temperatures of fluor-chlorapatites with F/(F+Cl) ratios from zero to 0.36 and reported that the monoclinic form was stabilized for small amounts of fluorine in the chlorapatite structure.

While substitution models A and B tend to stabilize the monoclinic form of chlorapatite, substitutions C and D provide for the occurrence of a reversal of the sense of the chlorine atom displacements from z = 1/2. The random choice of column in which substitution model C occurs would have the effect of removing the glide plane of the $P2_1/b$ structure. Substitution model C can occur only infrequently (if vacancies are not allowed), since C can occur only once per column without an accompanying substitution model D. Both models C and D provide for the occurrence of fluorine on the mirror planes at z = 1/4 and z = 3/4. Substitution model D, however, would be energetically unfavorable because of the small (~ 2 Å) fluorine-chlorine interatomic distance (the sum of the ionic radii is 3.14 Å).

Occurrence of Excess Halogen

Up to this point it has been assumed that only fluorine atoms occupy the sites at z = 0.18, 0.25 and 0.32. Table 17 presents the values of F+Cl and F/(F+Cl) obtained by x-ray and chemical analyses. The value obtained by least-squares analyses, particularly for G-10-1, are larger than the corresponding values found by chemical analyses. If one assumes that both chlorine and fluorine can occur at these sites, then a closer agreement results between the x-ray and chemical analyses (see Table 17).

From Table 17 we see that both x-ray and chemical analyses indicate, for sample G-10-1, a halogen content in excess of the

Table 17. F + Cl and F/(F + Cl) for G-6-6-1 and G-10-1

	F + Cl		
	X-RAY* DIFFRACTION	X-RAY** DIFFRACTION	CHEMICAL ANALYSIS
G-6-6-1	1.97	1.90	2.09
G-10-1	2.38	2.22	2.19

	F/(F + Cl)		
	X-RAY* DIFFRACTION	X-RAY** DIFFRACTION	CHEMICAL ANALYSIS
G-6-6-1	0.15	0.08	0.10
G-10-1	0.43	0.29	0.32

* The structure model assumes that all atoms located at 0, 0, 1/4 ± 0.07 are fluorine;

** A structure model was used in which half of the atoms occupying positions at (0, 0, 1/4 ± 0.07) were assumed to be chlorine rather than fluorine.

stoichiometric quantity of two halogens per unit cell. An explanation of this anomaly requires (i) an arrangement which permits at least three halogens to occur simultaneously on the screw axis within one unit cell, and (ii) a mechanism for charge compensation.

If one assumes that fluorine atoms as well as chlorine atoms can occur at sites heretofore assumed for chlorine, then three sites can be found, among all of the possible sites for halogens on the screw axis, which are nearly equally spaced. One third of the c axis is approximately 2.26 Å. The ionic diameter of three-co-ordinated fluorine (co-ordinated with Ca in this structure) is 2.32 Å (Shannon and Prewitt, 1969). Thus, the difference between the c axial length and three fluorine diameters is less than 3 per cent and it is reasonable to expect that three equally spaced fluorines could occur on the c axis without undue crowding. Three possible sites are z = 0.08, 0.42, and 0.75. The interatomic separations would then be 0.32c, 0.33c, and 0.33c. If one cell out of every five had three halogens, it would be sufficient to explain the excessive halogen content of G-10-1, provided the remaining cells contained a stoichiometric amount of halogen. Charge balance could be maintained with a tri-valent cation. However, these samples were prepared with only $Ca_5(PO_4)_3Cl$, $CaCl_2$, and CaF_2 in the flux and the chemical analysis did not show a lack of material balance sufficient for tri-valent cations to be the means of charge balance. The site-occupancy factor of phosphorus is high relative to the site-occupancy factors of the oxygens. This would be the expected result if a PO_4 group were replaced by a Cl^- to compensate for two extra halogens on the nearby screw axis. Wondratschek

(Brown and Young, 1972) has pointed out that the iodine ion can replace PO_4 in the apatite-like eulytine structure. Thus, it is conceivable that Cl^- could, in this case, substitute for some of the PO_4 groups.

Sterically Imposed Disorder

A possibility exists that the trimodal distribution of scattering density observed in the difference syntheses for G-6-6-1 and G-10-1 may actually be a uniform distribution modified by diffraction effects (Wilson, 1971). Sudarsanan and Young (1971) discuss a similar situation in various cadmium apatites. In a case discussed by them, the halogen, bromine, is too large for the stiochiometric amount to be accommodated on the relatively short c axis without overcrowding. They suggest a sterically imposed disordering of the bromine about the ideal position at z = 1/4. The simplest distribution to assume is a uniform one wherein each successive bromine atom, along a linear chain of contacting bromine atoms, becomes progressively further from z = 1/4 until the placement of the next bromine becomes energetically unfavorable and a vacancy occurs. If the halogen were almost small enough for three to occur with a unit cell distance, a similar process might enable an over-stoichiometric amount of halogens to be accommodated sterically. However, as Wilson (1971) has pointed out, the observed distribution in the Fourier synthesis should have a relative minimum at z = 1/4 for halogen chain lengths greater than 0.10c if the reciprocal space window is ℓ = 14. For ℓ = 13 and 15, this critical chain length is 0.11c and 0.10c respectively. The separation between the apparent off-mirror-plane fluorines is 0.18c and 0.15c for samples G-6-6-1 and G-10-1. Thus, one would expect a relative minimum at z = 1/4 if the halogens were

distributed uniformly. The maximum observed at z = 1/4 indicates that the distribution is trimodal rather than the uniform distribution introduced to account for excess halogen. However, coupled-substitutions, such as the one discussed in the previous paragraph, may account for the excess halogen.

Neodymium-Doped Fluorapatites

Our precision structure refinement techniques (including data collection) were applied to Nd-doped fluorapatite to determine (i) where neodymium resides in the apatite structure, (ii) how the Nd-doped fluorapatite structure differs from fluorapatite, and (iii) how the two FAp:Nd materials produced by the use of the two different dopants differ from each other.

Interest in neodymium-doped fluorapatite stems both from its possible use as an efficient laser crystal and from the prevalance of small quantities of rare-earth impurities in minerological and biological apatites. Particularly in the biological apatites, the structural role of such small impurities may have, ultimately, an important influence on *in vivo* properties. Preliminary studies on Nd-fluorapatite have indicated a laser performance which rivals yttrium aluminum garnet (Mazelsky, Ohlmann, and Steinbruegge, 1968) and $CaWO_4$ (Eaglet, 1970).

Nd-fluorapatite crystals kindly supplied by Eaglet had been grown by the Czochralski method. Both NdF_3 and Nd_2O_3 were used as the dopant. The NdF_3-doped FAp grows faster and has better optical quality than does the Nd_2O_3-doped FAp. However, the latter exhibits better performance as a laser. Why FAp:Nd with the higher optical quality and

growth rate is a poorer laser host is, of course, of great interest to the laser industry.

The samples were prepared with enough neodymium in the melt to replace one per cent of the calciums if the segregation coefficient were unity. The segregation coefficient of Nd in FAp with NdF_3 as a dopant has been measured to be about 0.7 (Eaglet, 1970). When Nd_2O_3 was used as the dopant the segregation coefficient was 0.52 (Mazelsky, Ohlmann, and Steinbruegge, 1968). This would indicate that we should expect to find on the order of 0.4 weight per cent of Nd present in these samples. This represents less than 0.1 Nd per unit cell and the problem of specifying its location is compounded by the fact that this small quantity may occupy a multiplicity of sites. Optical studies have placed Nd^{3+} at Ca_{II} sites (Prener and Piper, 1971). Spectrographic studies with the tri-valent rare-earth Eu substituting in fluorapatite indicated the presence of Eu^{3+} at both Ca_I and Ca_{II} sites when EuF_3 was the dopant and at Ca_{II} sites only when Eu_2O_3 was the dopant (Eaglet, 1970).

The fact that Nd may go into the fluorapatite structure at a site which is not spatially distinct from other atoms (e.g., Ca_I and Ca_{II}) complicates the analysis. If the scattering factor curves are similar in shape, then aside from an overall scaling factor, it will be impossible to determine how much of the scattering density at the calcium site is due to neodymium and not to calcium. This is because the expression for the intensity of a Bragg reflection has as a factor the product of the site-occupancy-factor and the atomic scattering factor. The scattering factor curves for neodymium and calcium have

been plotted in Figure 23, where the curve for calcium has been normalized so that the two curves match at zero scattering angle. Only in the $\sin\theta/\lambda$ region from 0.2 to 1.0 do the first derivatives of the two curves differ appreciably. Fortunately, the x-ray intensity data for both Nd-doped FAp samples did fall in the range $0.36 < \sin\theta/\lambda < 1.0$.

Least-Squares Analyses

Least-squares structure refinements were undertaken with the refined parameters (Chapter VII) of synthetic fluorapatite taken as the starting point. Nine hundred reflections obtained from FAp:NdF_3 were used in the least-squares process. After extinction corrections had been made, the refinements quickly converged to yield wR_2 = 2.92 per cent. Similarly, refinements using 1010 reflections obtained from the FAp:Nd_2O_3 sample yielded wR_2 = 3.87 per cent.

Small but significant differences occurred between (i) the FAp:Nd_2O_3 and FAp:NdF_3 parameters and (ii) those of synthetic fluorapatite. The biggest difference was the relative shift of the Ca_{II} position on the mirror plane, by about 0.01 Å. This, along with the subtle enlargement of the β_{11} temperature factor of Ca_{II} in FAp:NdF_3 and FAp:Nd_2O_3 ($\Delta\beta_{11} \approx 0.0003$) indicated that for both samples Nd might be at, or near, the Ca_{II} site as had been previously suggested by others from various optical studies. The only indication that Nd might also be at the Ca_I site of FAp:NdF_3 was a very small increase (~ 0.006) in the site-occupancy factor over that found for FAp:Nd_2O_3 and FAp. A comparison of the refined parameters of the Nd-doped samples and fluorapatite is made in Table 18. For these refinements neodymium was not included in the structure model.

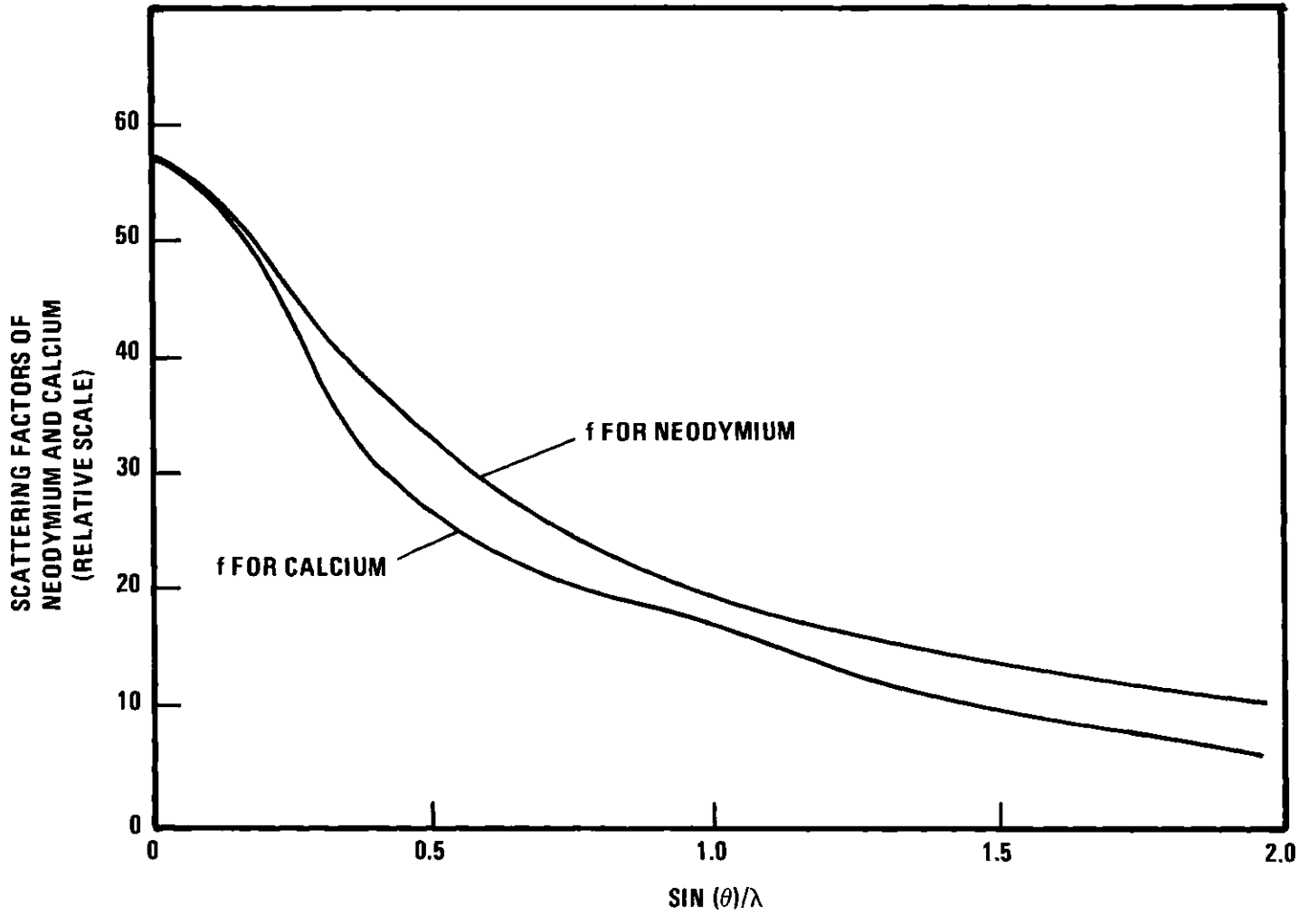

Figure 23. Scattering Factor Curves for Nd and Ca Scaled to Nd.

Table 18. Refined Parameters of Two Nd-Doped and One Pure Fluorapatite; no Nd in the Structure Model.

ATOM	SPECIMEN*	MULT	X	Y	Z
O_I	1	0.500(3)	0.3262(1)	0.4843(1)	1/4
	2	0.500(3)	0.3265(1)	0.4846(1)	1/4
	3	0.500(4)	0.3265(1)	0.4846(1)	1/4
O_{II}	1	0.506(3)	0.5880(1)	0.4668(1)	1/4
	2	0.500(3)	0.5882(1)	0.4670(1)	1/4
	3	0.497(4)	0.5884(1)	0.4669(1)	1/4
O_{III}	1	0.999(4)	0.3416(1)	0.2568(1)	0.0704(1)
	2	1.000(5)	0.3416(1)	0.2567(1)	0.0705(1)
	3	0.996(6)	0.3419(1)	0.2570(1)	0.0704(1)
P	1	0.497(1)	0.3981(0)	0.3688(0)	1/4
	2	0.518(1)	0.3983(0)	0.3691(0)	1/4
	3	0.510(1)	0.3985(0)	0.3691(0)	1/4
Ca_I	1	0.325(1)	1/3	2/3	0.0011(0)
	2	0.331(1)	1/3	2/3	0.0011(0)
	3	0.324(1)	1/3	2/3	0.0011(0)
Ca_{II}	1	0.488(1)	0.2416(0)	-0.0071(0)	1/4
	2	0.500(1)	0.2406(0)	-0.0073(0)	1/4
	3	0.510(1)	0.2401(0)	-0.0073(0)	1/4
F	1	0.157(1)	0	0	1/4
	2	0.153(2)	0	0	1/4
	3	0.150(3)	0	0	1/4

*Specimens: 1 = Pure FAp, 2 = FAp:NdF_3, 3 = FAp:Nd_2O_3

(Continued on next page)

Table 18. Refined Parameters of Two Nd-Doped and One Pure Fluorapatite; No Nd in the Structure Model. (Continued)

ATOM	SPECIMEN*	β_{11}**	β_{22}	β_{33}	β_{12}	β_{13}	β_{23}
O_I	1	35(1)	26(0)	41(1)	23(0)	0	0
	2	34(1)	25(1)	41(1)	23(1)	0	0
	3	34(1)	24(1)	39(1)	23(1)	0	0
O_{II}	1	16(0)	24(1)	70(1)	7(0)	0	0
	2	16(1)	23(1)	73(1)	7(1)	0	0
	3	15(1)	22(1)	66(2)	7(1)	0	0
O_{III}	1	61(1)	31(0)	31(1)	29(0)	-21(0)	-14(0)
	2	62(1)	31(1)	31(1)	30(1)	-22(1)	-14(0)
	3	60(1)	30(1)	28(1)	28(1)	-22(1)	-13(1)
P	1	14(0)	12(0)	17(0)	7(0)	0	0
	2	16(0)	14(0)	22(0)	9(0)	0	0
	3	15(0)	13(0)	18(0)	8(0)	0	0
Ca_I	1	30(0)	30	20(0)	15	0	0
	2	29(0)	29	22(0)	15	0	0
	3	28(0)	28	18(0)	14	0	0
Ca_{II}	1	22(0)	20(0)	27(0)	11(0)	0	0
	2	25(0)	20(0)	28(0)	11(0)	0	0
	3	26(0)	20(0)	25(0)	12(0)	0	0
F	1	25(1)	25	129(3)	12	0	0
	2	24(1)	24	139(3)	12	0	0
	3	24(1)	24	117(4)	12	0	0

*Specimens: 1 = Pure FAp, 2 = FAp:NdF_3, 3 = FAp:Nd_2O_3

**Temperature factors have been multiplied by 10^4.

Inclusion of neodymium in the structure models of FAp:Nd_2O_3 and FAp:NdF_3 at the Ca_{II} position did not lead to significant reductions in wR_2 but the Ca_{II} parameters still differed from those found with the fluorapatite sample. Further refinements, allowing neodymium to assume a slightly different position ($\sim$ 0.05 Å) from Ca_{II}, reduced wR_2 (from 2.92 to 2.77 per cent for FAp:NdF_3; from 3.87 to 2.80 per cent for FAp:Nd_2O_3) and increased the agreement between the positional parameters found for Ca_{II} in fluorapatite compared to those found with the two Nd-containing fluorapatites.

The final least-squares-refinement results for the parameters for the two Nd-containing fluorapatites and for fluorapatite are presented in Table 19. Neodymium was not placed at the Ca_I site in FAp:NdF_3, because the amount indicated by the final site-occupancy-factor is less than one standard deviation. The amount of neodymium indicated at the Ca_{II} sites of FAp:NdF_3 and FAp:Nd_2O_3 is approximately 7 weight per cent or half a neodymium per unit cell. The standard deviation of the site-occupancy factor of neodymium is 18 per cent. Thus, a conceivable three-standard-deviation error could lead to closer agreement with the 3.8 weight per cent found for neodymium by electron microprobe analysis (Johnson, 1971). The sample compositions are given in Table 20. The sample compositions determined by electron microprobe analysis differ significantly from that found from the least-squares refinements. In the ensuing discussion on charge-balance mechanisms the source of these differences will be considered.

For those specimens used in this work, the difference between the neodymium-containing fluorapatite and fluorapatite structures appears

Table 19. Refined Parameters of Two Nd-Doped and One Pure Fluorapatite.

ATOM	SPECIMEN*	MULT	X	Y	Z
O_I	1	0.500(3)	0.3262(1)	0.4843(1)	1/4
	2	0.498(3)	0.3264(1)	0.4845(1)	1/4
	3	0.502(3)	0.3265(1)	0.4846(1)	1/4
O_{II}	1	0.506(3)	0.5880(1)	0.4668(1)	1/4
	2	0.505(3)	0.5882(1)	0.4670(1)	1/4
	3	0.499(3)	0.5883(1)	0.4669(1)	1/4
O_{III}	1	0.999(4)	0.3416(1)	0.2568(1)	0.0704(1)
	2	0.995(4)	0.3416(1)	0.2567(1)	0.0705(1)
	3	0.999(4)	0.3419(1)	0.2570(1)	0.0704(1)
P	1	0.497(1)	0.3981(0)	0.3688(0)	1/4
	2	0.515(1)	0.3983(0)	0.3691(0)	1/4
	3	0.507(1)	0.3985(0)	0.3691(0)	1/4
Ca_I	1	0.325(1)	1/3	2/3	0.0011(0)
	2	0.329(1)	1/3	2/3	0.0010(0)
	3	0.324(7)	1/3	2/3	0.0011(0)
Ca_{II}	1	0.488(1)	0.2416(0)	-0.0071(0)	1/4
	2	0.359(25)	0.2419(3)	-0.0068(3)	1/4
	3	0.358(24)	0.2425(5)	-0.0067(5)	1/4
Nd_{II}	1	0	--	--	--
	2	0.040(7)	0.2368(10)	-0.0089(8)	1/4
	3	0.040(7)	0.2331(16)	-0.0094(12)	1/4
F	1	0.157(1)	0	0	1/4
	2	0.152(2)	0	0	1/4
	3	0.151(2)	0	0	1/4

*Specimens: 1 = Pure FAp, 2 = FAp:NdF_3, and 3 = FAp:Nd_2O_3

(Continued on next page)

Table 19. Refined Parameters of Two Nd-Doped and One Pure Fluorapatite. (Continued)

ATOM	SPECIMEN*	β_{11}**	β_{22}	β_{33}	β_{12}	β_{13}	β_{23}
O_I	1	35(1)	26(0)	41(1)	23(0)	0	0
	2	34(1)	25(1)	41(1)	24(1)	0	0
	3	35(1)	26(1)	40(1)	24(1)	0	0
O_{II}	1	16(0)	24(1)	70(1)	7(0)	0	0
	2	15(1)	23(1)	72(1)	7(1)	0	0
	3	15(1)	23(1)	68(1)	7(1)	0	0
O_{III}	1	61(1)	31(0)	31(1)	29(0)	-21(0)	-14(0)
	2	61(1)	31(1)	31(1)	29(1)	-22(1)	-14(0)
	3	61(1)	30(1)	30(1)	29(1)	-22(0)	-14(0)
P	1	14(0)	12(0)	17(0)	7(0)	0	0
	2	16(0)	14(0)	21(0)	8(0)	0	0
	3	15(0)	14(0)	19(0)	8(0)	0	0
Ca_I	1	30(0)	30	20(0)	15	0	0
	2	29(0)	29	22(0)	15	0	0
	3	29(0)	29	19(0)	14	0	0
Ca_{II}	1	22(0)	20(0)	27(0)	11(0)	0	0
	2	18(2)	21(1)	23(2)	9(1)	0	0
	3	18(1)	20(1)	24(1)	9(0)	0	0
Nd_{II}	1	--	--	--	--	--	--
	2	40(5)	16(4)	39(5)	15(3)	0	0
	3	37(5)	16(2)	24(2)	14(3)	0	0
F	1	25(1)	25	129(3)	12	0	0
	2	24(1)	24	139(3)	12	0	0
	3	23(1)	23	123(3)	12	0	0

*Specimens: 1 = Pure FAp, 2 = FAp:NdF_3, and 3 = FAp:Nd_2O_3

**Temperature factors have been multiplied by 10^4.

Table 20. Sample Compositions for FAp:NdF_3 and FAp:Nd_2O_3 (weight per cent).

CHEMICAL ENTITY	SAMPLE*	METHOD		
		X-RAY DIFFRACTION	ELECTRON MICROPROBE	X-RAY** DIFFRACTION
Ca	1	32.8	37.8	36.4
	2	32.7	--	36.2
PO_4	1	56.9	55.3	57.0
	2	57.0	--	57.1
F	1	3.4	2.9	3.4
	2	3.4	--	3.4
Nd	1	6.9	3.8	3.3
	2	6.9	--	3.3

*Sample: 1 = FAp:NdF_3, 2 = FAp:Nd_2O_3

**Site-occupancy factor of Ca_{II} increased by 3σ to 0.434 and the site-occupancy factor Nd_{II} was decreased by 3σ to 0.019.

to be only in the placement of a small amount of neodymium near (but not exactly at) the Ca_{II} site. The amount, if any, of Nd at the Ca_{I} site in FAp:NdF_3 was shown to be less than 0.02 weight per cent; similarly that at the Ca_{I} site in FAp:Nd_2O_3 was even less.

Charge-Balance Mechanism

Two charge-balance mechanisms have been postulated: (i) vacancies, $Ca_{5-3x/2}Nd_x(PO_4)_3F$ and (ii) the coupled substitution of Nd^{+3} for Ca^{+2} and O^{-2} for F^{-1}, $Ca_{5-x}Nd_x(PO_4)_3F_{1-x}O_x$. Neither of these mechanisms were imposed during least-squares refinements. That is, site-occupancy factors were allowed to vary without imposition of constraints. Site-occupancy factors, prior to the introduction of neodymium into the structure, indicated a charge imbalance of $+0.37 \pm 0.09$ and $+0.42 \pm 0.11$ electrons per unit cell for FAp:NdF_3 and FAp:Nd_2O_3, respectively. After refinements with neodymium in the structure, the apparent charge imbalance was -1.67 ± 0.66 and -1.92 ± 0.62 electrons per unit cell. In both cases the numbers of electrons associated with the PO_4 group, fluorine and Ca_{I} remained unchanged (within several hundredths of an electron) after the introduction of the neodymium. However, the net positive charge associated with the Ca_{II} site and nearby Nd_{II} site decreased by approximately 2 electrons. An error of three standard deviations in the Ca_{II} site-occupancy factor would account for 1.8 electrons of the charge imbalance. As a possibly instructive exercise, the indicated compositions by weight and the charge imbalance were therefore recalculated on the assumption that the site-occupancy factors were in error by -3σ for Ca_{II} and $+3\sigma$ for Nd_{II} (since the Ca_{II} and Nd_{II} multipliers are almost exactly negatively correlated). The charge imbalance then

calculated was -0.6 ± 0.7 electrons per unit cell. The compositions thus indicated (Table 19) as consistent with the x-ray structure refinement are in close agreement with the electron microprobe analysis.

CHAPTER VIII

CONCLUSIONS

Introduction

The techniques for collecting single-crystal Bragg intensity data, which were developed and evaluated in the course of this work, yielded significant precision (unattainable with any existing technique) in the least-squares refined parameters. This newly attained precision in atomic-scale detail was used to develop atomic-scale models which could account for certain observed properties on a macroscopic scale.

In what follows, a number of conclusions about the data collection techniques and about the crystal structures themselves are abstracted from the text and presented in summary form.

"Typical" vs "Controlled-Precision" Techniques

The application of the two different techniques ("typical" and "controlled-precision") to the same sample indicated that, for an allotted total time T to complete an experiment, one will be able to detect smaller physically significant parameter differences, with the "controlled-precision" than with the "typical" technique. From the case presented in Chapter VI, it was concluded that 25 per cent more time would be required to obtain the same wR_2 with the "typical" technique than with the "controlled-precision" technique. The use of the "controlled-precision" technique is preferred over the "typical"

technique because improved statistical precision can be obtained, simultaneous diffraction effects can be reduced and malfunctioning equipment detected without an increased expenditure of time.

The less precise ("typical") technique did not result in refined structure parameters demonstrably in error in comparison to the results with the "controlled-precision" technique; they were simply less well determined by, in this case, approximately a factor of two.

On the basis of tests with artifically added random errors and the half-normal probability plot (Figure 11, Chapter VI) of the differences in the refined parameters, it was concluded that (a) the least-squares standard deviations (in the 25 per cent random error example) were systematically too small (i.e., to account for the observed differences in the parameters) by 30 to 40 per cent, (b) addition of the random errors to the intensity data did not introduce systematic errors in the least-squares results, and (c) the addition of errors did not prevent convergence in the refinement process even though psuedo symmetry was present.

Simultaneous Diffraction and Extinction

Significant simultaneous diffraction effects ($> 3\sigma$) occurred for 14 to 34 per cent of the data collected from the apatite specimens (see Table 6, Chapter VI). Three standard deviations was at least 3 per cent, generally more, of the Bragg intensity. The occurrence of intrinsic simultaneous diffraction was still significant (> 17 per cent) for asymmetrical settings of the crystal relative to the ϕ axis of the diffractometer. The frequency of occurrence of detectable simultaneous

diffraction was approximately proportional to crystal size (see Figure 14).

Inclusion of the data affected by simultaneous diffraction in the least-squares refinements revealed that: (a) the structure parameters remained unchanged (within 3σ, where σ is the pooled standard deviation for the two refinements), (b) the R factor (wR_2) increased 39 per cent (from 4.35 to 6.04 per cent) and the average standard deviation, obtained from the least-squares process, increased 40 per cent, and (c) the extinction constant, $\underline{c}$, more than doubled (see Table 8, Chapter VI). Thus, if any physical interpretation is to be given the extinction constant, $\underline{c}$, one must correct for simultaneous diffraction (no procedure known at this time) or remove the affected data before the extinction correction procedure is applied. Also, identifying and removing those reflections presumably affected by simultaneous diffraction did improve the precision with which the final parameters were known.

Extinction corrections, routinely applied to all data, resulted in significant improvements in the R factors (wR_2) for all data sets (see Table 10, Chapter VI); a 57 per cent reduction occurred in one case (10.15 to 4.35 per cent). These samples did not exhibit severe extinction effects, the largest correction to any reflection intensity was only $\sim$ 15 per cent.

Atomic Scale Bases for Some Apatite Properties

Detailed knowledge of the various apatite structures studied in this work permitted atomic-scale models to be proposed which provide

for an explanation of the occurrence of some of their macroscopic properties. Some of the observed physical properties for which atomic-scale models have been presented in this work are:

(1) The occurrence of a monoclinic form of chlorapatite.

(2) The preferential doubling of only one a axis of hexagonal chlorapatite to form the monoclinic structure.

(3) The prevalence of mimetic twinning in chlorapatite.

(4) The initial inhibition and eventual promotion of the monoclinic to hexagonal phase transition with increasing substitution of fluorine into the chlorapatite structure.

(5) The three-fold splitting of the 8600 cm^{-1} fluorescence line in MnO_4-doped chlorapatite.

APPENDIX A

INITIALIZATION OF THE DATA COLLECTION

Introduction

The control program was designed to collect precise integrated Bragg intensities from single-crystal specimens. The machine-language interface-control subroutines are those written by W. R. Busing (1968) and modified by the programming group of Picker Corporation (Cleveland) for the FACS-I system. The methods and manner of the data collection strategy were developed by us in the course of the present work.

The programming system is modular in that it is composed of numerous overlays which are stored semi-permanently on a disk mass-storage device, and these overlays are called sequentially into core for execution. Each overlay is essentially a single or closely related group of logical operations.

For example:

(1)

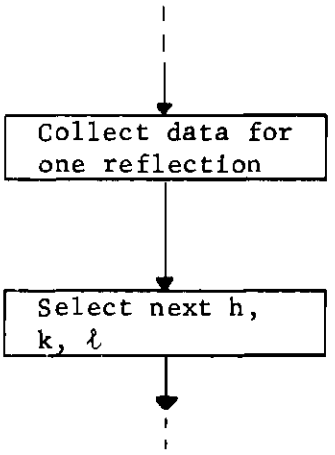

(2)

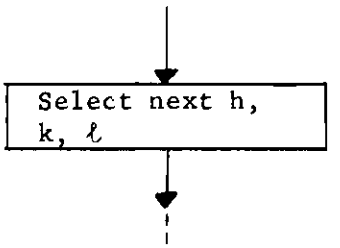

the box representing h, k, ℓ selection is an overlay, and thus one could substitute box 2 for box 1 and obtain a different method of h, k, ℓ selection without disturbing the rest of the programming. Of course, the overlay represented by box 2 must be written with full regard to intercommunication with other overlays, overlay 2 may need information created by the rest of the program, and overlay 2 may create results needed by the rest of the program.

An overlay is brought into core memory by the following sequence of assembly language commands:

```
JMS I .+3
EAOVERLAY
DMAOVERLAY
7736
```

where EAOVERLAY and DMAOVERLAY are respectively the disk extended address and disk memory address of the first location of the overlay on the disk.

Initialization Program

The disk monitor responds to one-letter keyboard commands. The crystal alignment program is brought into core by means of the resident disk monitor. Typing the letter "A" will bring the alignment program into core. Typing "/BC" will then bring the data collection program into core. To initialize the data collection program one types "/IN" and then types:

(1) the number of degrees you want to rotate about the diffraction vector,

(2) unimplemented parameter, reserved for future expansion, type "1",

(3) 1/2 of the basic peakwidth in degrees 2θ,

(4) statistical precision desired (e.g., for 1% type 0.01),

(5) time in minutes that you want between the standard reflections,

(6) maximum number of times you want to scan one reflection, at one angular setting of the diffraction vector,

(7) wavelength of the $K\alpha_1$, radiation used, in Å,

(8) wavelength of the $K\beta$ radiation of the target material used, in Å,

(9) wavelength of the β-filter absorption edge in Å,

(10) h, k, ℓ Miller indices of the standard reflection.

The program segment which accepts this initialization information is an overlay, thus changes can be made easily to read in additional or different information.

APPENDIX B

OPTIMIZATION OF THE VARIANCE OF THE INTEGRATED NET INTENSITY OF A BRAGG REFLECTION

Single-Scan or Single-Filter Case

Let I_N be the integrated net intensity, I_A the number of counts accumulated while the detector is scanned over the peak, I_C the number of counts accumulated while the detector is scanned over the background on both sides of the peak. If t represents the ratio of time spent on the peak to the time spent on the background on both sides of the peak, then:

$$I_N = I_A - t\, I_C \tag{54}$$

where a linear background has been assumed and extended under the Bragg peak. The variance of I_N will be

$$\sigma^2(I_N) = I_A + t^2\, I_C \tag{55}$$

and the fractional standard deviation will be

$$\sigma(I_N)/I_N = (I_A + t^2\, I_C)^{\frac{1}{2}}/(I_A - t\, I_C) \quad . \tag{56}$$

Let t_A and t_C be the times spent on the peak and total background respectively. If $t_A + t_C = K$ (K a constant) and $t = t_A/t_C$, then I_A and I_C can be rewritten:

$$I_A = (K - t_C)i_A \tag{57}$$

$$I_C = t_C i_C \tag{58}$$

where i_A and i_C are average count rates for the peak and background respectively. If one uses equations (57) and (58), then equation (56) can be rewritten as:

$$\sigma(I_N)/I_N = (i_A(K - t_C) + ((K - t_C)^2 i_C t_C)^{\frac{1}{2}}$$

$$/(i_A(K - t_C) - ((K - t_C)/t_C)i_C t_C) \quad . \tag{59}$$

Minimizing the fractional standard deviation with respect to t_C we obtain:

$$i_A/(K - t_C)^2 - i_C/t_C^2 = 0 \quad . \tag{60}$$

Let $S = (i_A - i_C)i_C$ (S is the signal-to-noise ratio) and substitute S into equation (60) to obtain

$$(1 + S)/t_A^2 - 1/t_C^2 = 0 \quad . \tag{61}$$

and

$$t^2 = 1 + S \quad . \tag{62}$$

Double-Filter or Double-Scan Case

If one follows a similar approach with a double-filter scan we obtain

$$t^2 = \frac{i_A + i_B}{i_C + i_D} \tag{63}$$

where i_A and i_B are the average count rates for the scans of the peak with the A and B filters respectively and i_C and i_D are the average count rates for the backgrounds obtained with the A and B filters respectively.

If the filters are balanced

$$i_C \approx i_D \tag{64}$$

and equation (63) reduces to

$$t^2 \approx \tfrac{1}{2}\frac{i_A}{i_C} + \tfrac{1}{2}\frac{i_B}{i_D} \tag{65}$$

or

$$t^2 \tfrac{1}{2}(1 + S_A) + \tfrac{1}{2}(1 + S_B) \tag{66}$$

where S_A and S_B are the signal-to-noise ratios obtained with the A and B filters respectively. Equation (66) can be rewritten

$$t^2 \quad 1 + \tfrac{1}{2} S_A + \tfrac{1}{2} S_B \quad . \tag{67}$$

If the A filter is the alpha-filter of an alpha-beta balanced-filter pair, then

$$S_A \approx 0 \tag{68}$$

and equation (67) becomes

$$t^2 \approx 1 + \tfrac{1}{2} S_B \quad . \tag{69}$$

APPENDIX C

DETAILS OF DATA COLLECTION

Two-Pass Data Collection Strategy

Usually, due to limitations of resources and time, a fixed total time T is specified within which the data collection must be completed. In most cases, the total number of Bragg reflections accessible for measurement exceeds by many times the number which can be measured within the constraint of a total time T for the experiment. The question of how one allocates the available time T in collecting the data has two parts:

1. How does one divide the time among the various accessible reflections consistent with the goals of the experiment (e.g., optimizing the weight of certain structure parameters, etc.)?

2. Given a time t_i, for measurement of a given reflection, how much time does one spend determining the peak intensity and how much time determining the back-ground intensity? (e.f., Chapter III)

To answer the above questions, one needs a prior knowledge of the Bragg intensities (i.e., one must, in principle, know the structure beforehand). Many authors (Shoemaker, 1968; Young, 1969; Arndt, 1964; Kaplow and Posen, 1969; Arndt and Willis, 1966) have pointed out the need for prior knowledge or survey information, in determining an optimum strategy for collecting x-ray intensity data which will best serve the purpose for which they were gathered. If one wants to determine

only the gross features of a structure, a very rapid determination of the integrated Bragg intensities would be sufficient (Killean, 1967). In the event that more structural details are desired, the initial rapid intensity determination may be used to obtain an optimized division of time for a re-collection of the intensity data. If the structure of interest has been previously solved, then that solution for the structure could serve as a model for calculating intensities, enabling one to by-pass the first pass of a two-pass process.

The Datex Controller, which lacked the closed-loop feature of the computer-controlled diffractometer, was used to collect the data in two distinct passes. The first pass consisted of an initial, cursory collection of the intensities of all the reflections to be eventually collected and then, based on an elementary analysis of the initial data for signal-to-noise ratio and integrated intensities, a second collection with optimized times was performed.

The closed-loop nature of the computer-controlled diffractometer allowed both passes to be made in an interleaved fashion. Thus, to the casual observer the data collection procedure would appear to be a single pass over all of the data.

Mounting Specimens

The spherical crystals were affixed to the ends of quartz-glass fibers with collodion and the glass fibers in turn, were mounted on brass plugs with jeweler's wax. The stem of the brass plug was then mounted on a standard goniometer head.

Centering Crystal and Determining Orientation Matrix

To collect data from a single-crystal with a diffractometer, one must position the crystal at the center of the sphere of confusion. This is easily accomplished by observing the motion of the crystal relative to the reticle of a telescope. As each axis of the diffractometer is rotated in turn, the crystal's position will not translate in space if the crystal lies on that axis.

After centering the crystal on the diffractometer, one must determine the orientation of the crystal lattice relative to the goniostat. The angle-setting calculations for the Datex controlled diffractometer were done with an off-line computer and so it was convenient purposefully to align the ϕ-axis of the diffractometer along the c* direction of the reciprocal lattice of the apatite crystal. This practice of aligning a direction of high symmetry along the ϕ-axis of the diffractometer enhances the probability of occurrence of simultaneous diffraction events and, thus, is a practice which should be avoided when precise data are required. With the computer-controlled diffractometer, a record of the orientation of the crystal is maintained in the computer as a general orientation matrix. The angle setting calculations are, then, done on-line in real-time with equal convenience for general or special orientations of the crystal relative to the goniostat. In fact, even though the crystals had been previously aligned for Weissenberg of precession photographs, our standard procedure was to offset the goniometer head arcs several degrees from the aligned settings and then to obtain a new orientation matrix for this general setting.

Wavelength Selection

The radiation used in collecting the data from all specimens was the $K\alpha$ doublet emitted from the excited molybdenum target. Molybdenum, rather than copper, was chosen for several reasons. More reflections are accessible with the shorter wavelength of $MoK\alpha$. The apparent increase in the number of collectable reflections is real, for with apatites reflections with signal-to-noise ratios greater than one exist all the way out to at least 120° 2θ, notwithstanding the $\sin\theta/\lambda$ dependence of the temperature factor. For a given crystal, the absorption correction will be less if molybdenum $K\alpha$ radiation is utilized rather than copper $K\alpha$ because of the λ^3 dependence of μ/ρ. Furthermore, as equations (30) and (31) in Chapter III make apparent, the extinction corrections will also be smaller with molybdenum than with copper radiation. However, the chance that simultaneous reflections will occur is greater because of the larger Ewald sphere associated with $MoK\alpha$. Anomalous dispersion can be useful in solving a structure, however in structure refinements it becomes necessary to correct for this phenomenon. It is usually best to avoid, or at least minimize, the need for corrections, since every correction factor has an attendant error associated with it. From Table 21 we can see that for the atoms in the apatites observed, the anomalous dispersion corrections are less with $MoK\alpha$ than with the two other commonly used target materials, Cu and Fe (Cromer, 1965).

Because of reduced intensity, uncertainty in the polarization correction, and the non-uniform reflectivity over its surface a monochromator was not used. But a pulse height discriminator was used in

Table 21. Anomalous Dispersion Corrections for Various Atoms and Wavelengths

	Ca		P		Cl		Nd	
	f′	f″	f′	f″	f′	f″	f′	f″
MoKα	0.24	0.36	0.11	0.12	0.15	0.19	-0.39	3.42
CuKα	0.36	1.34	0.27	0.46	0.33	0.72	-3.70	10.65
FeKα	0.21	1.98	0.32	0.68	0.36	1.07	-10.39	8.88

the counting circuits, which improved the signal-to-noise ratio by eliminating portions of the "white" background and harmonics of the $K\alpha$ wavelength.

Aperture Selection

A circular aperture of diameter $\frac{1}{4}$ inch, selected by means of the operational procedure described in Chapter II, was used. It was found that his size aperture maximized the net integrated intensity while not diminishing the signal-to-noise ratio with an aperture larger than was needed.

Computer-Controlled System

(h, k, ℓ) Selection

The reflections to be observed with the computer-controlled diffractometer could be chosen by one of two methods. The (h,k,ℓ) values could be generated by a subroutine programmed to generate any predeterminable sequence of (h,k,ℓ) desired. The second method of (h,k,ℓ) selection retrieved Miller indices which had been previously stored in the disk memory. This second method permitted one easily to go back and re-collect these reflections which had been flagged in the teletype output as suffering from some blunder or systematic error. Maximum and minimum limits could be specified for the angle 2θ. By collecting successive sets of data with different angular limits on 2θ, one could effectively collect the data from concentric bands in reciprocal space. As mentioned previously, there was not enough time to collect all of the accessible reflections; by collecting concentric banks of data, one could obtain data for all angular orientations and for a

wide range of $\sin\theta/\lambda$. A wide range in $\sin\theta/\lambda$ is necessary to reduce the otherwise extremely high correlations between the overall scale factor and the overall temperature factor.

Scan Mode and Filter Selection

After the next reflection (h,k,ℓ) to be observed is selected, a subroutine is entered to determine which one of four scan modes will be used to collect the integrated intensity data for that particular reflection. From Bragg's law we obtain

$$2\theta = 2\sin^{-1}(\lambda d^*/2) \quad . \tag{70}$$

Using equation (70) we can calculate the position of the peaks due to $K\alpha$ and to $K\beta$ wavelengths. If the separation between the two peaks is less than 3/2 of the width of the peak scan, the balanced-filter ω-scan mode is used.

$$2\theta_{K\alpha} - 2\theta_{K\beta} < 3/2 \text{ (Peakwidth)} \tag{71}$$

If equation (71) is not satisfied, then a balanced-filter ω-scan is not necessary for the α and β peaks are resolved enough for the β peak to be well outside of the range of the peak and background scan. The factor 3/2 arises since in the worst case conditions (signal-to-noise ratio = 0) the width of the background scan on one side of the peak is $\frac{1}{2}$ the width of the peak scan. Thus, the α and β peaks must be separated by more than one peak width plus the width of one background scan in order that the α-β filter ω-scan mode need not be used.

If a balanced-filter ω-scan is not needed, the order (N) of the reflection is then determined, to enable one to determine if the β-peak of the (N + 1)th order (or greater) will occur in the scanning range for the α-peak of the Nth order. Let N be the order and d* the reciprocal spacing of the reflection to be observed, then if

$$2\sin^{-1}\left(\frac{N+1}{N}\ \frac{\lambda_\beta d^*}{2}\right) - 2\sin^{-1}\left(\frac{\lambda_\alpha d^*}{2}\right) > 3/2\ \text{(Peakwidth)} \qquad (72)$$

is satisfied a no-filter 2θ scan mode is used. If equation (72) is not satisfied, a β-filter is required and one must then check to see if an α-filter scan will also be required. That choice depends on whether the absorption edge of the filter falls outside the angular range over which the peak and background will be scanned. Thus, if

$$(2\theta_{K\alpha} - 2\theta_{\beta\text{-Filter Abs. Edge}}) > 3/2\ \text{(Peakwidth)} \qquad (73)$$

is satisfied, a 2θ-scan β-filter suffices, otherwise an α, β balanced-filter 2θ-scan will be used. In equation (71) through (73) the term peakwidth is used and is defined as

$$\text{Peakwidth} \equiv \text{Basic Peakwidth} + D\tan\theta \qquad (74)$$

where the Basic Peakwidth is a constant term which takes into account the width of the peaks due to mosaicity, cross fire and divergence in

the beam, the size of the source and specimen; and the term which varies as tanθ takes into account the effect of dispersion on the peakwidth. Both the Basic Peakwidth and the dispersion constant D are quantities which must be supplied in the computer program during the set-up or initialization of the data collection procedure. The expression for D is

$$D = 2\left(\frac{\Delta\lambda}{\lambda}\right)(57.296) \qquad (75)$$

where $\Delta\lambda$ is the α-doublet separation. For MoKα radiation, D is 0.692 and for CuK, D is 0.285.

Algorithm for One Reflection

The angular settings for the 2θ, ω, χ, and ϕ axes are calculated for each (h,k,ℓ) for the bisecting position ($\omega = 0^\circ$) and for ω, χ, and ϕ values required to produce a rotation of ψ degrees about the diffraction vector. Before positioning the axes for the next reflection, the computer determines whether the calculated angles are accessible for both settings of ψ, without collisions occurring in the diffractometer. If either set of angle settings is inaccessible, that reflection is skipped and the program advances to the subroutine which selects the next (h,k,ℓ) for observation. If both sets of angular positions are accessible, the four diffractometer axes are driven to the bisecting position (i.e., $\omega = 0^\circ$) and the shutter is opened. A ten second sampling of the count rate is made. If during this time the count rate exceeds a certain level (predetermined by the electronic circuitry), an aluminum attenuator is placed automatically into the detected beam. Successively

thicker attenuators are placed in the beam until the count rate drops to an acceptable level or until the thickest available attenuator is in place. The attenuator holder is a motor driven wheel with 1 open hole and 5 holes in which disks of aluminum of gradually increasing μt have been placed. The count rate at which the attenuator circuit is triggered is approximately 27000 counts/sec.

Initial Determination of Signal-To-Noise Ratio and I_n

After the scan mode and attenuator have been selected, a 20 second survey of the selected Bragg peak is made. During the survey a 10 second sampling of the Bragg peak (for the $K\alpha_1$ wavelength) was made, and a 10 second sampling of the background was made with the detector displaced $\frac{1}{2}$ of the Peakwidth from the Bragg peak position. The signal-to-noise ratio S is approximated by

$$S \simeq (C_P - C_B)/C_B \tag{76}$$

where C_P and C_B are the counts accumulated during the counting period on the peak and on the background respectively. The optimum ratio (t_{opt}) of the time to spend on the peak to the time to spend on both sides of the background is (see Appendix B and Chapter III):

$$t_{opt} = (t_{peak}/t_{background}) = (S + 1)^{\frac{1}{2}} \tag{77}$$

for a single-filter or no-filter scan mode, and

$$t_{opt} = (S/2 + 1)^{\frac{1}{2}} \tag{78}$$

for a double- or balanced-filter mode. With the FACS-I system, the scanning speed is not under programmatic control. Since the peakwidth is fixed by equation (74) and the scanning speed is fixed by the drive gear selection, then t_{peak} is already determined. One would not want to make the peak scan any wider than required by equation (74), for to do so would decrease the signal-to-noise ratio unnecessarily. On the other hand, a peak scan any narrower would cut into the peak. Thus, one is left with the alternative of adjusting the amount of time spent on the background ($t_{background}$), i.e., increasing or decreasing the width of the background scan. Thus the scan limits for a particular Bragg peak are:

$$(2\theta_2 - 2\theta_1)/2(2\theta_1 - 2\theta_o) = (S+1)^{\frac{1}{2}} \tag{79}$$

and

$$(2\theta_2 - 2\theta_1)/2(2\theta_1 - 2\theta_o) = (S/2+1)^{\frac{1}{2}} \quad , \tag{80}$$

where equation (79) is for a single-filter case and equation (80) for a double-filter case. In equations (79) and (80), $2\theta_1$ and $2\theta_2$ are the extremes of the peak scan while $2\theta_o$ and $2\theta_1$ are the extremes for the background scan on the low angle side of the Bragg peak. A background scan on the same angular width is also made on the high angle side. The width of the peak $(2\theta_2 - 2\theta_1)$ is

$$(2\theta_2 - 2\theta_1) = (\text{Basic Peakwidth}) + D(\tan\theta) \quad . \qquad (81)$$

By utilizing the results of the survey, one can achieve the statistical precision that is desired in a shorter time or a smaller number of scans. For example, the time needed to obtain a given statistical precision in counting may be reduced by 50 per cent if the ratio of the time spent on the background is decreased from 4 to 1.5 (if $S = 1.25$).

Multiple Scans

During the initialization or set-up prior to the start of the data collection, the statistical precision desired and the maximum number of scans to be permitted are entered into the program via the teletype keyboard.

The number of counts collected and the elapsed times are saved for each of the 3 scan ranges: $2\theta_0$ to $2\theta_1$, $2\theta_1$ to $2\theta_2$, and $2\theta_2$ to $2\theta_3$. A linear-extrapolation background correction is made, using differences in the time of the scans rather than angular differences. The integrated intensity is computed and a standard deviation is calculated based on counting statistics. If $(\sigma/I_N) > P(2)^{\frac{1}{2}}$, where P is the desired precision which was entered into the program during initialization, then the four scan points are readjusted on the basis of the updated signal-to-noise ratio, and another scan is made. The counts and times for the successive scans are accumulated and the scanning process is continued until $(\sigma/I_N) < P(2)^{\frac{1}{2}}$ or until the upper limit to the number of scans is reached.

Test for Blunders and Simultaneous Diffraction Effects

The results obtained from these scans are saved, and the crystal is rotated Ψ degrees about the diffraction vector. A multiple scan process similar to that just described is performed at the second setting about the diffraction vector. For this work, the amount which the crystal was rotated about the diffraction vector was $\Psi = 1^{\circ}$. Small deviations of the crystal from spherical symmetry, should not show up as intensity differences at these two settings, since the specimen is only rotated one degree. Differences greater than expected from counting statistics along (e.g., at the 99.74 per cent confidence level) can, then, be assigned to possible blunders or simultaneous diffraction effects. If the net integrated intensity at the two settings about the diffraction vector differed by more than 3σ, where σ is the standard deviation based on counting statistics, then the output of the teletype for that reflection was flagged. Thus, random misreadings of the scaler or timer (which result in an intensity difference of 3σ or more) could be detected as well systematic differences in the intensities due to anisotropic extinction or simultaneous diffraction. An abrupt change in the specimen alignment would also result in the subsequent flagging of all or most of the reflections; perhaps long before the time the next standard reflection was scheduled for observation.

Tests for Filter Balance and Unexpected Character in Background

If the scan mode used was one of the balanced-filter modes, the data were checked for proper balance of the filters in two ways. If either condition was violated, the corresponding error flag was included in the line of teletype output for that reflection. One of the checks is:

$$|\text{BACKGROUND}_{\beta} - \text{BACKGROUND}_{\alpha}| + 4\sigma > 0 \qquad (82)$$

on both sides of the peak, i.e., within an allowed statistical error limit of 4σ in the quantities measured, the intensity obtained with the α filter must always be less than or equal to that obtained with the β filter in place. The other check determined whether the differences between the α and β filters are the same, within 4σ, on both sides of the peak. For example, angular dependence of the non-Bragg scattered radiation of pass-band wavelengths will cause a reflection to be flagged as a result of this latter check.

$$|\text{BACKGROUND}(\beta - \alpha)_{\text{High}} - \text{BACKGROUND}(\beta - \alpha)_{\text{Low}}| + 4\sigma > 0 \qquad (83)$$

Instrument Performance Monitors of the Computer Controlled System

Collision Recovery

If, in spite of the check made by the software, a collision occurs, all motors which were running on the diffractometer will be reversed for one second and a computer interrupt will be generated. As presently programmed, the software handler for the collision interrupt will generate a line of teletype output for that reflection, in which a flag indicates that a collision has occurred. The data for the next reflection in sequence is then collected. In practice, the only collisions which have occurred have been those where a fully extended

arc on a goniometer head touched the coiled-spring guards on the incident or diffracted beam tunnels. This geometrical restriction varies from crystal to crystal and has not been taken into account in the program as have the other geometrical limitations.

Recovery From Shaft-Encoder Failure

The absolute position of any of the motorized axes, was sensed by shaft encoders, one encoder for each motorized axis (2θ, ω, χ, ϕ). The encoders were a brush-and-disk type, with the output of the encoder in binary coded decimal (BCD). The encoders were designed to generate two complementary representations of each shaft position from two independent sets of brushes. Thus, each reading of each encoder could be checked for accuracy by comparison of the independent read outs. This feature became important as the encoders aged and the read-failure rate increased. The program provided with the FACS-I system was modified in order to prevent the data collection program from entering an infinite loop while trying to read a "bad spot" on an encoder. Now, read-failures are ignored while the axes are being scanned. However, if a read-failure occurs at a position at which one of the diffractometer axes is instructed to stop, and if this read-failure persists for as long as ten seconds, then a line of output is generated on the teletype for that reflection and includes a flag indicating which encoder had the read-failure. The program control then passes on to the next reflection with only ten seconds, at most, being lost. It is important to note that any read-failure which persists for less than ten seconds will not cause the loss of the data for that reflection. Since the 2θ axis scanning speed is 2°/minute, a band of encoder positions 1/3 of a degree wide

would all have to be bad for the reflection data to be lost. However, a single bad encoder position will cause the loss of the reflection data if that spot is one at which an axis must be positioned.

Monitoring of Incident Beam

The data collection program is executed concurrently with a 100 hertz clock interrupt. These interrupts can be counted for timing purposes, the nominal time resolution then being 1/100 of a second. On the basis of input information, standard reflections are programmatically inserted into the data collection procedure every T minutes. In practice, the time between standards will be somewhat greater than T, since the data collection on the current reflection is allowed to finish before data collection for the standard is initiated. The Miller indices of the standard reflection and the time between standards are specified during the initialization of the data collection program.

At present only one standard reflection is being collected every T minutes; however, the program segment which controls the collection of the standards could be changed to collect several standard reflections every T minutes.

To be chosen as a standard, a reflection was required to have a good signal-to-noise ratio and its integrated intensity had to be insensitive to rotations about the diffraction vector, particularly in that range of ψ being used for the experiment ($\psi = 0^{\circ}$ to 1°).

REFERENCES

1. Abrahams, S. C. (1964). Acta Cryst. 17, 1190.

2. Abrahams, S. C., Alexander, L. E., Furnas, T. C., Hamilton, W. C., Ladell, J., Okaya, Y., Young, R. A., and Zalkin, A. (1967). Acta Cryst. 22, 1.

3. Abrahams, S. C. and Bernstein, J. C. (1965). Acta Cryst. 18, 926.

4. Abrahams, S. C. and Keve, E. T. (1971). Acta Cryst. A27, 157.

5. Annaka, Shoichi (1962). J. Phys. Soc. Japan. 17, 846.

6. Arndt, U. W. (1964). Acta Cryst. 17, 1183.

7. Arndt, U. W. and Willis, B.T.M. (1966). Single Crystal Diffractometry. Cambridge University Press, Cambridge, Great Britain.

8. Åsbrink, Stig (1970). Acta Cryst. A26, 385.

9. Azaroff, L. V. (1955). Acta Cryst. 8, 701.

10. Beevers, C. A. and McIntyre, D. B. (1946). Miner. Mag. 27, 254.

11. Bond, W. L. (1960). Acta Cryst. 13, 814.

12. Braun, N. M. (1970). Private Communication.

13. Brown, W. E. (1972). Structural Properties of Hydroxyapatite and Related Compounds, Brown, W. E. and Young, R. A., Eds., Gordon and Breach, to be published.

14. Brown, W. E. and Young, R. A., Eds. (1972). Structural Properties of Hydroxyapatite and Related Compounds, Gordon and Breach, to be published.

15. Burbank, R. D. (1965). Acta Cryst. 19, 957.

16. Busing, W. R., Ellison, R. D., Levy, H. A., King, S. P., and Roseberry, R. T. (1968). The Oak Ridge Computer-Controlled X-Ray Diffractometer, ORNL-Report 4143.

17. Busing, W. R., Martin, K. O., and Levy, H. A., A Fortran Crystallographic Least-Squares Program, ORNL-TM-305, 1962.

REFERENCES (Continued)

18. Butt, N. M. and O'Connor, D. A. (1967). Proc. Phys. Soc. 90, 247.

19. Chandrasekhar, S., Ramaseshan, S., and Singh, A. K. (1969). Acta Cryst. A25, 140.

20. Cochran, W. (1969). Acta Cryst. A25, 95.

21. Cole, H., Chambers, F. W., and Dunn, H. M. (1962). Acta Cryst. 15, 138.

22. Commission on Crystallographic Apparatus (1966). Section 1, International Union of Crystallography, Seventh International Congress and Symposium, Moscow, USSR.

23. Cooper, M. J. and Nathans, R. (1968). Acta Cryst. A24, 481.

24. Cooper, M. J. and Rouse, K. D. (1968). Acta Cryst. A24, 405.

25. Coppens, P. (1968). Acta Cryst. A24, 253.

26. Cromer, D. T. (1965). Acta Cryst. 18, 17.

27. Cromer, D. T. (1965). Acta Cryst. 18, 104.

28. Cruickshank, D.W.J. (1956). Acta Cryst. 9, 747.

29. Cruickshank, D.W.J. and McDonald, W. S. (1967). Acta Cryst. 23, 9.

30. Dawson, B. (1967). Proc. Roy. Soc. A298, 264.

31. Eaglet, R. D. (1970). Private Communication.

32. Elliott, J. C. (1971). Nature 230, 72.

33. Elliott, J. C. and Young, R. A. (1968). Bulletin de la Société Chimique de France, (n° Spécial), 1763.

34. Ewald, P. P. (1921). Z. Kristallogr. Miner. 56, 129.

35. Gottlicher, S. (1968). Acta Cryst. B24, 122.

36. Hendricks, S. B., Jefferson, M. E., and Mosley, V. M. (1932). Z. Kristallogr. 81, 352.

37. Hounslow, A. W. (1968). Ph.D. Thesis. Carleton University, Ottawa, Ontario.

REFERENCES (Continued)

38. Hounslow, A. W. and Chao, G. Y. (1970). Can. Miner. 10, 252.

39. International Tables for X-Ray Crystallography (1969). Birmingham: Kynoch Press.

40. Jennings, L. D. (1968). Acta Cryst. A24, 472.

41. Johnson, J. W. (1971). Private Communication.

42. Kaplow, R. and Posen, H. (1969). J. Appl. Phys. 40, 4948.

43. Keppler, U. (1968). N. Jb. Miner. Mh. 359.

44. Keppler, U. (1969). N. Jb. Miner. Mh. 64.

45. Lomer, T. R. (1966). Proc. Phys. Soc. 89, 135.

46. Lucas, B. W. (1968). Acta Cryst. A24, 336.

47. Lucas, B. W. (1969). Acta Cryst. A25, 627.

48. Mack, M. and Spielberg, N. (1958). Spectrochim. Acta 12, 169.

49. Mackie, P. E. (1971). American Crystallographic Association Meeting, Ames, Iowa, Paper E9.

50. Mackie, P. E., Elliott, J. C., and Young, R. A. (1972). Acta Cryst. In Press.

51. Mackie, P. E. and Young, R. A. (1971). American Crystallographic Association Meeting, Columbia, South Carolina, Paper G4.

52. Mazelsky, R., Ohlmann, R. C., and Steinbruegge, K. (1968). J. Electrochem. Soc.: Solid State Science 115, 68.

53. Miyake, S., Towaga, S., and Hosoya, S. (1964). Acta Cryst. 17, 1083.

54. Nilsson, Nanny (1957). Arkiv För Fysik 12, 247.

55. O'Connor, D. A. and Butt, N. M. (1963). Phys. Letters 7, 233.

56. Olekhnovich, N. M. (1969). Kristallografiya 14, 261.

57. Panke, D. and Wölfel, E. (1968). J. Appl. Cryst. 1, 255.

58. Parrish, W. (1956). Philips Tech. Rev. 17, 206.

REFERENCES (Continued)

59. Posner, Aaron S. and Perloff, Alvin (1957). J. Res. N.B.S. 58, 279.

60. Prener, J. S. (1967). J. Electrochem. Soc. 114, 77.

61. Prener, J. S. and Piper, W. W. (1971). Structural Properties of Hydroxyapatite and Related Compounds. Brown, W. E. and Young, R. A., Eds., Gordon and Breach, to be published.

62. Renninger, M. (1955). Acta Cryst. 8, 606.

63. Rouse, K. D. and Willis, B.T.M., Pryor, A. W. (1968). Acta Cryst. B24, 117.

64. Santoro, A. and Zocchi, M. Acta Cryst. 17, 597.

65. Shannon, R. D. and Prewitt, C. T. (1969). Acta Cryst. B25, 925.

66. Shoemaker, D. P. (1968). Acta Cryst. A24, 136.

67. Skelton, E. F. and Katz, J. L. (1969). Acta Cryst. A25, 319.

68. Smith, A. E. (1968). American Crystallographic Association Meeting, Tucson, Arizona, Paper H2.

69. Sudarsanan, K. (1967). Private Communication.

70. Sudarsanan, K. (1971). Private Communication.

71. Sudarsanan, K. and Young, R. A. (1968). American Crystallographic Association Meeting, Buffalo, New York, Paper LL2.

72. Sudarsanan, K. and Young, R. A. (1969). Acta Cryst. B25, 1534.

73. Sudarsanan, K. and Young, R. A. (1970). American Crystallographic Association Meeting, New Orleans, Louisiana, Paper N2.

74. Sudarsanan, K. and Young, R. A. (1971). American Crystallographic Association Meeting, Ames, Iowa, Paper N11.

75. Ueki, T., Zalkin, A., and Templeton, D. H. (1966). Acta Cryst. 20, 836.

76. Willis, B.T.M. (1965). Acta Cryst. 18, 75.

77. Wilson, A.J.C. (1971). Private Communication.

REFERENCES (Concluded)

78. Young, R. A. (1959). Annual Report No. 1, Project A-389, Georgia Institute of Technology, Atlanta, Georgia.

79. Young, R. A. (1963). Zeitschrist für Kristallographia 118, 233.

80. Young, R. A. (1965). Transactions of the American Crystallographic Association 1, 42.

81. Young, R. A. (1969). Acta Cryst. A25, 55.

82. Young, R. A. (1972). Physics of X-Ray Diffraction, Chap. 7, L. V. Azaroff (Ed.), R. Kaplow, N. Kato, R. J. Weiss, A.J.C. Wilson and R. A. Young, McGraw-Hill Book Company, to be published.

83. Young, R. A. and Elliott, J. C. (1966). Archs. oral Biol. 11, 699.

84. Young, R. A., Goodman, R. M., Jr., and Kay, M. I. (1964). American Crystallographic Association Meeting, Bozeman, Montana, Paper A2.

85. Young, R. A. and Mackie, P. E. (1971). American Crystallographic Association Meeting, Columbia, South Carolina, Paper I5.

86. Young, R. A. and Wagner, C. E. (1966). Brit. J. Appl. Phys. 17, 723.

87. Zachariasen, W. H. (1963). Acta Cryst. 16, 1139.

88. Zachariasen, W. H. (1965). Acta Cryst. 18, 705.

89. Zachariasen, W. H. (1967). Acta Cryst. 23, 558.

90. Zachariasen, W. H. (1968). Acta Cryst. A24, 421.

VITA

Paul Elias Mackie, Jr. was born in Bridgton, Maine on April 19, 1942. He graduated from Kentucky Military Institute in Lyndon, Kentucky in 1960. He received the Bachelor of Science in Physics from the Georgia Institute of Technology in 1965. Since 1965, he has been associated with the Engineering Experiment Station at the Georgia Institute of Technology. He married Janet Lee Hawthorne on September 12, 1965. They have two sons, Paul Elias Mackie, III and William David Mackie. Mr. Mackie received the degree of Master of Science in Physics from the Georgia Institute of Technology in 1967. He is a member of the American Crystallographic Association, The American Association of Physics Teachers, The American Association for the Advancement of Science, and the honor society Sigma Pi Sigma. He is also an associate member of Sigma Xi.